

Copyright  
by  
Bruce Edward Rodenborn  
2011

The Dissertation Committee for Bruce Edward Rodenborn  
certifies that this is the approved version of the following dissertation:

**The Fluid Dynamics of Flagellar Swimming by  
Microorganisms and Harmonic Generation by  
Reflecting Internal, Ocean-like Waves**

Committee:

---

Harry L. Swinney, Supervisor

---

Roger Bengtson

---

Wendell Horton

---

William McCormick

---

Zong-Liang Yang

**The Fluid Dynamics of Flagellar Swimming by  
Microorganisms and Harmonic Generation by  
Reflecting Internal, Ocean-like Waves**

by

**Bruce Edward Rodenborn, B.A.; B.S.Phys.**

**DISSERTATION**

Presented to the Faculty of the Graduate School of  
The University of Texas at Austin  
in Partial Fulfillment  
of the Requirements  
for the Degree of

**DOCTOR OF PHILOSOPHY**

THE UNIVERSITY OF TEXAS AT AUSTIN

December 2011

Dedicated to the memory of my mother Thelma Rodenborn.

## Acknowledgments

I first want to thank my wife Christine Garza for her support, which she gave without hesitation, when I returned to academic study in 2002, and again when I began graduate work in physics in 2006. Her support never wavered, even when I doubted myself. The sacrifices she has made for my intellectual pursuits are many, and for that I am indebted. I am also indebted to her for the support I have received from her family, especially her father Ernest and mother Vicki, whose pride in my accomplishments further strengthened my resolve.

My own family of eight siblings left indelible imprints on my personal and intellectual development, especially my oldest brother Brian, whose love of science inspired his younger brothers and sisters to be curious about the nature of the world. I regret that my mother did not live to see me complete my doctorate in physics, but she and my father set high standards for their children and filled our home with love, which endures after their passing in the lifelong relationships their many and varied children have with each other.

I want to thank Harry Swinney for guiding me as a fledgling scientist, and for believing in me after giving him reason to doubt my commitment. He embodies the best hopes that I have for myself as a physicist and of how I conduct my life. I also want to thank him for including me in the Hands

on Research in Complex Systems school, which allowed me to travel to India, Brazil and Cameroon where we taught tabletop experimental physics to the participants. As a result, I have had the great fortune to interact with many bright and dedicated scientists from all over the world. These experiences, and those yet to come, are some of the most cherished memories in my life. His love of physics and skill as a scientist may only be eclipsed by his love of and skill in teaching physics. He has instilled the same dedication in me and in myriad other researchers that have worked with him over his career. I am proud to be among that group.

I also owe a tremendous debt of gratitude to Hepeng Zhang, Harry's former post doctoral researcher and now a professor in the Department of Physics and Institute of Natural Sciences at Shanghai Jiao Tong University in China. Hepeng endured long hours in the lab with me when I was an undergraduate student, teaching me how to use scientific equipment and how to analyze data. Those that know Hepeng are aware that he uses few words, reserving them for only what is necessary or humorous.

I want to thank our collaborators Phil Marcus and Chung-Hsiang Jiang at the University of California, Berkeley. They graciously agreed to provide the numerical code for my internal wave reflection study and trained me to use it. They also gave important feedback about the science as the work developed, and Chung-Hsiang gave frequent technical support when I was a Linux neophyte. They were instrumental in the success of the project.

I want to thank Olga Vera and Marybeth Casias for their hard work,

which shields students and faculty from numerous administrative headaches, even the ones we create for ourselves.

Finally, I want to thank the Center for Nonlinear Dynamics for being such a special place to complete my graduate studies. I have been inspired by the collegial atmosphere and dedication of both the students and faculty with whom I have shared my time here. I hope, as many before me have done, to bring that same attitude to wherever my career next takes me.

# **The Fluid Dynamics of Flagellar Swimming by Microorganisms and Harmonic Generation by Reflecting Internal, Ocean-like Waves**

Bruce Edward Rodenborn, Ph.D.  
The University of Texas at Austin, 2011

Supervisor: Harry L. Swinney

This dissertation includes two fluid dynamics studies that involve fluid flows on vastly different scales, and therefore vastly different physics. The first study is of bacterial swimming using a flagellum for propulsive motion. Because bacteria are only about  $10\ \mu\text{m}$  in length, they swim in a very low Reynolds number ( $10^{-4}$ ) world, which is described by the linear set of governing equations known as the Stokes equations, that are a simplified version of the Navier-Stokes equations. The second study is of harmonic generation from nonlinear effects in internal, ocean-like wave beams that reflect from boundaries in a density stratified fluid. Internal wave reflection is an important oceanic process and may help sustain ocean circulation and affect global weather patterns. Such ocean processes have typical Reynolds numbers of  $10^{10}$  or more and are only described by the full, nonlinear Navier-Stokes equations.

In the low Reynolds number study, I examine theories by Gray et al. (1956) and Lighthill (1975) that describe swimming microorganisms using a

helical flagellum for propulsive motion. I determine the resistance matrix, which can fully describe the dynamics of a flagellum, for flagella with different geometries, defined by: filament radius  $a$ , helical radius  $R$ , helical pitch  $\lambda$ , and axial length  $L$ . I use laboratory experiments and numerical simulations conducted in collaboration with Dr. Hepeng Zhang. The experiments, conducted with assistance from a fellow graduate student Chih-Hung Chen, use macroscopic scale models of bacterial flagella in a bath of highly viscous silicone oil. Numerical simulations use the Regularized Stokeslet method, which approximates the Stokeslet representation of an immersed body in a low Reynolds number flow. My study covers a biologically relevant parameter regime:  $1/10R < a < 1/25R$ ,  $R < \lambda < 20R$ , and  $2R < L < 40R$ . I determine the three elements of the resistance matrix by measuring propulsive force and torque generated by a rotating, non-translating flagellum, and the drag force on a translating, non-rotating flagellum. I investigate the dependences of the resistance matrix elements on both the flagellum's axial length and its wavelength. The experimental and numerical results are in excellent agreement, but they compare poorly with the predictions of resistive force theory.

The theory's neglect of hydrodynamic interactions is the source of the discrepancies in both the length dependence and wavelength dependence studies. I show that the experimental and simulation data scale as  $L/\ln(L/r)$ , a scaling analytically derived from slender body theory by my other collaborator Dr. Bin Liu. This logarithmic scaling is new and missing from the widely used resistive force theory. Dr. Zhang's work also includes a new parameter-

ized version of resistive force theory.

The second part of the dissertation is a study of harmonic generation by internal waves reflected from boundaries. I conduct laboratory experiments and two-dimensional numerical simulations of the Navier-Stokes equations to determine the value of the topographic slope that gives the most intense generation of second harmonic waves in the reflection process. The results from my experiments and simulations agree well but differ markedly from theoretical predictions by Thorpe (1987) and by Tabaei et al. (2005), except for nearly inviscid, weakly nonlinear flow. However, even for weakly nonlinear flow (where the dimensionless Dauxois-Young amplitude parameter value is only 0.01), I find that the ratio of the reflected wavenumber to the incoming wavenumber is very different from the prediction of weakly nonlinear theory. Further, I observe that for incident beams with a wide range of angles, frequencies, and intensities, the second harmonic beam produced in reflection has a maximum intensity when its width is the same as the width of the incident beam. This observation yields a prediction for the angle corresponding to the maximum in second harmonic intensity that is in excellent accord with my results from experiments and numerical simulations.

# Table of Contents

<b>Acknowledgments</b>	<b>v</b>
<b>Abstract</b>	<b>viii</b>
<b>List of Tables</b>	<b>xiv</b>
<b>List of Figures</b>	<b>xv</b>
<b>Chapter 1. Introduction</b>	<b>1</b>
1.1 Propulsion of microorganisms using a helical flagellum . . . . .	2
1.1.1 Organization of bacterial swimming work . . . . .	5
1.2 Reflection of internal gravity waves from a sloping boundary in a density stratified fluid . . . . .	6
1.2.1 Organization of internal wave reflection work . . . . .	10
<b>Chapter 2. Background and Literature Review</b>	<b>11</b>
2.1 Theory and motivation for bacterial swimming research . . . . .	11
2.1.1 Bacterial flagella . . . . .	11
2.1.2 Low Reynolds number hydrodynamics . . . . .	16
2.2 Slender body theory . . . . .	18
2.2.1 Resistive force theory predictions for a helical flagellum	21
2.2.2 Regularized Stokeslet method representation of a flagellum	28
2.2.3 Purpose of the bacterial swimming research . . . . .	31
2.3 Theory and motivation for internal wave reflection research . . . . .	32
2.3.1 Wave equation for internal waves . . . . .	32
2.3.2 Dispersion relation for internal waves . . . . .	35
2.3.3 Internal wave reflection . . . . .	37
2.3.4 Harmonic generation theories . . . . .	39
2.3.5 Purpose of the internal wave study . . . . .	40

<b>Chapter 3. Methods</b>	<b>42</b>
3.1 Bacterial Swimming . . . . .	42
3.1.1 Experiment . . . . .	42
3.1.1.1 Propulsive Force Measurements . . . . .	46
3.1.1.2 Drag Measurements . . . . .	51
3.1.1.3 Torque Measurements . . . . .	52
3.1.2 Numerical simulations . . . . .	53
3.2 Internal Wave Reflection . . . . .	55
3.2.1 Experiments . . . . .	55
3.2.2 Numerical simulations . . . . .	62
3.2.3 Data analysis . . . . .	70
<b>Chapter 4. Bacterial swimming with a helical flagellum</b>	<b>75</b>
4.1 Comparison of experiments, simulations and resistive force theories . . . . .	75
4.1.1 Dependence on helical pitch . . . . .	75
4.1.2 Dependence on flagellum length . . . . .	77
4.2 Analysis of why resistive force theories fail . . . . .	79
4.2.1 Asymptotic theory for long flagella . . . . .	79
4.2.2 Incorporating length scaling and wavelength dependence into resistive force theory . . . . .	82
4.2.3 Parameterization of $C_n$ , $C_t$ and $S_{drag}$ . . . . .	86
4.2.4 Hydrodynamic efficiency as test of the parametrization scheme . . . . .	88
<b>Chapter 5. Harmonic generation by internal gravity waves reflecting from a sloping boundary in a density stratified fluid</b>	<b>91</b>
5.1 Comparison of experiments and simulations to theories by Thorpe and Tabaei et al. . . . .	92
5.1.1 Intensity of second harmonic from experiment and simulation . . . . .	92
5.1.2 Quantifying nonlinearity . . . . .	93
5.1.3 An observation-based prediction in accord with experiment and simulation . . . . .	96

5.2	Analysis of the failure of weakly nonlinear and inviscid theories	99
5.2.1	Recovery of the Tabaei et al. prediction for low amplitude beams . . . . .	99
5.2.2	Wavenumber and amplitude of the reflected fundamental beam . . . . .	100
5.2.3	Wavenumber of the second harmonic . . . . .	101
5.2.4	Reflection compared to interaction of unbounded beams	103
<b>Chapter 6. Discussion</b>		<b>105</b>
6.1	Low Reynolds Number Flagellar Swimming . . . . .	105
6.1.1	Future bacterial swimming work . . . . .	109
6.2	Harmonic Generation by Reflection Internal Waves . . . . .	110
6.2.1	Future work on internal wave reflection . . . . .	112
<b>Appendix</b>		<b>115</b>
0.1	Compiling source files . . . . .	118
0.2	Libraries needed . . . . .	120
<b>Bibliography</b>		<b>123</b>

## List of Tables

- 2.1 The geometric parameters of helical flagella, radius  $R$ , wavelength  $\lambda$  (normalized by  $R$ ) and axial length  $L$  (normalized by  $\lambda$ ), for several species of bacteria, exemplifying the range over which the parameters vary. The filament radius of the flagellum is not listed, but current estimates are that it is  $a \sim 0.01 \mu\text{m}$ . 13
- 4.1 Geometric parameters and hydrodynamic efficiency of naturally observed bacterial flagella. Geometric parameters are from Spagnolie and Lauga [117] who averaged measurements found in the literature. In all computations, the filament radius is  $a = 0.01 \mu\text{m}$  and the contour length  $\Lambda = 10 \mu\text{m}$ . . . . . 89

## List of Figures

1.1	Movie frame showing the bacterium <i>rhodobacter sphaeroides</i> swimming with a single helical flagellum. The flagella have been fluorescently labeled to reveal the rotating helix used for propulsive motion[14]. . . . .	3
1.2	Sea surface temperature map from the Nasa Goddard Space Flight Center’s Scientific Visulation Studio showing data from the MODIS satellite system[23]. The Gulf Stream is clearly visible showing the northward transport of warm, saline tropical water. This advection of heat helps to warm Europe. After releasing its heat, the cold salty water is denser than the surrounding fluid and sinks in deep water formations as part of the Meridional Overturning Circulation[140]. . . . .	7
2.1	Schematic of a flagellum and definitions of geometric parameters. The flagellum is oriented along $\hat{x}$ direction with a pitch angle $\theta$ . A filament segment $ds$ is shown in the inset with tangential and normal directions denoted as $\hat{t}(x)$ and $\hat{n}(x)$ , respectively. We define a flagellum with an array, $[r, R, \lambda, L]$ , whose elements are filament radius $a$ , helical radius $R$ , helical pitch $\lambda$ , and axial length $L$ . The pitch angle $\theta$ is related to $k = 2\pi/\lambda$ and $R$ as $\tan\theta = kR$ . The length of the segment $ds$ in the inset is $\sqrt{1 + R^2k^2}dx$ . The total contour length of the filament is $\Lambda = L\lambda/\cos\theta$ . Two filament segments are marked in red to illustrate effects of hydrodynamic interactions (see Section 4.2.1). . . . .	14
2.2	Illustration adapted from [16] and [17] showing the complexity of a bacterial motor. The inset image shows a composite electron micrograph of a bacterial motor providing visual evidence of this complexity. Bacterial motors typically rotate at about 100 Hz and are driven by a ion flux of either protons or sodium atoms. . . . .	15

2.3	a) Slender body theory representation of a flagellum using a Stokeslet and a source dipole arranged along the helical centerline. The combination of Stokeslet plus dipole approximates the fluid response to a flagellum segment. (b) The regularized Stokeslet method of Cortez et al. [26] discretizes the surface of the flagellum and represents each surface element by a <i>Regularized Stokeslet</i> , which approximates a Stokeslet but avoids using delta function singularities. . . . .	29
2.4	Pictorial representation of a fluid parcel in a stratified fluid being displaced upward and then released. The parcel will experience restoring forces from gravity and buoyancy so that it oscillates about its equilibrium height until motion is damped out by viscous dissipation. The natural frequency of oscillation $N$ of such a fluid parcel is determined by the density profile of the fluid as given by Eq. 2.40. . . . .	32
2.5	Schematic of an internal wave beam. The beam energy is propagating in the direction of the group velocity $\mathbf{c}_g$ . Fluid motion is oscillatory along the lines of constant phase, and the lines of constant phase move in the direction of the wavenumber $\vec{k}$ . We define $\theta$ as the angle of $\vec{k}$ with respect to the vertical so that the dispersion relation (2.46) can be written as in (2.47). Note that group velocity $c_g$ and energy propagate at an angle $\theta$ with respect to the <i>horizontal</i> . . . . .	36
2.6	Schematic showing the reflection of an internal wave beam from a boundary at an angle $\alpha$ relative to the horizontal. The incoming and reflected wave beams are at angles $\theta_i$ and $\theta_r$ , respectively, which by the dispersion relation (1) are equal because the frequencies $\omega_i$ and $\omega_r$ are the same. However, the width and wavenumber of the reflected beam are different than those of the incident beam, as given by (3). The second harmonic wave beam (shown by the dashed lines) is generated by nonlinear interaction between the incoming and reflected wave beams, which occurs mainly in the overlap (shaded) region. The harmonic propagates at an angle given by $\sin \theta_h = 2\omega/N$ . The group velocities, $\mathbf{c}_i$ , $\mathbf{c}_r$ and $\mathbf{c}_h$ , indicate the direction of energy propagation. . . . .	38
3.1	Image of two aluminum mandrels used to form the flagella. The mandrel on the left has a wavelength $\lambda=3R$ and the one on the right has a wavelength $\lambda=6R$ , where $R$ is the radius of the mandrel. The wire is wrapped around the mandrels while the mandrels are held in by a collet in a lathe. The lathe is switched into neutral and rotated by hand. The wire is attached at the tip using a plate and screws, and at the end using a screw inserted into a threaded hole machined near the groove. . . . .	44

3.2	Image of flagella used in the length-dependence study formed using the mandrels in Fig. 3.1 using stainless steel welding wire. The wire is annealed on a mandrel for two hours at 350°C and left to cool for 24 hours, which helps it take the form. . . . .	45
3.3	Image of robotic bacterium used for the propulsive force measurements. The body is shown with a flagellum made from copper welding wire that has a diameter twice that of the flagella made from the stainless steel wire. The body is machined from a block of acrylic and a gear motor is inserted into a cavity behind the sealed ball bearing at the rear. A shaft adapter connects the motor to the flagella, which rotates at a frequency of $\sim 0.5$ Hz. The fluid is silicone oil with a viscosity $10^5$ times that of water to achieve a Reynolds number of $10^{-2}$ , similar to that of a bacterium. . . . .	47
3.4	Schematic of experimental apparatus: (a) Side and front view of setup for propulsive force measurements. (b) Side view of setup for drag measurements. . . . .	48
3.5	Sample dataset for propulsive force measurements for a flagellum with $R=6.1$ mm, $a=R/16$ , $\lambda=6.2$ R, and $L=22$ R, showing: (a) the frequency spectrum obtained from analyzing a movie of the rotating flagellum, (b) the force per unit frequency from multiple measurements of propulsive is determined by the slope of a line fit to the data. . . . .	50
3.6	Schematic of experimental apparatus for measuring torque. The flagellum is driven with a stepper motor giving computer control of its rotation rate. We use a Magnova MLY torque transducer calibrated by the manufacturer, which relies on a magnetic field generated by the active shaft when a torsional load is applied. The magnetic field is read using Hall effect probes. . . . .	54
3.7	Setup for the double-bucket method: the denser, salty water in tank 1 is pumped into tank 2, the mixed tank, which is continuously stirred. A second pump draws water from the mixed tank and pumps it into the bottom of the experimental tank. The pump rates are determined using the method of [97], which specifies the rates based on the instantaneous salt concentration necessary in the mixed tank to achieve the desired density profile in the experimental tank. . . . .	57
3.8	The wavemaker consists of five acrylic plates in box (right) driven by a camshaft (left) using a computer-controlled stepper motor. The desired beam profile is generated by selecting the angular difference $\Delta\phi$ between successive cams. In this example, $\Delta\phi = 45^\circ$ , which creates a half-sine wave configuration. . . . .	59

3.9	Vorticity field computed for $\theta_i = 22.7^\circ$ , $N = 1.63$ rad/sec, $\nu = 0.01$ cm <sup>2</sup> /s and plate angle $\alpha = 2.5^\circ$ . The computational domain has been rotated so that the gravity vector points downward; the image has been cropped to fit. The shaded box shows the location of the forcing term. A sponge layer has been added to the no-slip boundary at the top of the domain (boundary A) to absorb the upward propagating wave created by the wavemaker. The simulation is periodic at boundaries B and D, and there is a no-slip boundary condition at boundary C. . . . .	64
3.10	Snapshot of Filemaker Pro database used to both record the parameters for a given simulation ( $\sim 900$ in total) and to generate an ASCII file read in at runtime. The database also stores results from the analysis and allow for easy sorting and comparison between simulations. Records in the database are related to simulation data organized in directories labeled with the value in the Run ID field, which is highlighted. . . . .	66
3.11	(a) The time-independent velocity amplitude cross sections for wave beams under the same conditions as in Fig. 5.1. The cross section from the numerical simulation (dashed line) is accurately Gaussian, whereas there is a small departure from a Gaussian for the laboratory beam (solid line). (b) Vorticity cross section snapshots at the same location. . . . .	69
3.12	Snapshot of Matlab GUI used for data analysis showing the various parameter fields and buttons that launch analysis scripts. The parent directory is specified in the highlighted field and the directory with the data to be analyzed is specified in the Run ID field. The data are all stored in directories with the same name as the records in the Filemaker database. Values for the wave beam intensity and other results are returned in the field above and to the right of the figure. The values are also copied to the computer clipboard for easy transfer into the Filemaker database. . . . .	71
3.13	Contour plot of the measured second harmonic intensity, $(A_2)^2$ . The kinetic energy of the beam was integrated over the area where it was above one-half the maximum. Integration starts at the point of maximum kinetic energy within the beam (white circle). . . . .	73
4.1	Propulsive force (a), torque (b) and drag (c) of flagella with the same helical radius $a = 1/16R$ , axial length $L = 20R$ but different helical pitch $R < \lambda < 20R$ . Numerical results are the solid lines and experimental measurements are the black diamonds. Predictions from resistive force theory are shown as dotted lines for Gray et al.'s[49] drag coefficient expressions and dashed lines for Lighthill's expressions[81]. . . . .	78

4.2	Propulsive force (a), torque (b) and drag (c) for flagella with the same helical radius $a = 1/16R$ and pitch $\lambda = (2.42) R$ , but different axial lengths $L$ . Experimental data are shown as diamonds and numerical results are the solid curves. Simulation results are the solid lines and experimental measurements are the black diamonds. Predictions from resistive force theory are shown as dotted lines for Gray et al.'s[49] drag coefficient expressions and dashed lines for Lighthill's expressions[81]. . . . .	80
4.3	Axial length, $L$ , dependence. $F_x$ , $T_x$ and $D_x$ are rescaled (see text for details) and plotted as functions of axial length $L$ in (a), (b) and (c). The solid curves are simulations and the dashed lines are the asymptotic theory from (4.5) and (4.6). All data sets have the same filament radius $a = 1/16R$ . The helical pitch is $\lambda = 2.42R$ . For flagella longer than $\sim 3\lambda$ , the normalized $F_x$ , $T_x$ and $D_x$ are approximately constant, showing that Dr. Liu's asymptotic theory is correct. . . . .	83
4.4	(a) Drag coefficients $C_n$ (circles) and $C_t$ (squares) from simulations with $a = 1/16R$ , $L = 30R$ , and $R < \lambda < 20R$ . The solid lines are the new parameterization of these coefficients provided in Eq. 4.13. Lighthill's expressions for $C_n$ and $C_t$ are shown as dashed lines. (b) The new drag scaling factor extracted from the same simulations (diamonds) with the parameterization from Eq. 4.15 plotted as the solid lines. . . . .	85
4.5	Collapse of $C_n$ , $C_t$ and $S_{drag}$ to functions given by Eqs. (4.13) to (4.15). Different symbols correspond to a specific combination of $a$ , $R$ , $\lambda$ and $L$ . Our study covers a biologically relevant parameter regime of $1/10R < a < 1/25R$ , $R < \lambda < 20R$ , and $15R < L < 40R$ . . . . .	87
4.6	Hydrodynamic efficiency of two sets of flagella ( $R = 0.221 \mu\text{m}$ ) and ( $R = 0.123 \mu\text{m}$ ) from numerical simulations (Sec. 3.1.2). In both cases, the filament radius is $a = 0.01 \mu\text{m}$ and the contour length $\Lambda = 10 \mu\text{m}$ . Solid lines are directly computed from the numerical simulations and dashed lines are from the new resistive force parametrization scheme. The Peritrichous normal and curly form pitch angles with error bars (from experimental measurements in the literature) are indicated below the $R = 0.221 \mu\text{m}$ and $R = 0.123 \mu\text{m}$ curves respectively. . . . .	90
5.1	Instantaneous experimental and computed vorticity fields for forcing frequency, $\omega = 0.628 \text{ rad/s}$ , $N = 1.63 \text{ rad/s}$ , $\theta_i = 22.7^\circ$ , plate angle $\alpha = 14.1^\circ$ , and beam amplitude $A \sim 0.25 \text{ cm/s}$ . In the experiment the spatial resolution was $0.5 \text{ cm}$ . . . . .	92

5.2	Intensity of the second harmonic generated in the reflection of an incident internal wave beam (at $\theta = 22.7^\circ$ ) from a plate tilted at angle $\alpha$ . The curves are cubic spline fits to the data. The boundary angles $\alpha$ where the maxima occur are $\alpha_{max} = 13.2^\circ$ (experiment) and $14.1^\circ$ (simulation), far from either the $22.7^\circ$ predicted by Tabaei et al. [121] or the $8.25^\circ$ predicted by Thorpe [126]. . . . .	94
5.3	(a) The second harmonic amplitude depends quadratically (black line) on the incident wave beam amplitude, up to high amplitudes where the second harmonic determined in the simulations (solid dots) saturates (for a beam incident at $\theta = 22.7^\circ$ on a boundary at angle $\alpha = 12.5^\circ$ ). (b) Under the same conditions, the dimensionless amplitude parameter $a_{nonlinear}$ (Eq. (5.1)) in the simulations varied from 0.01 (very weakly nonlinear) to 0.52 (highly nonlinear), and in the experiments was 0.25 (corresponding to $A_{in} = 0.25$ cm/s). . . . .	95
5.4	The boundary angle corresponding to the maximum intensity of the second harmonic of an internal wave beam reflected from a surface, for incident beam velocity amplitudes $A = 0.25$ cm/s ( $a_{nonlinear} = 0.25$ ). My laboratory observations (triangles), numerical simulations (circles) with water viscosity ( $\nu = 0.01$ cm <sup>2</sup> /s) and numerical simulations with viscosity reduced by an order of magnitude (open squares) in (a) all agree well with the solid curve (Eq. (5.2)), which was obtained from ray theory, given the observation that the maximum intensity of second harmonic occurs when that beam's width is the same as that of the incident beam. Clearly, these results do not agree with either the Tabaei et al. [121] or the Thorpe [126] theory. . . .	97
5.5	Results from numerical simulations for the boundary angle corresponding to the maximum intensity of the second harmonic of an internal wave beam reflected from a surface, for incident beam velocity amplitudes $A = 0.01$ cm/s ( $a_{nonlinear} = 0.01$ ). These low-amplitude beams agree with the Tabaei et al. prediction for incident beam angles greater than $\sim 25^\circ$ (solid circles). When the viscosity is reduced from that of water by an order of magnitude, the agreement of the simulation with the Tabaei et al. prediction extends to about $15^\circ$ (open squares). . . . .	98

5.6	(a) The ratio of the dominant wavenumber in the incoming beam to the dominant wavenumber of the reflected beam (at the fundamental frequency) given by theory (Eq. (2.48), solid curve) and numerical simulation (data points and dashed line is an exponential fit to the data). (b) The prediction of the Tabaei et al. theory for the ratio of the reflected fundamental wave beam's peak amplitude to the incoming wave beam's peak amplitude, $A_r/A_i = \sin(\theta_r + \alpha)/\sin(\theta_i - \alpha)$ , compared with the results from my numerical simulation. Theory predicts that the amplitude of the reflected wave should diverge at the critical angle, whereas the simulations yield quite different behavior with a broad peak in the reflected wave amplitude at about $\alpha = 4.5^\circ$ and a monotonic decrease in amplitude for larger angles. (In both (a) and (b), $\theta_i = 22.7^\circ$ , $A_{in} = 0.25$ cm, and $a_{nonlinear} = 0.25$ .) . . . . .	102
1	Code from the <i>main.f90</i> source file showing the implementation of the parameter reader subroutine. New variables may be created here and read from the parameters.ascii file at runtime.	117
2	Makefile created for use on the Ranger system at the Texas Advanced Computing Center. . . . .	121

# Chapter 1

## Introduction

Physics students rarely study fluid mechanics as part of their undergraduate or even graduate studies. The focus of physics education in mechanics is most often on solid rather than continuum mechanics, yet fluids and fluid-like systems are ubiquitous, existing at vastly different scales ranging from the microscopic world to astrophysical systems such as cold proto-planetary discs.

In the early 1900's, physicists discovered that physics at very small length scales is a foreign world of quantum mechanical effects that are completely different than the dynamics at macroscopic scales. Likewise, the fluid dynamics of our cell's world is completely different than that of a proto-planetary disc. Fortunately, though, fluid mechanics has the advantage of dynamic similarity – the same dynamical behavior that exists on one scale may be observed at some other scale, if the rescaling is done properly.

The method to properly rescale a fluid flow was made well-known by Osborne Reynolds (1883), who was studying fluid resistance in pipe flow and sought a way to make his results applicable to any size pipe. Using physical reasoning and dimensional analysis, he found that the ratio of the inertial to

viscous forces, now called the Reynolds number, defined as:

$$Re \equiv \frac{\rho UL}{\mu} \tag{1.1}$$

where  $\rho$  is the fluid density,  $U$  is a typical velocity of the system,  $L$  is a typical length scale and  $\mu$  is the dynamic viscosity of the fluid, provides just such a non-dimensional way to compare fluid flows. He showed that if the Reynolds numbers and geometry are the same, so are the hydrodynamics[110].

Dynamic similarity is the common thread between the two fluid dynamics studies in this thesis. The fluid flows investigated have vastly different Reynolds numbers from each other, and both are much different than typical Reynolds numbers in our daily lives. The first is a study of the propulsion of microorganisms such as bacteria using a helical flagellum. The typical Reynolds number for swimming bacteria is  $Re=10^{-4}$ . The second study is of an oceanic process, harmonic generation by reflecting internal waves, which has a typical Reynolds number of  $Re=10^{10}$ . However, dynamic similarity allows us to analyze these fluid flows, which are separated by more than 10 orders of magnitude, using small laboratory tanks of similar dimensions. Our rescaled experiments allow more detailed analysis of the fluid dynamics than is typically accessible when studying the original systems.

## **1.1 Propulsion of microorganisms using a helical flagellum**

Many types of bacteria use rotating helical flagella for propulsive motion, cf. Fig. 1.1. Research over the past 50 years has increased the under-

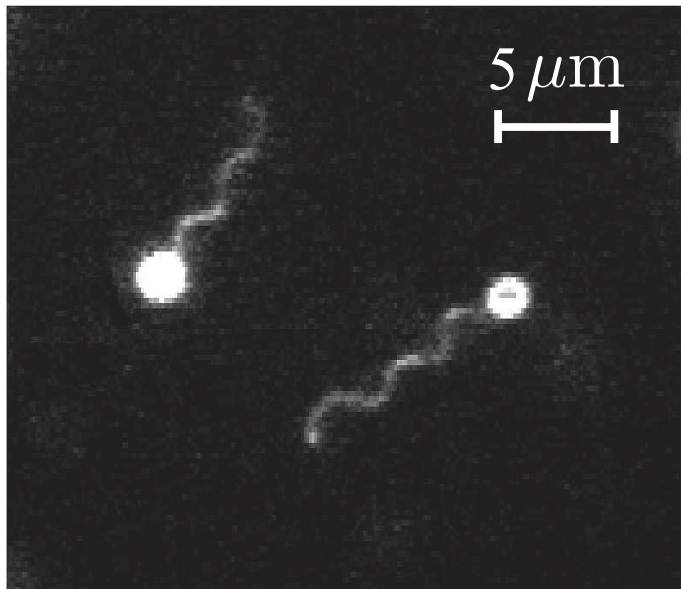


Figure 1.1: Movie frame showing the bacterium *rhodobacter sphaeroides* swimming with a single helical flagellum. The flagella have been fluorescently labeled to reveal the rotating helix used for propulsive motion[14].

standing of the structure of bacterial flagella[2, 113, 86] and the hydrodynamics of the world in which the bacteria live[122, 10, 106]. However, much is still unknown about bacterial flagellar swimming at these small scales.

Early theoretical work by J. Gray and G.J. Hancock[49] and James Lighthill [81] developed what is now called resistive force theory as a simplified model of the hydrodynamics of flagellar swimming. Their theories decompose the flagellum into short segments and calculate the fluid resistance to each element, ignoring interactions between parts of the flagellum beyond some small scale related to the flagellum geometry. The total force and torque is found by integrating over the contour length of the flagellum.

Resistive force theory has proven effective in describing the swimming of certain types microorganisms such as sperm[36], small worms [119] and even swimmers in granular material [88]. They are also used in fields such as the design of nano-scale robotic swimmers[11, 1, 50].

Some measurements[48, 62, 74] have shown qualitative agreement with resistive force theory for helical propulsion by bacterial flagella [49, 81]. More recent studies have quantitatively tested theoretical predictions using measurements of live bacteria, which require difficult, small scale experiments[24, 25]. Such bacterial research has shown that resistive force theory fails to accurately describe bacterial swimming, at least for the flagellar geometries studied.

However, bacterial flagella parameters vary, as described below, so I seek the functional dependences of propulsive force, torque and drag on a flagellum's helical geometry. I study this problem, not at the bacterial scale, but using macroscopic ( $R = 2$  cm) models of bacterial flagella in a bath of highly viscous silicone oil to achieve a Reynolds number much less than one ( $10^{-2}$ ), and using numerical simulations that implement the Regularized Stokeslet Method of Cortez et al. [26] conducted by my collaborator Professor Hepeng Zhang (Department of Physics and Institute of Natural Sciences, Shanghai Jiao Tong University, Shanghai, China and former post-doctoral researcher at UT-Austin).

I determine the propulsive force, torque and drag on flagella with different biologically relevant geometries, determining the dependence of these forces and torques on both the wavelength and the axial length of the flagella.

I compare the experimental and numerical results with the resistive force predictions found when using Gray et al.'s resistive force theory and when using Lighthill's expressions.

### **1.1.1 Organization of bacterial swimming work**

The research on bacterial swimming in this thesis was conducted in collaboration with three other researchers: Dr. Hepeng Zhang, Dr. Bin Liu (School of Engineering, Brown University) and Chih-Hung Chen, a fellow graduate student who assisted in gathering some of the experimental data.

The research is organized as follows: Chapter 2.1 describes the current understanding of bacterial flagella, basic theory of low Reynolds number fluid flows, theoretical work of Gray et al. and Lighthill and how resistive force theory predicts flagellar dynamics. Chapter 3.1 describes the experimental and computational methods used in this study. Chapter 4.1 compares my experimental results with the numerical results from Dr. Zhang, which agree but differ from the predictions of resistive force theories both in the wavelength dependence and length dependence studies. In Chapter 4.2, I describe Bin Liu's theoretical derivation for the length dependence found in the experiments and simulations. I also show Dr. Zhang's better, parameterized version of resistive force theory that accounts for the wavelength dependence we both found. I then test this new resistive force theory using hydrodynamic efficiency. Chapter 6.1 discusses the reasons for the failure of resistive force theory in its present form and how the new parameterized version solves these problems. I

also outline future work motivated by my findings, including a new project in development with my collaborators.

## **1.2 Reflection of internal gravity waves from a sloping boundary in a density stratified fluid**

The reflection of internal waves by topography results in mixing at the boundaries and redistribution of tidal energy in the ocean. The mixing work done by internal waves is hypothesized to be an important source of the potential energy increase needed to return deep, dense water to the surface [76, 34] as part of the meridional overturning circulation [32, 140].

Surface currents such as the Gulf Stream transport warm water from the equatorial regions to far northern and far southern latitudes, see Fig. 1.2. Because of increased solar evaporation near the equator, equatorial waters are saltier than most other parts of the ocean. When this warm, salty water reaches the arctic regions and cools, it is denser than the surrounding fluid and sinks to the bottom of the ocean in what are termed deep water formations, losing gravitational potential energy in the process[101]. Studies have shown that without a mechanism to inject gravitational potential energy into the ocean and return this deep, dense water to the surface, the ocean would be become a two-layer system with near-freezing water filling the ocean beneath a thin warm layer at the surface heated by the sun[91].

Instead, the ocean is continuously stratified, and the density of the ocean increases continuously with depth once below the thermocline, which is

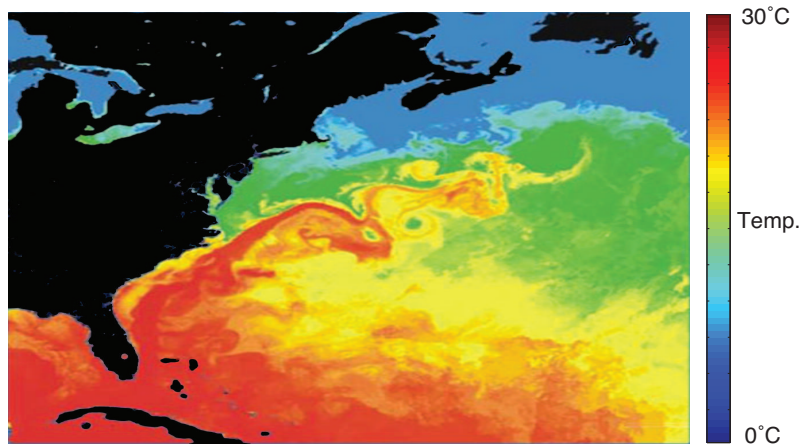


Figure 1.2: Sea surface temperature map from the NASA Goddard Space Flight Center's Scientific Visualization Studio showing data from the MODIS satellite system[23]. The Gulf Stream is clearly visible showing the northward transport of warm, saline tropical water. This advection of heat helps to warm Europe. After releasing its heat, the cold salty water is denser than the surrounding fluid and sinks in deep water formations as part of the Meridional Overturning Circulation[140].

a warmer and well-mixed layer in the upper ocean formed by solar heating and wind forcing[101]. Oceanographers believe that vertical mixing is the mechanism by which the deep water returns to the surface[91, 76, 34] as part of the meridional overturning circulation, [32, 140]. There is debate about the importance of vertical mixing in this process [134, 139], but most oceanographers believe that vertical mixing is essential.

Oceanographers also believe that tidally forced, internal waves are an important part of vertical mixing though the precise mechanisms are unknown[38]. For internal waves to be important, there must be an energy pathway to convert the kinetic energy injected by the pull of the moon's gravity into gravitational potential energy, and internal wave reflection may be one such mechanism.

Tidal flow of a stratified fluid over topography generates internal wave beams[68, 143, 144], and wave reflection modifies such internal waves beams in the ocean. Near the generation region, the wave spectrum includes high harmonic components[77]. However, high wave modes dissipate rapidly within about 100 km of the generation region[108].

The processes that both create and dissipate high wave modes are not well understood. Harmonics generated by reflection are a possible source of high wave modes, and they may be unstable, causing overturning and mixing. Further, reflection may lead to wave trapping in the boundary layer, another possible source of internal wave mixing. Thus, an understanding of internal wave beam generation and reflection is needed to understand energy transfer

in the oceans.

Theoretical work on internal wave reflection has generally been limited to inviscid, weakly nonlinear flow, whereas observations in the oceans, laboratory experiments and numerical simulations reveal that tidal flow over topography can generate intense, strongly nonlinear wave beams, particularly in regions where the slope of the topography matches the angle of internal wave propagation [6, 21, 73, 77, 38, 133, 143, 68]. Dauxois and Young developed a weakly nonlinear theory for near-critical reflection and concluded that if wave beams are strongly nonlinear, the reflection process will rapidly lead to turbulence and enhanced mixing near the slope [29]. These waves may erode continental slopes to the same angle as internal wave beams at the tidal frequency [21, 105, 144].

Weakly nonlinear analyses for inviscid fluids by Thorpe [126] and by Tabaei et al. [121] have predicted the value of the topographic slope angle at which the second harmonic intensity is a maximum. Pioneering experiments and simulations [99, 46] studied harmonic generation by reflecting internal waves but did not examine the applicability of the analyses of Thorpe and Tabaei et al. to strongly nonlinear reflection processes. The present study examines how the generation of second harmonic waves upon reflection from a sloping boundary depends on boundary angle, wave beam intensity, and fluid viscosity.

### 1.2.1 Organization of internal wave reflection work

The research on internal waves in this thesis was conducted almost exclusively by me, but it uses some experimental results gathered by Daniel Kiefer, who received a Masters in Physics from UT-Austin in 2006. Hepeng Zhang and Harry Swinney provided support and direction, but did not conduct either the computations or experiments. This work was previously published in February, 2011 in *Physics of Fluids* [111].

The research is organized as follows: Chapter 2.3 describes the physics of internal waves, the unique properties of internal wave reflection, and weakly nonlinear and inviscid theories by Thorpe and Tabaei et al. that make predictions about the functional dependence of harmonic generation on the boundary angle. Chapter 3.2 describes my experimental and computational methods, and data analysis. Chapter 5.1 compares my experimental and numerical results, which agree but differ from the predictions of both of the weakly nonlinear analyses for inviscid fluids. I show that, instead, the results agree with a prediction I deduced from an observed geometric relation between the second harmonic and incident wave beams. Chapter 5.1 also discusses how the results depend on forcing amplitude, viscosity, and frequency. Chapter 6.2 considers the implications of the geometric relation on the reflection of internal waves in theory and in the oceans.

## Chapter 2

### Background and Literature Review

#### 2.1 Theory and motivation for bacterial swimming research

##### 2.1.1 Bacterial flagella

I begin by considering the structure of a bacterial flagellum. Most prokaryotic flagella are assembled from the protein flagellin arranged like a “staircase” with  $5\frac{1}{2}$  helical subunits per turn along with auxiliary proteins that may modify the shape. This arrangement creates a hollow tube of flagellin with a radius  $\sim 10$  nm. The flagellin and other flagellar proteins most likely pass single file through the inner 3 nm channel of the flagellum, assembling at the tip of the structure outside of the cell[89].

There are no motor proteins in the flagellum so it has no ability to drive itself as in some eukaryotic flagella [86]. Instead, bacterial flagella are driven by a rotary motor whose shaft is attached to the “hook”, a sharp bend in the flagellum just outside the membrane of the bacterium[57, 16], which has a very precise 55 nm length[86].

A 5-30  $\mu\text{m}$  long helical filament forms from the top of the hook structure and terminates with capping proteins that shape the tip and prevent additional flagellin from binding[56, 89]. Unlike the hook, the helical portion of the

flagellum varies in length between bacteria of the same species and can regrow if broken[86].

Theoretical and experimental work show that bacterial flagella can take only a limited number of conformational shapes[3, 22, 86]. The shape of a flagellum is influenced by the underlying geometry of the flagellin assembly, rotation sense, and by ambient conditions such as the pH and salinity of the fluid[63]. However, as Darnton et al.[27] show, a bacterial flagellum is well represented as a rigid helix with a fixed geometry when it is used for propulsive motion.

The most common shape has been labeled the *normal* form and is the conformation used most often for propulsive motion[117]. Table 2.1 shows the physical characteristics for various conformational shapes of several types of bacterial flagella. The parameters in the table are defined in Fig. 2.1, which provides a schematic of a flagellum. The complex that drives the flagellum is “a nanotechnological marvel” [16]. It is a small rotary electric motor that has a drive shaft, bushings and mounting plate that attach it to the cell wall, see Fig. 2.2. The motor is assembled from about 20 motor-specific proteins, and is driven by an ion flux of either protons or sodium ions depending on the type of bacterium[17]. Bacterial motion is often “run and tumble” because the flagellum rotates in one direction, typically counterclockwise, to create directed propulsive motion, but then reverses its sense of rotation causing conformational changes in the flagellum and the bacterium to tumble[136]. Bacterial flagella typically rotate at about 100 Hz, which results in swimming

Helical parameters of selected bacterial flagella			
<b>Organism</b> [ref.]	$R$ ( $\mu\text{m}$ )	$\lambda/R$	$L/\lambda$
<b><i>Caulobacter crescentus</i></b> [69]			
Wild type	0.13	8.3	6
<b><i>Escherichia coli</i></b> <i>et al.</i> [28]			
CCW	$0.195\pm 0.025$	11	2.8
Stopped	$0.210\pm 0.025$	11	2.7
<b><i>Rhizobium lupini</i></b> [112]			
Normal	$0.250\pm 0.015$	5.4	4
Semicoiled	$0.385\pm 0.02$	2.9	3
Curly	$0.135\pm 0.02$	9.4	5
<b><i>Salmonella</i></b> [87]			
Wild type	$0.210\pm 0.005$	11	4
Curly mutant	—	—	11
Tumbling mutant	$0.145\pm 0.005$	7.6	9

Table 2.1: The geometric parameters of helical flagella, radius  $R$ , wavelength  $\lambda$  (normalized by  $R$ ) and axial length  $L$  (normalized by  $\lambda$ ), for several species of bacteria, exemplifying the range over which the parameters vary. The filament radius of the flagellum is not listed, but current estimates are that it is  $a \sim 0.01 \mu\text{m}$ .

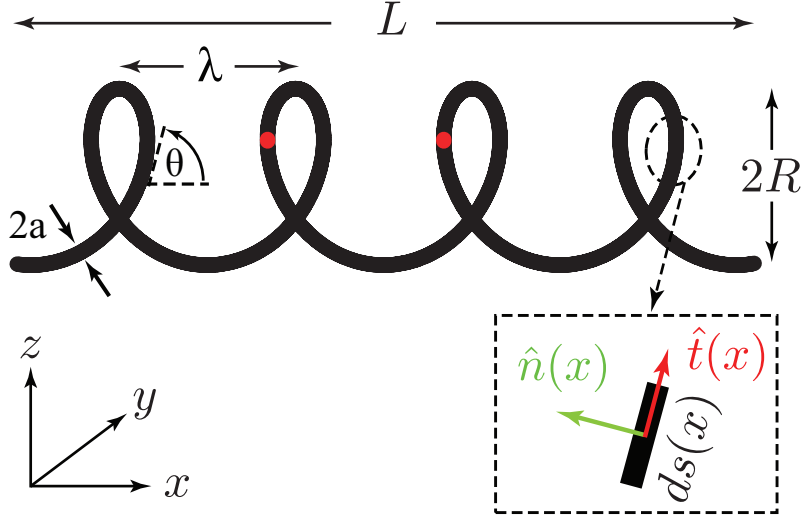


Figure 2.1: Schematic of a flagellum and definitions of geometric parameters. The flagellum is oriented along  $\hat{x}$  direction with a pitch angle  $\theta$ . A filament segment  $ds$  is shown in the inset with tangential and normal directions denoted as  $\hat{t}(x)$  and  $\hat{n}(x)$ , respectively. We define a flagellum with an array,  $[r, R, \lambda, L]$ , whose elements are filament radius  $a$ , helical radius  $R$ , helical pitch  $\lambda$ , and axial length  $L$ . The pitch angle  $\theta$  is related to  $k = 2\pi/\lambda$  and  $R$  as  $\tan \theta = kR$ . The length of the segment  $ds$  in the inset is  $\sqrt{1 + R^2 k^2} dx$ . The total contour length of the filament is  $\Lambda = L\lambda/\cos \theta$ . Two filament segments are marked in red to illustrate effects of hydrodynamic interactions (see Section 4.2.1).

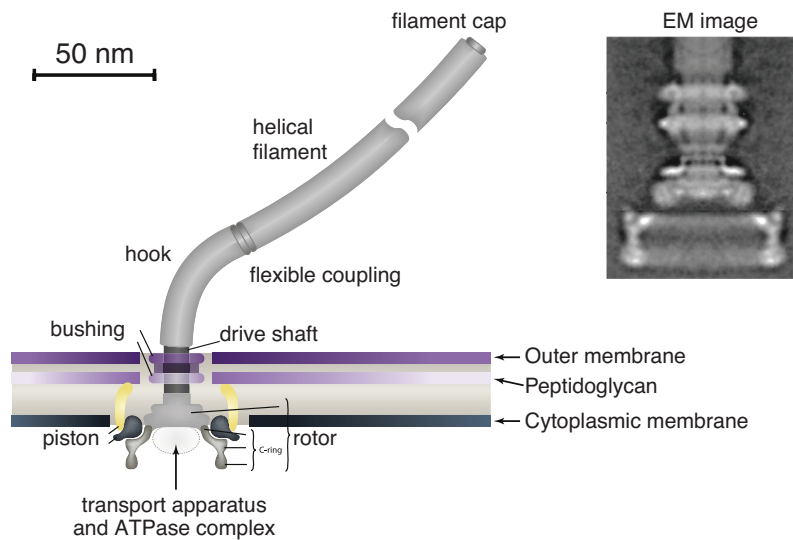


Figure 2.2: Illustration adapted from [16] and [17] showing the complexity of a bacterial motor. The inset image shows a composite electron micrograph of a bacterial motor providing visual evidence of this complexity. Bacterial motors typically rotate at about 100 Hz and are driven by a ion flux of either protons or sodium atoms.

speeds of 25-35  $\mu$  m/s. Bacteria are about 5-10  $\mu$ m in length so they move many body lengths per second[84].

The Reynolds number for a bacterium in water can be defined using the helical radius  $R$  as a typical length scale, and  $\omega R$  as a typical velocity for the system:

$$Re \equiv \frac{\rho UL}{\mu} = \frac{\rho(\omega R)R}{\mu} = \frac{(10^3 kg/m^3)(2\pi 100/s)(10^{-6}m)^2}{10^{-3}Ns/m^2} \approx 10^{-4} \quad (2.1)$$

As stated above, the Reynolds number represents the ratio of inertial to viscous forces in the fluid so a low Reynolds number, or Stokes flow, swimmer's inertia is so small that any momentum it imparts to the fluid is damped out almost immediately by viscous forces. Stokes flow dynamics are radically different from those experienced by macroscopic swimmers. Purcell provided the illustrative example of a ship floating in a sea of molasses whose propeller rotates once per month as a system with a Reynolds number similar to that of a bacterium[107].

### 2.1.2 Low Reynolds number hydrodynamics

The physics of Stokes flow hydrodynamics has been studied theoretically for over 100 years and has been found to be very different from typical macroscopic fluid dynamics. Seminal work by H.A. Lorentz (1896) showed that the Navier-Stokes and continuity equations for an incompressible Newtonian fluid in the low Reynolds number limit reduces to the Stokes equations:

$$-\nabla p + \mu \nabla^2 u = 0 \quad (2.2)$$

$$\nabla \cdot u = 0 \quad (2.3)$$

because the time derivative and nonlinear advective term become negligible. This new set of governing equations is much simpler, and importantly, is linear. The force  $\mathbf{F}$  and torque  $\mathbf{T}$  exerted on the fluid by an object that moves at a velocity  $\mathbf{U}$  and rotates at an angular velocity  $\Omega$  can thus be described using the following tensor equation[66]:

$$\begin{pmatrix} \mathbf{F} \\ \mathbf{T} \end{pmatrix} = \begin{pmatrix} \mathbf{A} & \mathbf{B} \\ \tilde{\mathbf{B}} & \mathbf{C} \end{pmatrix} \cdot \begin{pmatrix} \mathbf{U} \\ \Omega \end{pmatrix} \quad (2.4)$$

(Because momentum is dissipated so rapidly, the time rate of change of the momentum of freely moving, rigid object in Stokes flow is effectively zero, i.e. it remains force free. This means that the fluid must be exerting equal and opposite forces and torques on an object moving in the fluid.)

The matrix in Eq. 2.4 is referred to as the resistance matrix and its elements depend only on the geometry of the object. The sub-block matrices,  $\mathbf{A}$ ,  $\mathbf{B}$  and  $\mathbf{C}$  are three-dimensional and symmetric (i.e.  $\mathbf{A} = A_{ikj} = A_{jki}$ ), and therefore, so is the entire resistance matrix[66]. If this matrix is known, the trajectory of the object can be fully determined, but analytic solutions are rare for anything other than very simple geometries such as a sphere.

The linearity of the Stokes equations allows for important theoretical simplifications because the flow dynamics can be solved using a Green function

method. The solution for the fluid velocity and pressure field, or Stokeslet [51], resulting from a point-force at the origin,  $\mathbf{f}\delta(\mathbf{r})$ , is given by[66]:

$$\mathbf{u}(\mathbf{r}) = \mathbf{f} \cdot \mathbb{J}(\mathbf{r}) \quad (2.5)$$

$$p(\mathbf{r}) = \frac{\mathbf{f} \cdot \mathbf{r}}{4\pi|\mathbf{r}|^3} \quad (2.6)$$

where  $\mathbb{J}(\mathbf{r})$  is the Oseen Tensor defined as:

$$\mathbb{J}(\mathbf{r}) \equiv \frac{1}{8\pi\mu} \left( \frac{\mathbb{I}}{|\mathbf{r}|} + \frac{\mathbf{r}\mathbf{r}^T}{|\mathbf{r}|^3} \right) \quad (2.7)$$

H.A. Lorentz showed that the fluid response to a continuous force distribution from an immersed body can be found by superposing these Stokeslets[82], i.e.:

$$\mathbf{u}(\mathbf{r}) = \int \mathbf{f}(\mathbf{r}') \cdot \mathbb{J}(\mathbf{r} - \mathbf{r}') d\mathbf{r}' \quad (2.8)$$

$$p(\mathbf{r}) = \int \frac{\mathbf{f}(\mathbf{r}') \cdot (\mathbf{r} - \mathbf{r}')}{4\pi|\mathbf{r} - \mathbf{r}'|^3} d\mathbf{r}' \quad (2.9)$$

Lorentz also showed that the far field fluid response to a moving sphere (spherical distribution of Stokeslets) can be represented by a single Stokeslet and a source dipole of the same strength at the center of the sphere[71].

## 2.2 Slender body theory

Using these results, Hancock[51] developed a simplified model, *slender body theory*, to describe flagellar swimming. The theory was later refined by James Lighthill in 1975, but both use a “curvilinear distribution of elementary flow fields along the centerline of the flagellum” [82]. The centerline of the flagellum is moving during propulsive motion so they reasoned that each

cross section can be represented by a Stokeslet with a strength and direction proportional to the force per unit length on the flagellum plus a source dipole at that location, analogous to the solution for the sphere. (This geometric arrangement of the flow singularities is shown in Figure 2.3(a).)

The strengths of the Stokeslets and dipoles are determined from two boundary conditions: there is no fluid slip on the flagellum surface, and the total energy of the induced velocity field must remain finite. The second boundary condition is important because Stokes showed that otherwise a Stokeslet will induce a velocity distribution with infinite energy [51, 82].

Hancock and Lighthill sought a general representation of the flow induced at a point on the surface of the flagellum and decomposed the distribution of flow singularities on the centerline into three sets of Stokeslets and three sets of dipoles oriented in the  $x$ ,  $y$ ,  $z$  directions, where  $x$  is aligned along the flagellum axis as in Fig. 2.1. They separately analyzed the effects of the Stokeslets in each direction, and performed a similar analysis of the effects of the dipoles oriented in each of the three directions, summing the results to get the fluid velocity at any point on the flagellum [51, 82].

As part of their analysis, Hancock and Lighthill reasoned that dipolar fields fall off as  $r^{-2}$  whereas Stokeslets fall off as  $r^{-1}$  so there should be some intermediate distance  $q$  from any given point on the flagellum where only dipoles within  $q$  are important in determining the flow at that point, though all of the Stokeslets on the centerline must be considered because they are longer ranged.

Hancock derived integral representations of the flow velocity components at a point on the flagellum and expanded each velocity component in a power series. Lighthill developed a simpler integral representation and showed that the sum of the near and far field solutions for the induced fluid flow on a given segment could be made independent of  $q$  by the choice of source dipoles of the form[82, 75]:

$$-\frac{a^2 \mathbf{f}_n(r)}{4\mu} \quad (2.10)$$

where  $a$  is the radius of the filament and  $\mathbf{f}_n(r)$  is the component the Stokeslet strength,  $\mathbf{f}$ , in the plane perpendicular to the flagellum's centerline at that location and  $\mu$  is the dynamic viscosity of the fluid[81]. Lighthill also showed that the velocity of a flagellum segment located at  $s_0$  along the contour of the flagellum is [81]:

$$\mathbf{u}(s_0) = \frac{\mathbf{f}_\perp(s_0)}{4\pi\mu} + \int_{|\mathbf{r}_0 - \mathbf{r}| > \delta} \mathbb{J}(\mathbf{r}_0 - \mathbf{r}) \cdot \mathbf{f}(s) ds \quad (2.11)$$

where  $s$  is a point along the centerline of the flagellum,  $\mu$  is the dynamic viscosity,  $\mathbf{r}$  is a distance from the segment located at  $\mathbf{r}_0$  in three-dimensional space,  $\delta = a\sqrt{\epsilon}/2$  is the natural cutoff,  $\mathbb{J}$  is the Oseen Tensor of (2.7), and  $\mathbf{f}$  is the force per unit length on the flagellum and  $\mathbf{f}_\perp = \mathbf{f} \cdot \mathbf{nn}$  is the component of  $\mathbf{f}$  normal to the flagellum segment.

There are errors implicit in slender body theory because it assumes that a flagellum segment is locally straight, i.e. it ignores the effects of cur-

vature. In Hancock’s analysis, the errors from the power series expansion are  $O[\ln(2q/a)]$  whereas in Lighthill’s analysis, the errors were  $O[a/q]$ . For example, if  $q/a=100$ , the magnitude of the errors are 5.29 and 0.01, respectively, showing that Lighthill’s version of slender body theory is more accurate[82].

### 2.2.1 Resistive force theory predictions for a helical flagellum

The limitation of slender body theory is that to determine the force on each segment of the flagellum requires evaluating integrals of the form in Eqs. 2.8 and 2.9. These are generally intractable and so both Gray et al. and Lighthill sought to further simplify the problem by considering each segment of the flagellum represented by the Stokeslet and dipole as an independent slender rod. The resistance of the fluid to the slender rod’s motion is calculable if the local coefficient of drag for the segment and its velocity are known. Typically, the coefficient of drag is expressed in terms of normal and tangential drag coefficients per unit length,  $C_n$ , and  $C_t$ , respectively.

The total force and torque for any motion of the flagellum is found by an integration of the forces and torques from each small segment. Figure 2.1 shows such a small segment (see inset) and defines geometric parameters that describe a flagellum: filament radius  $a$ , helical radius  $R$ , helical pitch or wavelength  $\lambda$ , and axial length  $L$ , which I use for such calculations. The following derivation is based on similar work in [49] and [81].

In the figure, the flagellum is oriented along  $\hat{x}$  direction with a pitch angle  $\theta$ . I can parameterize the flagellum using the x-coordinate so that the

center line is given by:

$$\vec{r}(x) = [x, R \cos(kx), R \sin(kx)], \quad (2.12)$$

where  $k = 2\pi/\lambda$ .

Describing the local forces at this point  $\vec{r}(x)$  on the flagellum in terms of parallel and perpendicular drag coefficients requires defining both a tangential direction:

$$\hat{t}(x) = \frac{1}{\sqrt{1 + R^2 k^2}} [1, -Rk \sin(kx), Rk \cos(kx)] \quad (2.13)$$

and a normal direction:

$$\hat{n}(x) = [0, -\cos(kx), -\sin(kx)]. \quad (2.14)$$

The force exerted by an element  $ds$  on the fluid is given by  $d\vec{f} = \overleftrightarrow{K} \cdot \vec{u} ds$ , where  $\vec{u}$  is the local velocity and  $\overleftrightarrow{K}$  is the resistance tensor per unit length of a filament element, see Eq. 2.4. (Note that filament segments do not rotate locally so that  $\Omega$  is zero.)

The tensor  $\overleftrightarrow{K}$  depends only on the geometry of the filament element and can be written as:

$$\overleftrightarrow{K} = C_n \overleftrightarrow{I} + (C_t - C_n) \hat{t}\hat{t}. \quad (2.15)$$

The total force and torque exerted on the fluid by the flagellum is then:

$$\vec{F} = \int \overleftrightarrow{K} \cdot \vec{u} ds \quad (2.16)$$

$$\vec{T} = \int \vec{r} \times \vec{K} \cdot \vec{u} ds, \quad (2.17)$$

where again  $\vec{u}(x)$  is the filament velocity, and  $ds$  is the segment length.

These equations completely describe the motion of the helix, but in a different way than the resistance matrix description provided in Eq. 2.4. Therefore, I can use resistive force theory to calculate elements of the flagellum's resistance matrix under the following simplifying assumptions.

I am only concerned with the reduced problem of the flagellum rotating and translating in the axial direction (i.e. bacterial swimming). Because of the reduced dimensionality, I only need the force and torque in the  $x$  direction,  $F_t$  and  $T_x$ , resulting from a velocity and rotation in the  $x$  direction,  $U_x$  and  $\Omega_x$ . The resistance matrix simplifies to a  $2 \times 2$  array made of the  $A_{111}$ ,  $B_{111}$  and  $C_{111}$  components of the sub-block matrices in Eq. 2.4. The simplified problem is described by :

$$\begin{pmatrix} F \\ T \end{pmatrix} = \begin{pmatrix} A & B \\ B & C \end{pmatrix} \cdot \begin{pmatrix} U \\ \Omega \end{pmatrix} \quad (2.18)$$

where I have dropped the subscripts on the force and torque and on the matrix elements.

Now consider two types of constrained motion. The first type of motion is a flagellum rotating axially at some angular velocity  $\Omega$  but with the flagellum is constrained so that  $U = 0$ . Two resistance matrix elements can

be determined from Eq. 2.18 because it gives:

$$F_x = B\Omega \tag{2.19}$$

$$T_x = C\Omega. \tag{2.20}$$

Next, consider a flagellum that is constrained from rotating ( $\Omega = 0$ ) and being towed at some constant velocity  $U$ . The drag on this flagellum using Eq. 2.18 is:

$$D_x = AU \tag{2.21}$$

where again the subscript refers to the direction of the force on the flagellum, which gives the remaining matrix element.

Thus, I need to explicitly calculate the propulsive force and the torque in the  $\hat{x}$  direction for these two types of motion using resistive force theory, which I do below. The results will be in terms of the drag coefficients  $C_n$  and  $C_t$ , so I will subsequently describe derivations by Gray et al. and Lighthill who got separate expressions for them.

When a flagellum rotates at an angular frequency  $\Omega$ , the local velocity of an element is  $\vec{u}(x) = \Omega R [0, -\sin(kx + \Omega t), \cos(kx + \Omega t)]$ . The inner product of the local velocity with the segment's tangential and normal unit vectors gives the parallel and perpendicular velocities. Using local parallel and perpendicular drag coefficients for the segment, the force  $d\vec{f}$  generated by an element has cartesian components:

$$\begin{aligned}
df_x &= \hat{x} \cdot \overleftrightarrow{K} \cdot \vec{u} ds \\
df_x &= -(\Omega R) (C_n - C_t) \sin \theta \cos \theta ds \\
df_y &= \hat{y} \cdot \overleftrightarrow{K} \cdot \vec{u} ds \\
df_y &= (\Omega R) (C_n \cos^2 \theta + C_t \sin^2 \theta) \sin (kx + \Omega t) ds \\
df_z &= \hat{z} \cdot \overleftrightarrow{K} \cdot \vec{u} ds \\
df_z &= -(\Omega R) (C_n \cos^2 \theta + C_t \sin^2 \theta) \cos (kx + \Omega t) ds
\end{aligned} \tag{2.22}$$

Likewise, the torque in the  $\hat{x}$  direction exerted by each segment on the fluid is

$$\begin{aligned}
dT_x &= \vec{r} \times d\vec{f} \cdot \hat{x} \\
dT_x &= -R \sin (kx + \Omega t) df_y + R \cos (kx + \Omega t) df_z \\
dT_x &= -R (\Omega R) (C_n \cos^2 \theta + C_t \sin^2 \theta) ds
\end{aligned} \tag{2.23}$$

Integrating over the contour length, I get:

$$F_x = -(\Omega R) (C_n - C_t) \sin \theta \cos \theta \frac{L}{\cos \theta} \tag{2.24}$$

and

$$T_x = -(\Omega R^2) (C_n \cos^2 \theta + C_t \sin^2 \theta) \frac{L}{\cos \theta}, \tag{2.25}$$

The matrix elements  $B$  and  $C$  from Eqs. 2.19 and 2.20 are now known,  $B = F_x/\Omega$ , and  $C = T_x/\Omega$ .

For a translating, non rotating flagellum, the axial drag on this flagellum can be calculated as:

$$\begin{aligned}
df_x &= \hat{x} \cdot \overleftrightarrow{K} \cdot \vec{u} ds \\
df_x &= -u (C_n \sin^2 \theta + C_t \cos^2 \theta) ds,
\end{aligned} \tag{2.26}$$

Therefore the total drag is:

$$D_x = -u (C_n \sin^2 \theta + C_t \cos^2 \theta) \frac{L}{\cos \theta}. \tag{2.27}$$

giving  $A = D_x/U$ .

Through Eqs. 2.24, 2.25 and 2.27, resistive force theory gives predictions about the propulsive force, torque and drag on a rotating flagellum at low Reynolds number, and thereby predicts the form of the flagellum's reduced resistance matrix in terms of the flagellum geometry and the local drag coefficients  $C_n$  and  $C_t$ .

Gray et al. and Lighthill got expressions for the drag coefficients from slender body theory [49, 81, 75] by considering a small segment's tangential force acting at all points within a distance  $q$  from the segment. They then derived an expression for the tangential velocity generated on the surface of the segment. The ratio of the force divided by the velocity gives the tangential drag coefficient per unit length  $C_t$ .

In their analysis, Gray *et al.* [49] used a result for the tangential velocity on each segment of the flagellum found in Hancock's earlier slender body work[51] and derived the following expression for the tangential drag force per unit length:

$$df_t = \frac{2\pi\mu}{\left(\ln \frac{2\lambda}{a} - \frac{1}{2}\right)} u_t \quad (2.28)$$

where  $\mu$  is the fluid viscosity,  $q$  is the as yet undetermined length scale over which the forces act,  $a$  is the filament radius and  $u_t$  is the tangential fluid velocity. Gray et al. reasoned that there was only a logarithmic dependence on the length scale  $q$  in their expression so the choice was not terribly important, and chose the axial wavelength of the flagellum.

Thus, by dividing both sides by  $u_t$ , one gets the tangential drag coefficient per unit length:

$$C_t = \frac{2\pi\mu}{\ln \frac{2\lambda}{a} - 1/2} \quad (2.29)$$

Gray et al. also assumed that  $C_n = 2C_t$  based in part on results obtained by G.I. Taylor for an infinitely long filament undergoing sinusoidal motion in a plane[123], and probably based on experimental measurements of the wave speed of a sperm's flagellum relative to its propagation velocity, which implies a ratio close to 2:1 [81]. Thus, the normal drag coefficient per unit length is:

$$C_n = \frac{4\pi\mu}{\ln \frac{2\lambda}{a} + 1/2}. \quad (2.30)$$

The change of sign in the denominator of (2.30) was not part of Gray et al.'s original work, but was later adopted based on work by Lighthill. As part of a proof of his "fundamental theorem of flagellar hydrodynamics," he derived the same expression for the tangential force (2.28) which implies  $C_t$  is given by (2.29). Rather than assuming a ratio for the two drag coefficients, Lighthill derived the normal force per unit length, which implies the form for  $C_n$  in (2.30) that has subsequently been associated with Gray et al.[81].

Lighthill showed that the accuracy of the drag coefficients expressions could be improved by using his slender body theory formulation for the flow field near the flagellum, which was more accurate (Sec. 2.2), along with a better choice of the length scale over which higher order terms are important. He used a small fraction of the contour length of one wavelength for the length

scale  $q = 0.09(\frac{\lambda}{\cos\theta})$ , and derived:

$$C_t = \frac{2\pi\mu}{\ln \frac{0.18\lambda}{a \cos\theta}} \quad (2.31)$$

As stated, he did not assume the ratio of the drag coefficients had some specific value, and derived  $C_n$  by taking the ratio of the normal force exerted by the segment acting over length  $q$  divided by the normal velocity on the segment, which gives:

$$C_n = \frac{4\pi\mu}{\ln \frac{0.18\lambda}{a \cos\theta} + 1/2}. \quad (2.32)$$

These two sets of expressions (2.29)-(2.30) and (2.31)-(2.32) for  $C_n$  and  $C_t$  are the most commonly used expressions for resistive force theory drag coefficients in the literature. Through Eqs. 2.24 to 2.27 along with either set of drag coefficients expressions, resistive force theory predicts the form of a flagellum's resistance matrix.

### 2.2.2 Regularized Stokeslet method representation of a flagellum

Slender body theory is a simpler representation of a body immersed in a Stokes flow than fully discretizing the surface and assigning an appropriate Stokeslet to represent each surface element. However, the singular nature of the Stokeslets makes calculating the fluid response difficult both analytically and numerically, even with slender body theory's simplifications. Furthermore, the theory has errors that, though they tend to zero linearly as  $a/L \rightarrow 0$  [82], depend on the parameters of the flagellum being studied.

## Slender body theory

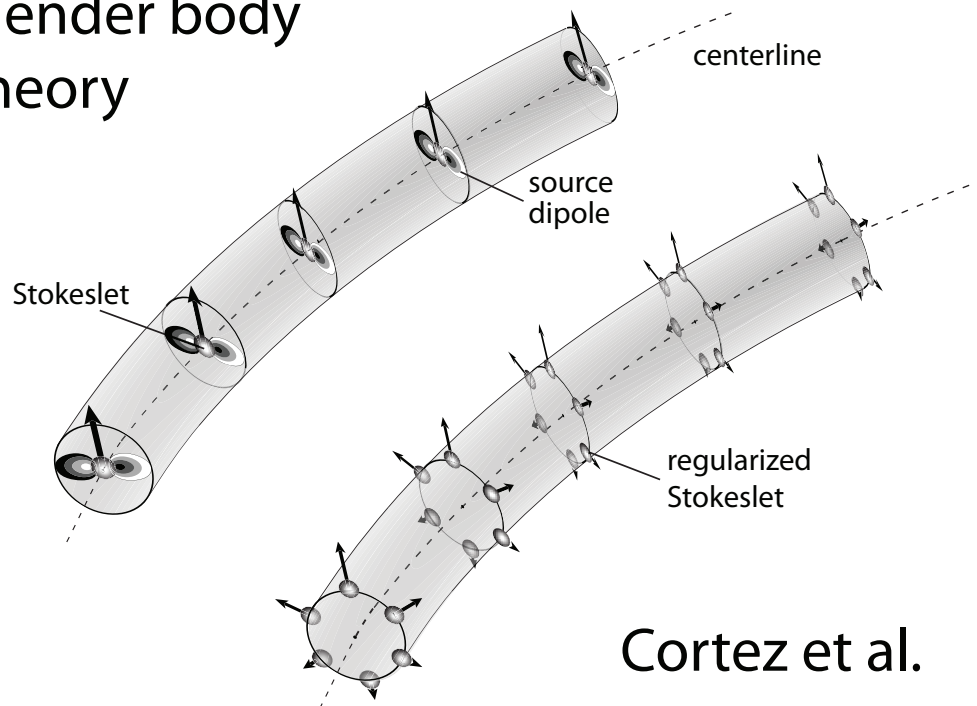


Figure 2.3: a) Slender body theory representation of a flagellum using a Stokeslet and a source dipole arranged along the helical centerline. The combination of Stokeslet plus dipole approximates the fluid response to a flagellum segment. (b) The regularized Stokeslet method of Cortez et al. [26] discretizes the surface of the flagellum and represents each surface element by a *Regularized Stokeslet*, which approximates a Stokeslet but avoids using delta function singularities.

Cortez et al.[26] pursue a different simplification. They fully discretize the surface of an object immersed in a Stokes flow, but represent each surface element by a *regularized Stokeslet*. These differ from a Stokeslet because they are the fluid response to an approximate Dirac delta function, a smooth, radially symmetric cutoff function. The cutoff function they propose, though others are possible, is [26]:

$$\phi_\epsilon = \frac{15\epsilon^4}{8\pi(r^2 + \epsilon^2)^{7/2}} \quad (2.33)$$

where  $\epsilon$  is a small control parameter and  $r$  is the radial distance from the center.

The use of an epsilon parameter has two functions: it eliminates singular and non-integrable kernels in the simulations, and it can play the role of a physical parameter setting the distance over which a force is applied to the fluid[26]. In the limit  $\epsilon \rightarrow 0$ ,  $\phi_\epsilon$  approaches a three dimensional delta function distribution [26], and the regularized Stokeslet becomes the Stokeslet of Eq. 2.5.

To represent a flagellum, regularized Stokeslets can be arranged in circular cross sections along the filament centerline, with the radius of the cross sections representing the filament radius, see Fig. 2.3. I describe the implementation of this method by Dr. Zhang in Sec. 3.1.2.

### 2.2.3 Purpose of the bacterial swimming research

Resistive force theories are, as Lighthill stated, a “suboptimal representation” of flagellar swimming[81]. He recognized that the severe approximations made in obtaining drag coefficients may lead to significant error, but these limitations were offset by the utility of the method. Resistive force theories were developed when experimental techniques and computational capabilities were much less sophisticated than they are now, and they provide simple, calculable expressions for the propulsive force, torque and drag on a low Reynolds number swimmer. Without such analytic expressions, optimization of a mechanical design is difficult even when computations are feasible. Therefore, resistive force theories will continue to be used, typically by using the drag coefficients as free parameters to fit experimental data rather than using either Gray et al. or Lighthill’s expressions.

I will show that the use of resistive force theories in their current form leads to large quantitative errors, even when using the drag coefficients as free parameters. I test the predictions of Eqs. 2.24, 2.25 and 2.27 using experiments and my collaborator’s numerical simulations, and show that they fail to accurately describe the resistance matrix of a flagellum (2.18). Using his simulations, Dr. Zhang also develops a parameterized version of resistive force theory. I describe this development which points out the pitfalls in such a method, but shows how such discrepancies can be resolved to produce a form that accurately describes flagella swimming in a biologically relevant regime.

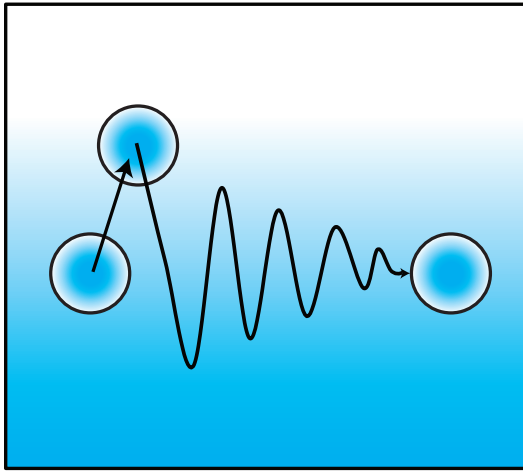


Figure 2.4: Pictorial representation of a fluid parcel in a stratified fluid being displaced upward and then released. The parcel will experience restoring forces from gravity and buoyancy so that it oscillates about its equilibrium height until motion is damped out by viscous dissipation. The natural frequency of oscillation  $N$  of such a fluid parcel is determined by the density profile of the fluid as given by Eq. 2.40.

## 2.3 Theory and motivation for internal wave reflection research

### 2.3.1 Wave equation for internal waves

In a stably stratified fluid such as in the ocean, any vertically displaced fluid parcel experiences restoring forces from buoyancy and gravity, causing it to oscillate about its equilibrium height, and this oscillatory motion allows the propagation of internal waves, see Fig. 2.4.

I can derive a dispersion relation for these waves by considering the Navier-Stokes equations for a non-rotating, inviscid, stratified fluid in the

Boussinesq limit, where the density variation in the stratified fluid is small relative to a reference density, typically that of water, i.e. I can write the density as:

$$\rho(z) = \rho_0 + \rho' \tag{2.34}$$

where  $\rho_0$  is the reference density and  $\rho'$  is a small perturbation. The assumption is that the density is varying slowly with respect to vertical distance, which is certainly true in the ocean where the density varies less than 5% over the entire water column, which is typically 5km in depth, though the density gradient is not constant and some parts of the ocean change much more rapidly[133, 67].

I assume that the fluid is incompressible because I am only concerned with the changes in the density that result from differences such as temperature or salinity as opposed to density variations that result from compressibility. Any fluid parcel raised above its equilibrium height that expands to match the local density will not experience a restoring force and such fluid motion will not support wave propagation. Oceanographers often use the potential density rather than absolute density for this reason. Potential density is the density of a fluid parcel with respect to some reference pressure, typically atmospheric pressure[72].

Likewise, I only want to consider pressure perturbations that support wave motion so I subtract off pressure variation due to hydrostatic balance, i.e.:  $dp/dz = -\rho g$ .

The Cartesian components of the *linearized* Navier-Stokes equations, with gravity antiparallel to the  $z$ -direction, become[72]:

$$\frac{\partial u}{\partial t} = -\frac{1}{\rho_o} \frac{\partial p'}{\partial x} \quad (2.35)$$

$$\frac{\partial v}{\partial t} = -\frac{1}{\rho_o} \frac{\partial p'}{\partial y} \quad (2.36)$$

$$\frac{\partial w}{\partial t} = -\frac{1}{\rho_o} \frac{\partial p'}{\partial z} - \frac{g}{\rho_o} \rho' \quad (2.37)$$

$$\frac{\partial \rho'}{\partial t} - \frac{N^2 \rho_o}{g} w = 0 \quad (2.38)$$

$$\frac{\partial u}{\partial x} + \frac{\partial v}{\partial y} + \frac{\partial w}{\partial z} = 0 \quad (2.39)$$

where  $(u, v, w)$  are the velocity components in the  $x$ ,  $y$ , and  $z$  directions.  $\rho_o$  is the constant reference density, and  $p'$  is perturbation to the pressure and  $\rho'$  is the perturbation density, as defined above.

These equations use the buoyancy frequency, which is defined as:

$$N \equiv \sqrt{-\frac{g}{\rho_o} \frac{\partial \rho}{\partial z}}, \quad (2.40)$$

where  $\rho$  is the density,  $g$  is the gravitational acceleration.

If I also define a horizontal Laplacian operator,  $\nabla_H^2$ , as:

$$\nabla_H^2 = \frac{\partial^2}{\partial x^2} + \frac{\partial^2}{\partial y^2} \quad (2.41)$$

and operate on the sum of (2.35) and (2.36), and then use the continuity equation (2.39), I get:

$$\rho_o \frac{\partial}{\partial t} \left( \frac{\partial u}{\partial x} + \frac{\partial v}{\partial y} \right) = -\rho_o \frac{\partial^2 w}{\partial t \partial z} = -\nabla_H^2 p' \quad (2.42)$$

Now taking partial derivatives of the result with respect to time and  $z$  gives:

$$-\rho_o \frac{\partial^2}{\partial t^2} \left( \frac{\partial^2 w}{\partial z^2} \right) = -\frac{\partial}{\partial t} \left( \nabla_H^2 \frac{\partial p'}{\partial z} \right) \quad (2.43)$$

into which I can substitute for the pressure perturbation using (2.37) along with (2.38) to get the following wave equation for internal or gravity waves:

$$\frac{\partial^2}{\partial t^2} \nabla^2 w + N^2 \nabla_H^2 w = 0 \quad (2.44)$$

### 2.3.2 Dispersion relation for internal waves

I now use the standard method to derive the dispersion relation for internal waves: assuming a plane wave solution and seeking a relationship between the frequency and wavenumber. Because (2.44) only depends on  $w$ , I can use, without loss of generality, a plane wave aligned in the  $x$  direction that has the form:

$$w(x, z, t) = A \exp(i(k_x x + k_z z - \omega t)) \quad (2.45)$$

where  $A$  is the wave amplitude,  $k_x$  and  $k_z$  are the wave numbers in the  $x$  and  $z$  directions respectively, and  $\omega$  is the wave frequency. By inserting this solution into (2.44), I get the dispersion relationship:

$$\omega = \frac{k_x}{\sqrt{k_x^2 + k_z^2}} N = \frac{k_x}{|\vec{k}|} N \quad (2.46)$$

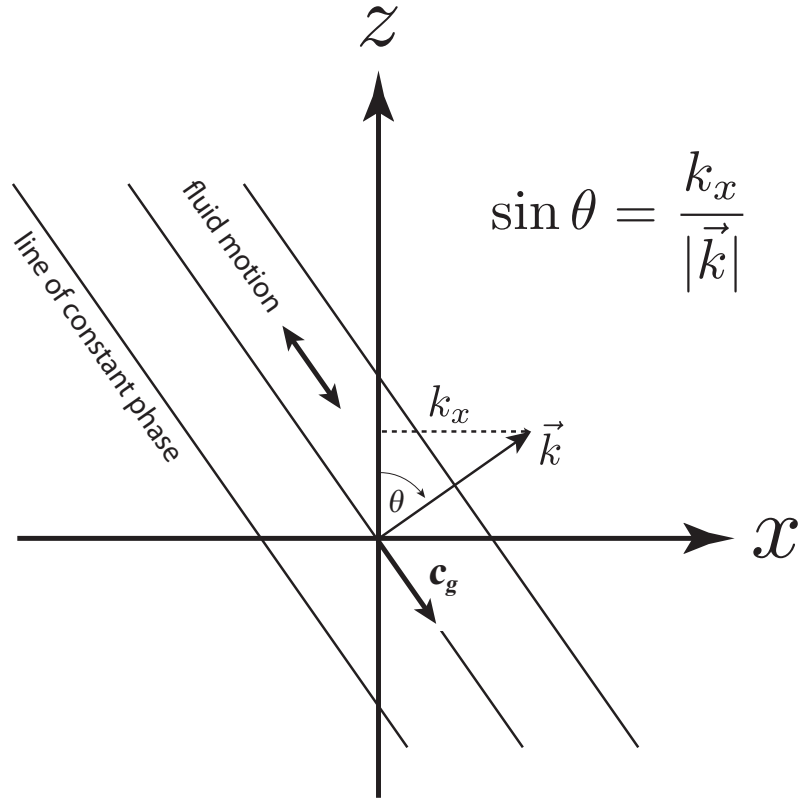


Figure 2.5: Schematic of an internal wave beam. The beam energy is propagating in the direction of the group velocity  $\mathbf{c}_g$ . Fluid motion is oscillatory along the lines of constant phase, and the lines of constant phase move in the direction of the wavenumber  $\vec{k}$ . We define  $\theta$  as the angle of  $\vec{k}$  with respect to the vertical so that the dispersion relation (2.46) can be written as in (2.47). Note that group velocity  $c_g$  and energy propagate at an angle  $\theta$  with respect to the *horizontal*.

As shown in Fig. 2.5, the ratio of  $k_x$  to the magnitude of the wavenumber  $|\vec{k}|$  is the sine of the angle of the wavenumber with respect to the vertical, so I can rewrite (2.46) as:

$$\omega = N \sin \theta, \quad (2.47)$$

where  $\theta$  is the angle of  $\vec{k}$  with respect to the vertical. The dispersion relation (2.47) is unusual because frequency and wavenumber are only indirectly related. An internal wave beam is a packet of plane waves that all have same frequency, but different wavenumbers. The various wavenumber components in a beam must all have the same frequency because components at different frequencies would travel at different angles and diverge in space.

### 2.3.3 Internal wave reflection

In the absence of nonlinear effects, an internal wave beam reflected by a topographic slope must have the same frequency after reflection; hence it propagates at the same angle with respect to the vertical as the incident beam, regardless of the angle of the topography from which it reflects, see Fig. 2.6, which uses the notation of [126]).

The reflected wave beam has a width and wavenumber profile different from the incident beam because the two beams propagate at the same angle,  $\theta_r = \theta_i$  (Fig. 2.6). From ray theory and geometry, the wavenumbers are related by:

$$\frac{k_i}{k_r} = \frac{\sin(\theta_i - \alpha)}{\sin(\theta_r + \alpha)}. \quad (2.48)$$

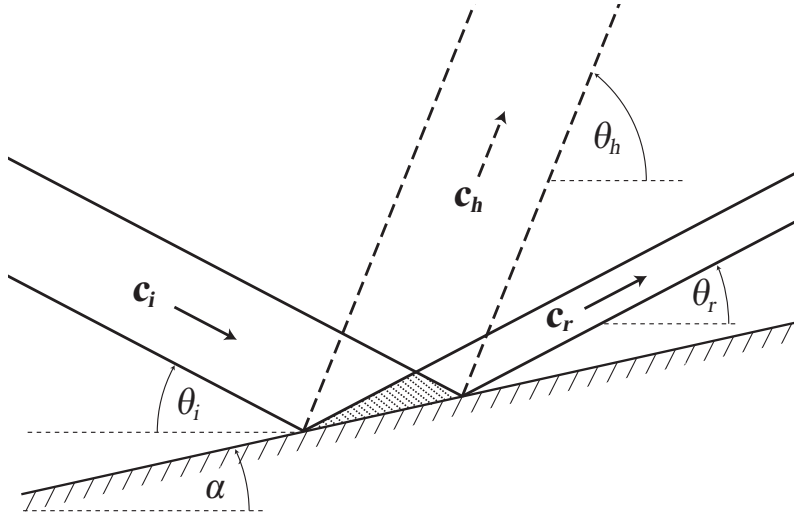


Figure 2.6: Schematic showing the reflection of an internal wave beam from a boundary at an angle  $\alpha$  relative to the horizontal. The incoming and reflected wave beams are at angles  $\theta_i$  and  $\theta_r$ , respectively, which by the dispersion relation (1) are equal because the frequencies  $\omega_i$  and  $\omega_r$  are the same. However, the width and wavenumber of the reflected beam are different than those of the incident beam, as given by (3). The second harmonic wave beam (shown by the dashed lines) is generated by nonlinear interaction between the incoming and reflected wave beams, which occurs mainly in the overlap (shaded) region. The harmonic propagates at an angle given by  $\sin \theta_h = 2\omega/N$ . The group velocities,  $\mathbf{c}_i$ ,  $\mathbf{c}_r$  and  $\mathbf{c}_h$ , indicate the direction of energy propagation.

The narrower reflected beam has higher energy flux than the incident beam because the reflected beam is confined within a smaller region. I test the predicted wavenumber relation (2.48) in the experiments and simulations described in Section 5.2.2 and, surprisingly, as I shall show, (2.48) *fails* to describe my results even for my lowest intensity incident beam.

### 2.3.4 Harmonic generation theories

Two approaches have been taken to predict the topographic angle yielding the maximum intensity of the second harmonic. Phillips [101] reasoned that if the fluid is inviscid and nonlinear interactions are weak, the nonlinear process will occur through a resonant triad; that is, a new wave will be generated from the interaction of two internal waves as either the sum or difference of the frequency and of the wavenumber,

$$k_3 = k_1 \pm k_2 \quad \text{and} \quad \omega_3 = \omega_1 \pm \omega_2. \quad (2.49)$$

Thorpe [126] assumed that harmonic waves result from a resonant triad forming between an incoming *plane wave* and the wave's primary reflection. He used boundary conditions to show that the only angle that satisfies the resonant triad condition is:

$$\alpha_{Thorpe} = \tan^{-1} \left[ \left( \frac{\sin\theta_i}{2\cos^2\theta_i} \right) \sqrt{-3 + 4\cos^2\theta_i} \right]. \quad (2.50)$$

Although I am concerned with *wave beams*, i.e., a packet of plane waves rather than a single plane wave, I will examine the possible applicability of Thorpe's

analysis to my data.

In a different approach, Tabaei et al. [121] derived a relation for internal wave reflection from a sloping boundary by asymptotically matching solutions in the near and far fields. They considered that for a wave beam, resonant triads can form between any of the components of the incoming and reflected wave beams. For a beam with a Gaussian cross-beam profile in wavenumber space, the energy of the second harmonic diverges as the angle of the boundary approaches the wave propagation angle[121]. Prior to Tabaei et al., the study by Dauxois and Young of near-critical reflection showed that nonlinear and viscous effects heal the singularity that occurs at the critical angle [29]. Thus, the energy will not diverge but will have a large finite value when

$$\alpha_{Tabaei} = \theta_i. \tag{2.51}$$

### 2.3.5 Purpose of the internal wave study

Much of the basic physics of internal waves is not thoroughly understood including the reflection of wave beams from boundaries. The Thorpe and Tabaei et al. predictions were developed in the limit of zero viscosity and weak nonlinearity, and differ significantly, especially for large beam angles. For example, for an incoming wave beam with  $\theta_i = 22.7^\circ$ ,  $\alpha_{Thorpe} = 8.2^\circ$  and  $\alpha_{Tabaei} = 22.7^\circ$ . My experiments and simulations are undertaken to determine which prediction is more accurate. I also investigate the effects of strong nonlinearity on harmonic generation because, as stated above, internal wave

beams in the ocean are often strongly nonlinear whereas theories assume at most weak nonlinearity. I show that these theories fail to describe my data and I find an empirical, geometric relationship between the wave beam and the boundary angle where maximum harmonic generation occurs for more strongly nonlinear wave beams.

## Chapter 3

### Methods

#### 3.1 Bacterial Swimming

##### 3.1.1 Experiment

I was assisted by a fellow graduate student Chih-Hung Chen in gathering some of the most recent experimental measurements and I also worked with a 380N student, Yider Lin, who helped construct early prototypes of the experimental system. However, the experimental system and data collection techniques were designed and constructed primarily by me.

The bacterial swimming experiments are performed in an 80-liter tank (52 cm  $\times$  49.5 cm  $\times$  33 cm high), which I constructed using four 31 mm thick acrylic slabs for the walls and a 6.35 mm piece of tempered glass for the bottom. The tank is filled with silicone oil (Clearco Polydimethylsiloxane 100,000 cSt) of density 970 kg/m<sup>3</sup> and a dynamic viscosity  $\mu = 1.0 \times 10^{-3}$  kg/(m·s) at 22°C, about 100,000 times that of water. I confirmed the viscosity of the fluid using a cone and plate viscometer, but relied on the manufacturers stated viscosity temperature dependence of  $1.00 \times 10^{-5}$  g/(cm·s) per °C, and stated thermal expansion of  $9.4 \times 10^{-4}$  m<sup>3</sup>/m<sup>3</sup> per °C. We measure the temperature of the silicone oil using a calibrated thermistor (Barnant Model 600-1075

LogR Thermistor/Datalogger) and adjust the values for viscosity and density accordingly.

I construct model flagella from type 304 stainless steel welding wire with a cross-sectional radius of 0.397 mm. The welding wire, straight prior to forming, is wrapped around aluminum mandrels machined with a Computer Numerical Controlled lathe to create helical v-shaped grooves of varying wavelengths on rods with radius 6.4 mm and length of either 152.5 or 305 mm, see Fig. 3.1.

The 304 stainless steel wire is rigid enough to withstand repeated lowering and raising into the very viscous silicone oil and the forces exerted by fluid during the measurements without changing shape significantly. However, the stiffness of the wire also makes it difficult to form around the mandrel, so the flagella lengthened when removed from the mandrel, uniformly increasing the wavelength and decreasing the radius even though they were annealed in an oven at  $350^\circ$  for two hours. Fulling annealing the stainless steel would melt the aluminum mandrels. However, the wavelength and radius varied less than  $\sim 1\%$  along the length of a given flagellum.

In the wavelength dependence measurements, the the helical radii were ( $R=6.3\pm 0.4$ ) mm, the lengths were  $L = (130\pm 5)$  mm and wavelengths ranged from  $2.25R < \lambda < 15.3R$ . In the length dependence measurements with constant wavelength, the radii were  $R = (6.6\pm 0.2)$ mm, the wavelength was  $\lambda = (2.42\pm 0.02)R$  and the lengths ranged from  $8R < L < 27R$ .

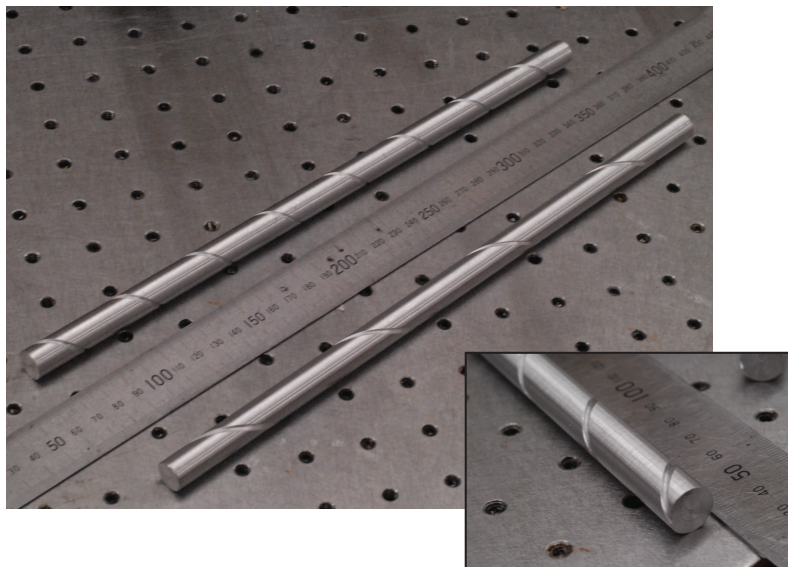


Figure 3.1: Image of two aluminum mandrels used to form the flagella. The mandrel on the left has a wavelength  $\lambda=3R$  and the one on the right has a wavelength  $\lambda=6R$ , where  $R$  is the radius of the mandrel. The wire is wrapped around the mandrels while the mandrels are held in by a collet in a lathe. The lathe is switched into neutral and rotated by hand. The wire is attached at the tip using a plate and screws, and at the end using a screw inserted into a threaded hole machined near the groove.

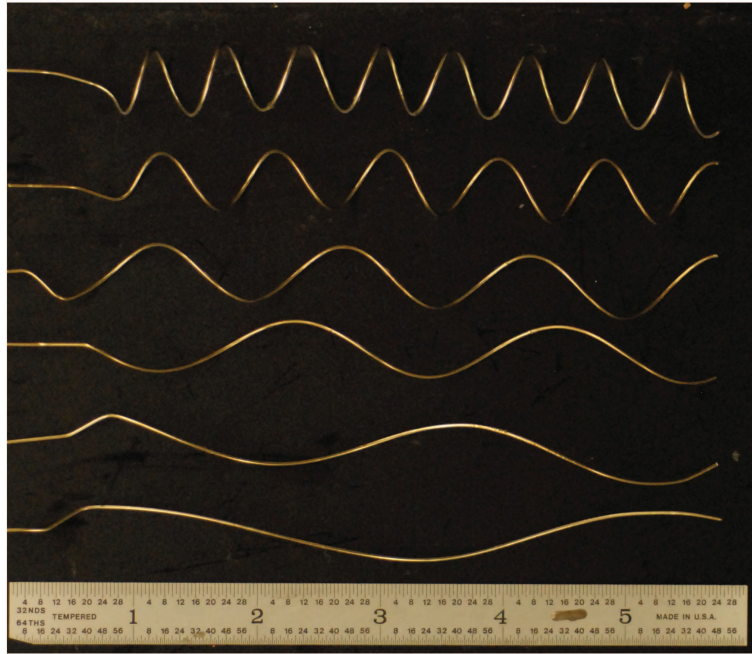


Figure 3.2: Image of flagella used in the length-dependence study formed using the mandrels in Fig. 3.1 using stainless steel welding wire. The wire is annealed on a mandrel for two hours at  $350^{\circ}\text{C}$  and left to cool for 24 hours, which helps it take the form.

### 3.1.1.1 Propulsive Force Measurements

Measuring the propulsive force requires rotating the flagella while immersed in the silicone oil, so I built a body from a block of acrylic (89 mm x 38 mm x 35 mm) to house a small, reversible motor (Pololu 298:1 Micro Metal Gear motor -10 mm x 12 mm x 24 mm), see Fig. 3.3. The motor shaft is aligned with a 12.7 mm double-shielded stainless ball bearing at the end of the acrylic block. The 298:1 gearbox on the motor provides sufficient torque to rotate the flagellum without requiring a large body to enclose it. The motor is driven at different speeds with a controller ( Pololu TRex Jr Dual Motor Controller DMC02A) that adjusts the voltage and current to the motor in response to a control voltage. A 6.35 mm stainless steel shaft adapter extends through the bearing connecting the motor shaft inside the body to the flagellum outside of the body.

To measure the generated force, the swimmer is attached to a 9.5 mm diameter down rod extending from a structure above the tank, as shown in schematically in Fig. 3.4. This vertical rod has a horizontal cross-rod fitted into two ball bearings (VBX R6 3/8" x 7/8" x 7/32" Full Ceramic Miniature Ball Bearing), forming a T-shape to constrain the swimmer to movement along one direction. The distance from the bearings' center of rotation to the the center of an attached flagellum is 325 mm. A load cell (Omega LCL257) is attached to the top of the down rod, 25.4 mm above the bearings' center of rotation. The load cell allows for a maximum deflection of 1.27 mm when a full scale load of 2.52 N is applied. The swimmer can rotate at most 3° at

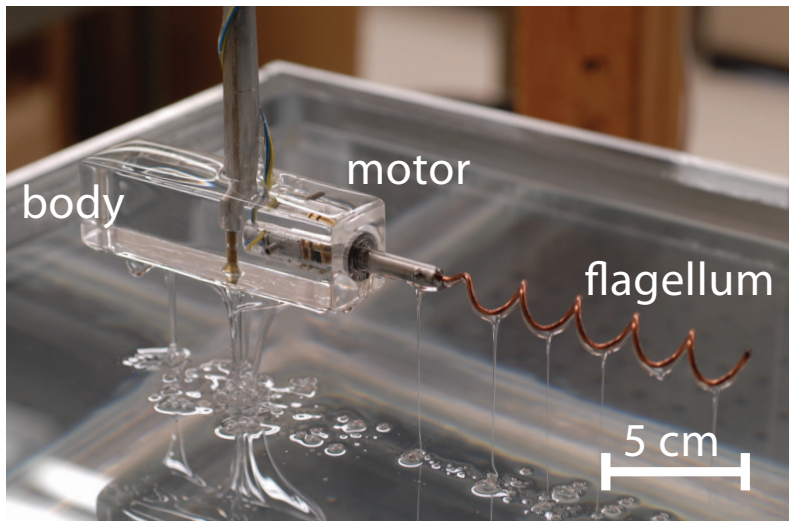


Figure 3.3: Image of robotic bacterium used for the propulsive force measurements. The body is shown with a flagellum made from copper welding wire that has a diameter twice that of the flagella made from the stainless steel wire. The body is machined from a block of acrylic and a gear motor is inserted into a cavity behind the sealed ball bearing at the rear. A shaft adapter connects the motor to the flagella, which rotates at a frequency of  $\sim 0.5$  Hz. The fluid is silicone oil with a viscosity  $10^5$  times that of water to achieve a Reynolds number of  $10^{-2}$ , similar to that of a bacterium.

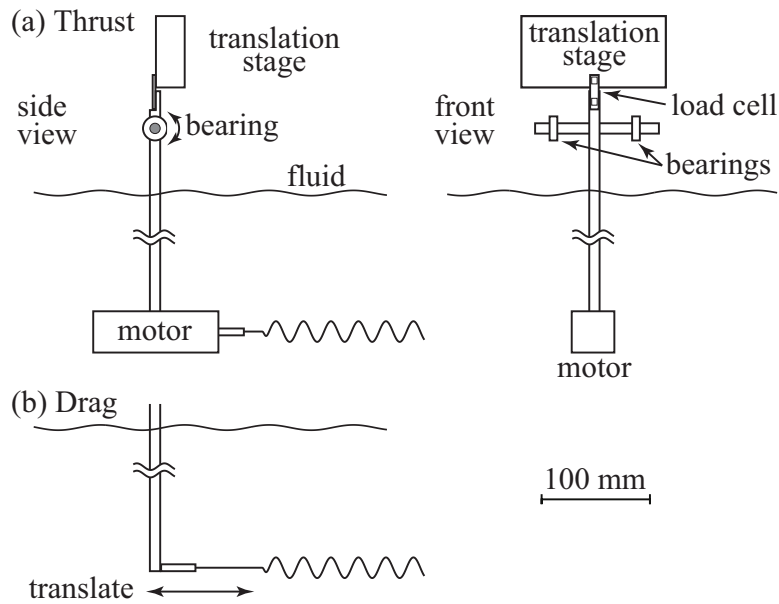


Figure 3.4: Schematic of experimental apparatus: (a) Side and front view of setup for propulsive force measurements. (b) Side view of setup for drag measurements.

the bottom end of the down rod, i.e. a total deflection of 16.5 mm. There is a small ( $<1\%$ ) error introduced by this setup because the propulsive force does not remain perpendicular to the load cell. However, this error is offset by the force amplification provided by the torque arm ( $\sim 10X$ ), which reduces the relative error inherent in the load cell. The manufacturer's stated error is 5% of full scale and nonlinearity is  $<1\%$ .

The load cell is connected to an amplifier/driver (Omega DP25B-E-A 1/8 DIN Process Meter and Controller) that provides an excitation voltage and amplifies the signal from the load cell. The amplified signal is recorded on a computer using a digital data acquisition board (National Instruments

NIDAQ 6008 USB ) and a Matlab-based GUI computer program built for the purpose.

We calibrate the load cell while the body is immersed in the silicone oil. This is necessary because the body's buoyancy affects the calibration. We then attach a string to the down rod above the fluid line and pass it over a low-friction bearing outside the tank. We measure the output voltage from the load cell for multiple weights and fit the data to a line, which gives a calibration constant of volts per newton. The calibration constant changes depending on the orientation of the apparatus with respect to gravity and other factors. Consequently, it is re-calibrated whenever the setup changes significantly.

The data acquisition board also provides motor speed control via an analog output port. However, the motor response is not linear with respect to the control voltage. Consequently, we record movies with a digital camera (Logitech Quickcam Pro 9000, 1920x1080 resolution) using the same Matlab GUI as is used for data acquisition. We simultaneously record load cell and video data for approximately 200 seconds and analyze the movie pixel data using Matlab's built in Power Spectral Density function. Averaging the  $\sim 10^3$  spectra from the region of the image containing the flagellum significantly reduces random error, and the composite spectrum generally has a single peak and its harmonics with the primary peak three to four orders of magnitude above the noise in the signal. The rotation frequencies were  $\sim 0.50$  Hz with a typical half-width of  $\sim 0.01$  Hz, see Fig. 3.5(a).

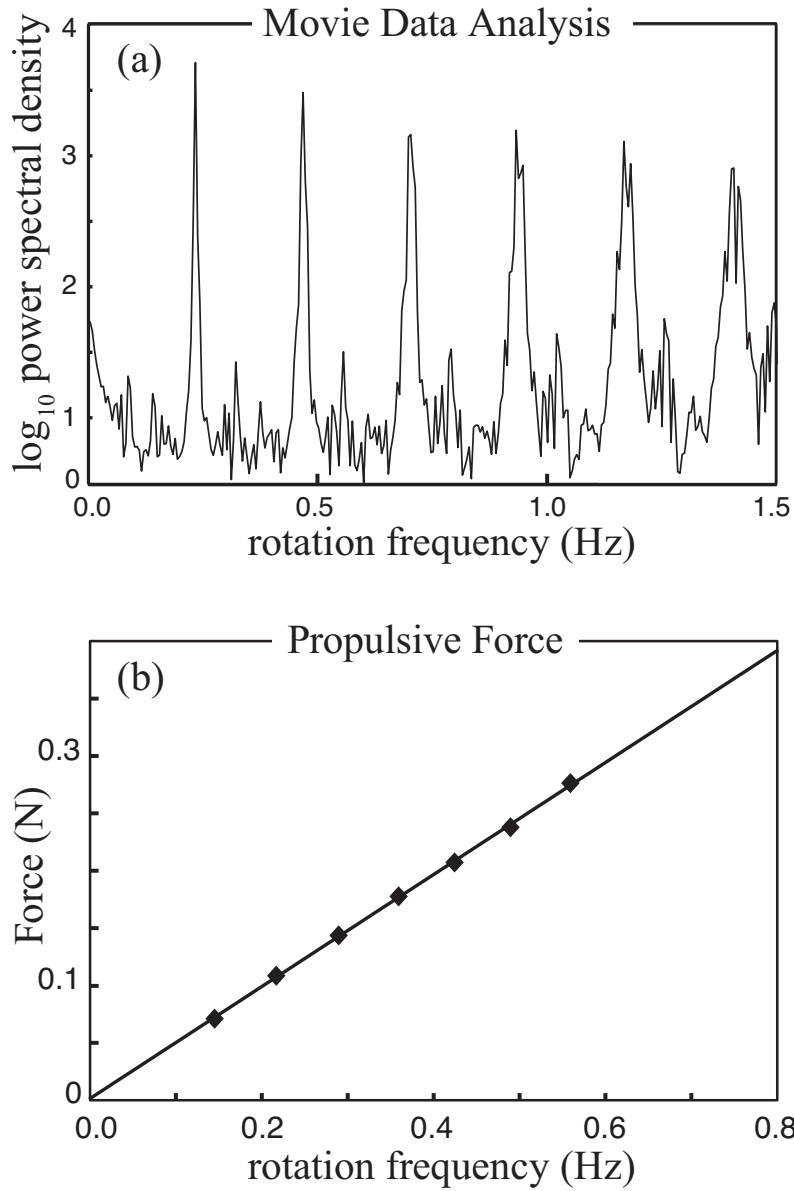


Figure 3.5: Sample dataset for propulsive force measurements for a flagellum with  $R=6.1$  mm,  $a=R/16$ ,  $\lambda=6.2$  R, and  $L=22$  R, showing: (a) the frequency spectrum obtained from analyzing a movie of the rotating flagellum, (b) the force per unit frequency from multiple measurements of propulsive is determined by the slope of a line fit to the data.

For each flagellum, we measure the propulsive force for clockwise (CW) and counterclockwise (CCW) rotation for six to seven rotation speeds in each direction. We fit the data in each direction separately to a line as shown in Fig. 3.5(b). The average slope of these two lines provides the force per unit frequency for the flagellum. Typical variation between CW and CCW rotation is  $\pm 2\%$ .

### 3.1.1.2 Drag Measurements

To measure the drag on a translating flagellum, we use the same load cell as for propulsive force measurements. However, the entire load cell assembly is mounted to a horizontal translation stage that travels parallel to the axis of the flagellum and perpendicular to the load cell. The 0.3 mm/turn drive screw for the translation stage is driven by a stepping motor (Parker-Hannifin GT6 Controller and OS21-B Stepping Motor), giving computer control of the translation velocity. We must recalibrate the load cell since the acrylic body is not used.

The flagellum is mounted onto to a different 9.5 mm diameter down rod that has no body and just a 6.35 mm diameter adapter mounted perpendicular to the down rod into which the flagellum is mounted, see Fig. 3.4.B. We then drag the rod, shaft adapter and flagellum through the fluid for 70 mm and measure the drag force via the load cell.

Six to seven measurements are made at different translation velocities in both the flagellum-first and rod-first directions. We separately fit the data

to lines with the average slope giving the final drag force force per unit velocity. However, this signal includes the drag from the down rod and adapter which must be independently measured and subtracted from the force measured with the flagellum attached. We use the same procedure of multiple measurements fitted to a line to measure this background value in each direction. Typically, the background is 70% of the total signal.

### **3.1.1.3 Torque Measurements**

We use a torque sensor (Magnova MLY Torque Transducer) to measure the torque required to rotate the flagella. The maximum torque it can measure is  $\pm 25$  mNm and the manufacturers stated accuracy is  $\pm 1\%$  of full-scale. The torque transducer has two external shafts connected internally using a "magneto-elastic" active shaft that emits a magnetic field proportional to a torsional load. The magnetic field is measured using Hall probes inside the housing, see Fig. 3.6. The transducer is calibrated by the manufacturer, which we verified using known loads. The calibration was very stable, remaining the same even after loads in excess of the 100% of full scale were applied, so frequent recalibration is not necessary. The output from the torque transducer is amplified by a manufacturer-supplied amplifier board and then read using the same data acquisition board and Matlab GUI program used for the load cell measurements.

In contrast to the orientation for propulsive force and drag measurements, the flagellum during torque measurements is mounted vertically using

a straight down rod to which the flagella are mounted using the 6.35 mm diameter adapter, see Fig. 3.6. The flagellum is adjusted so that it is at mid-depth in the tank, about 10 cm from both the top and bottom boundaries.

The stepper motor is used to rotate the flagellum giving precise control of rotation rate so no frequency analysis is required. Again, multiple measurements at different rotation speeds are made and fit to a line, giving the torque per unit frequency in each direction which is averaged. There is also a background offset in this measurement. The torque created by rotating the down rod and adapter alone must be subtracted from the value measured when the flagella are attached and is measured using the same technique. The background here is smaller than in drag measurements, around 25% of the total signal.

All propulsive force and torque data vary linearly with frequency, and all drag data varies linearly with translation velocity, with less than 1% variance in the slope returned from the the fits.

### **3.1.2 Numerical simulations**

Professor Zhang's numerical simulations use the Regularized Stokeslet Method of Cortez et al.[26] to calculate propulsive force, torque and drag on a flagellum. This method is an approximation of the Stokeslet representation of a body in a low Reynolds number flow, as described in Sec. 2.2.2.

The numerical scheme uses a boundary integral method to calculate the solution to the Stokes equations. Regularized Stokeslets are added to the

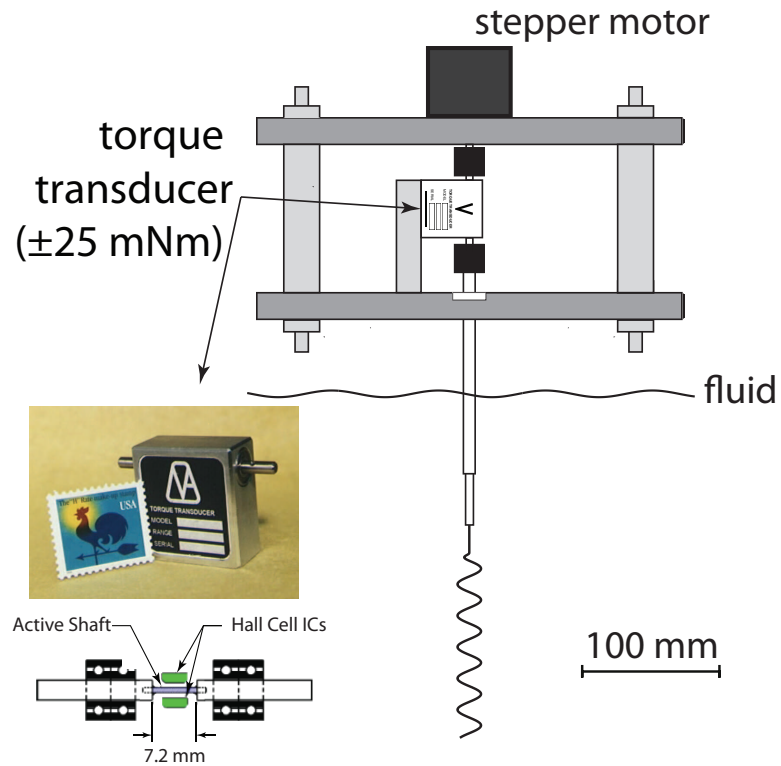


Figure 3.6: Schematic of experimental apparatus for measuring torque. The flagellum is driven with a stepper motor giving computer control of its rotation rate. We use a Magnova MLY torque transducer calibrated by the manufacturer, which relies on a magnetic field generated by the active shaft when a torsional load is applied. The magnetic field is read using Hall effect probes.

R.H.S. of the momentum equation to represent an immersed flagellum with boundary  $D$ . The analytic solution is:

$$\int u_j(x)\phi_\epsilon(x - x_0)dV(x) = \frac{1}{8\pi\mu} \int_{\partial D} S_{ij}^\epsilon(x, x_0)f_i ds(x) \quad (3.1)$$

where  $f_i$  is the  $i$ th component of the force exerted by the fluid on the body (in Stokes flow  $f_i = -g_i$  where  $g_i$  is the  $i$ th component of the force of the body on the fluid) and  $S_{ij}^\epsilon$  is the Green function satisfying:

$$u_i = \frac{1}{8\pi\mu} S_{ij}^\epsilon(x, x_0)g_j \quad (3.2)$$

He then discretizes Eq. 3.1 and solves it numerically using Gaussian quadrature for Regularized Stokeslets arranged in circular cross sections along the helical centerline, with the radius of the cross sections representing the filament radius, see Fig. 2.3.

He uses six Regularized Stokeslets per cross section and uses about 400 cross sections per flagellum. The value of  $\epsilon=0.01$  gives good results, as shown in [26]. Once the  $g_i$  are determined, they are summed appropriately to give the total propulsive force, torque and drag for a given flagellum geometry rotating at a given rate.

## 3.2 Internal Wave Reflection

### 3.2.1 Experiments

Experiments are performed in a 250-liter glass tank (90 cm  $\times$  45 cm  $\times$  60 cm high) filled using the double-bucket method [97] to create a linearly

stratified fluid, see Fig. 3.7. As shown in [97], a stratified fluid with an arbitrary density profile can be constructed using two reservoir tanks and two pumps. The double-bucket method solves the differential equations necessary to specify the density gradient as a function of the two starting volumes and concentrations in the reservoir tanks. Tank 1 is saltier than tank 2, and is pumped into tank 2 at a rate specified by the algorithm while tank 2 is continuously stirred. The mixed solution in tank 2 is then pumped into the bottom of the experimental tank at some other specified rate. Tank 2 has a uniform instantaneous salt concentration and density during the process (assuming the mixing is fast enough) and is pumped at the rate necessary to create the desired density profile in the experimental tank.

However, for construction of a linear density gradient, there is a simple solution to the differential equations in the double-bucket method. Tank 1 is filled with a solution that has the highest density desired in the experimental tank, and the mixed tank is filled with an equal amount of fresh water. The pump rate from tank 1 into the mixed tank 2 is held equal to the pump rate from the mixed tank into the experimental tank. The resultant density profile is linear and varies from the starting density of tank 1 at the bottom to the density of fresh water at the top.

In practice, keeping the pump rates equal is difficult. Our experimental tank is on an optics table, and the reservoir tanks are on the floor. Thus, there is an increasing pressure head on the pump from tank 2 into the experimental tank as the volume of tank 2 decreases and the volume of the experimental

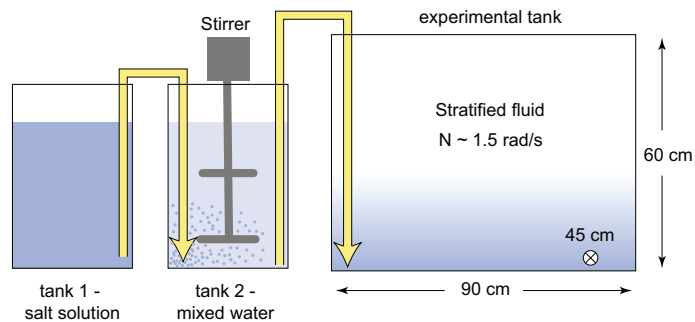


Figure 3.7: Setup for the double-bucket method: the denser, salty water in tank 1 is pumped into tank 2, the mixed tank, which is continuously stirred. A second pump draws water from the mixed tank and pumps it into the bottom of the experimental tank. The pump rates are determined using the method of [97], which specifies the rates based on the instantaneous salt concentration necessary in the mixed tank to achieve the desired density profile in the experimental tank.

tank increases. The pump rate between tank 1 and tank 2 also changed as the volume of the two tanks decreased even though the tanks had the same volume. Thus, the pump rates required constant adjustment to keep them equal. However, one pump may be eliminated from the setup and replaced with a siphon between tank 1 and tank 2. A siphon can be used because the volumes of the reservoir tanks should be equal at all times during the filling. The advantage of the siphon is that no matter how the pump rate from tank 2 into the experimental tank varies, the flow rate in the siphon between reservoir tanks responds accordingly, ensuring that the result is a linear density gradient.

Filling the experimental tank requires about 25 kg of salt (NaCl). The salty water in the bottom of the tank has viscosity about 30% higher than the

fresh water at the top of the tank. However, changes in viscosity are less than 10% within the region studied in the middle of the tank. The density profile, measured with a density meter (Anton Paar Model DMA 35), is typically linear within 1%. The density change from the top to the bottom is about  $\Delta\rho = 140$  kg/m<sup>3</sup>, which corresponds to a density gradient of  $\partial\rho/\partial z = 250$  kg/m<sup>4</sup> and a buoyancy frequency  $N = 1.57$  rad/s (period  $T = 4$  s). The internal waves were observed to propagate in straight lines, indicating constant  $N$ . The value of  $N$  used in comparison of experiment and simulation was deduced from the wave propagation angle rather than from the measurements of the density as a function of height.

A collimated internal wave beam is generated using a wavemaker similar to the one invented by Gostiaux et al. [47]. A former Masters student, Daniel Kiefer, originally constructed the wavemaker and I made small modifications to its design. The wavemaker consists of a stack of five identical acrylic plates (15 cm  $\times$  15 cm  $\times$  0.6 cm), separated by 0.25 cm and housed in a parallelepiped open-sided box (see Fig. 3.8). A helicoidal rotating camshaft constructed from a stainless steel shaft and plastic Delrin discs as shown in the figure is inserted through rectangular holes in the plates. The size in one dimension of the rectangular hole is the same as the diameter of the discs on the camshaft ensuring that the plate must move with the disc as the camshaft rotates. The discs on the shaft are shifted by a phase  $\Delta\phi$  relative to each other, which determines the shape of the forcing. I used  $\Delta\phi=45^\circ$  to achieve a half-sine shape to the edge of the plates. The radius of the disc determines the oscillation

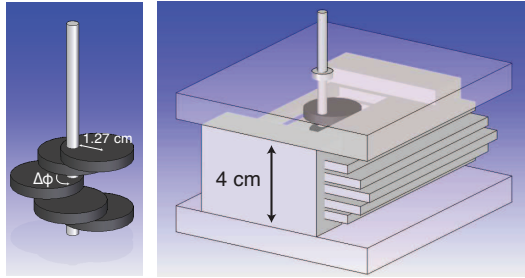


Figure 3.8: The wavemaker consists of five acrylic plates in box (right) driven by a camshaft (left) using a computer-controlled stepper motor. The desired beam profile is generated by selecting the angular difference  $\Delta\phi$  between successive cams. In this example,  $\Delta\phi = 45^\circ$ , which creates a half-sine wave configuration.

amplitude of the plates (1.27 cm). The camshaft is inserted through bearings seated in the top and bottom of the enclosing box, and the camshaft is rotated by a computer controlled stepper motor giving precise control of the frequency.

In the tank the wavemaker is pointed in the direction of the excited wave beam. When the frequency and therefore the wave beam angle change, the wavemaker tilt angle is adjusted accordingly. The wave beam reflects off an acrylic plate (40 cm  $\times$  20 cm  $\times$  0.6 cm) mounted in the tank. Measurements were made for plate angles ranging from zero (horizontal) to the critical angle where the wave beam angle  $\theta_i$  equals the plate angle  $\alpha$ ).

Particle image velocimetry is used to measure the velocity field. The fluid is seeded with  $\text{TiO}_2$  tracer particles (5-10  $\mu\text{m}$  diameter). The  $\text{TiO}_2$  is originally powdered with a typical grain size of 1-3  $\mu\text{m}$ . We achieve larger diameters preferable for the experiments by mixing 1 g of  $\text{TiO}_2$  into 1 L of

water and allowing it to rest for about one week. The  $\text{TiO}_2$  sediments to the bottom of the vessel and aggregates into larger size grains. The aged solution is then agitated gently to suspend the particles in solution without breaking apart the conglomerates. Approximately 40 ml is added to the experimental tank after the filling tank. Because the  $\text{TiO}_2$  is more than four times as dense as the water (4.2 g/ml), the largest particles ( $\sim 25 \mu\text{m}$  diameter) sediment to the bottom of the tank within about 30 minutes to 1 hour. Different size particles sediment at different rates, which allows me to change the size particle used for flow visualization by waiting more time if the particles are too large. If the particle size becomes too small, I can also adjust the laser brightness to increase the signal from smaller particles until I get good results from the particle image velocimetry.

A 532 nm wavelength laser (Coherent Verdi 5 W) green laser set at 0.2 to 0.5 W is used to produce a 0.5 cm thick light sheet that illuminates the tracer particles in a vertical plane. The tracer particle motion in a 25 cm  $\times$  25 cm region is imaged with a 10 bit digital camera (Cohu 1100, resolution: 1004  $\times$  1004 pixels).

The instantaneous velocity field is extracted from consecutive image pairs using the Correlation Image Velocimetry (CIV) algorithm of Fincham and Delerce [35] obtained from <http://coriolis.legi.grenoble-inp.fr/spip.php?article3>. The algorithm is run with a Matlab interface, and the velocity field is stored in a NetCDF file. Data analysis is done in Matlab either using the UVMAT interface or my own Matlab codes.

I take a pair of images separated by 35 ms, and then take a new pair of images after a longer period. Typically pairs of images are separated by 1/20 of the period of the internal wave being studied, a value determined empirically in previous studies by other researchers in my group. Each frame is divided into  $50 \times 50$  pixel regions that are analyzed by correlating the motion of particles in one region into another region across successive image pairs. The first image from a pair is correlated with the first image of the next image pair taken, and the second image is correlated with the second image from the next pair, giving two measurements at effectively the same instant of time, which are averaged to reduce random error. The algorithm returns the confidence of the correlation fits along with velocity vectors implied by the correlations. The NetCDF file includes the  $x$  and  $z$  direction velocity components and the  $y$  direction vorticity.

I measure the number of pixels per centimeter by imaging a ruler immersed in the fluid near where the reflection process occurs and use the time separation of the image pairs to convert the CIV output, which is returned in units of pixels/(image pair separation), into physical units.

The theoretical predictions described in Sec. 2.3.4 and the numerical simulations described in Sec. 3.2.2 are two-dimensional, so I need to ensure that my experimental wavemaker produces a wave beam appropriate for comparison. The plates in the wave maker are 15 cm in the horizontal dimension, perpendicular to the vertical light sheet, so I scanned the light sheet across the horizontal extent of the wavemaker. I found that the generated internal wave

beam is essentially two-dimensional  $\pm 6.5$  cm from the center of the wavemaker.

### 3.2.2 Numerical simulations

My numerical simulations use a modified version of a code developed by Barranco and Marcus[9] to which I made further modifications. See Appendix A for details on the changes I made and the details of compiling and running the code.

This pseudo-spectral, fully parallelized code describes a two-dimensional, stratified fluid in the Boussinesq approximation, which is valid for flow in my tank because the variation in density is small. The code solves for the three components of the velocity and the density with a fractional step method. The equations solved are

$$\partial \vec{u} / \partial t = -(\vec{u} \cdot \nabla) \vec{u} - \nabla P / \rho_0 - g \hat{\mathbf{n}}(\rho / \rho_0) + \nu \nabla^2 \vec{u} \quad (3.3)$$

$$\nabla \cdot \vec{u} = 0 \quad (3.4)$$

$$\partial \rho / \partial t = -(\vec{u} \cdot \nabla) \rho + (\rho_0 N^2 / g) u_z \quad (3.5)$$

where  $\vec{u}$  is the velocity,  $u_z$  is the vertical component of the velocity,  $P$  is the non-hydrostatic component of the pressure,  $\rho$  is the non-horizontally averaged density perturbation,  $N$  is the buoyancy frequency as defined in (2.40),  $\hat{\mathbf{n}}$  is a unit vector that points vertically upward (antiparallel to gravity), and  $\nu$  is the kinematic viscosity,  $\nu = \mu / \rho$ .

To generate internal gravity waves, a momentum forcing term similar to that used by Slinn and Riley [115] and Javam et al. [60] is added to the right side of (3.3):

$$\vec{F} = [\nabla \times (\nabla \times \Phi \hat{z})] \cos(\omega t + \phi), \quad (3.6)$$

where  $\omega$  and  $\phi$  are, respectively, the forcing frequency and phase. The amplitude  $\phi_{max}$ , position  $(x_0, z_0)$ , and beam width  $\sigma$  (standard deviation of the Gaussian profile) of the forcing are given through the term

$$\Phi(x, z) = \Phi_{max} \exp\left(\frac{-(x - x_0)^2 - (z - z_0)^2}{2\sigma^2}\right). \quad (3.7)$$

I use the code to solve the full equations (3.3) through (3.5) directly in two dimensions for Reynolds numbers up to several thousand, which is beyond the highest Reynolds number (about 1000) reached in my laboratory experiments. The computations yield the  $x$  and  $z$  components of the velocity and the  $y$  component of vorticity at each grid point, 128 times per wave period. The instantaneous vorticity field of a numerically simulated internal wave field is shown in Fig. 3.9. The forcing is strongest along the wave beam propagation direction (in the second and fourth quadrants with respect to the wave maker), though weaker beams can be seen in the other two quadrants.

The Reynolds number dependence of the results were examined by solving the equations for different values of the the viscosity  $\nu$  and for different beam widths  $\sigma$ . For some tests I use an inviscid version of the code with the no-slip boundary conditions at boundaries A and C replaced with free-slip boundary conditions.

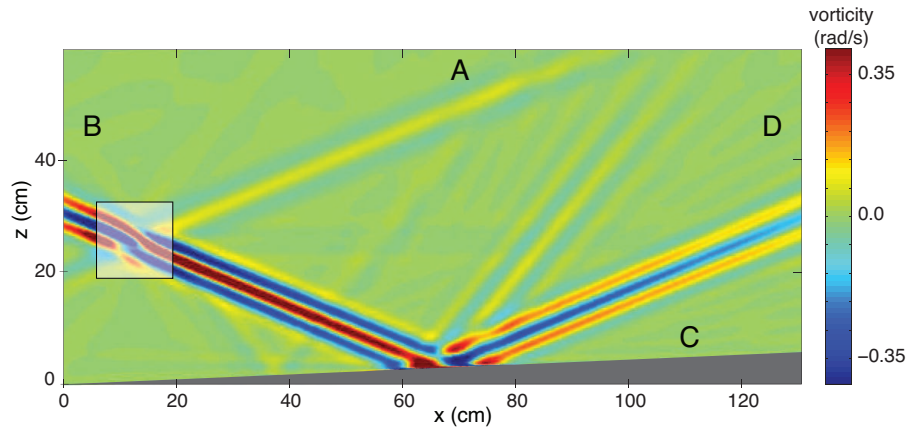


Figure 3.9: Vorticity field computed for  $\theta_i = 22.7^\circ$ ,  $N = 1.63$  rad/sec,  $\nu = 0.01$  cm<sup>2</sup>/s and plate angle  $\alpha = 2.5^\circ$ . The computational domain has been rotated so that the gravity vector points downward; the image has been cropped to fit. The shaded box shows the location of the forcing term. A sponge layer has been added to the no-slip boundary at the top of the domain (boundary A) to absorb the upward propagating wave created by the wavemaker. The simulation is periodic at boundaries B and D, and there is a no-slip boundary condition at boundary C.

I want to measure the intensity of the second harmonic as a function of the bottom boundary angle for many wave beam angles. (The bottom boundary angle is actually set by rotating the gravity vector in the simulations.) I also vary the viscosity, wave beam intensity, buoyancy frequency, spatial location of the numerical wave maker, etc. This study required a total of about 900 simulations, and therefore, management of a large dataset ( $\sim 3$  terabytes). Keeping information organized and easily accessible for analysis is critical so I created a Filemaker Pro database to record the information about each simulation run.

Not only did the database record the parameters used in the simulations, but also an internal script creates an ASCII text file that was read at runtime by the compiled executable, see Fig. 3.10. This relationship ensures that the intended parameters were used in the simulations. The database also improved efficiency and accuracy in data analysis, as described below.

In simulations, the beam intensity and wavelength for a given forcing depended slightly on the domain size and the bottom boundary angle  $\alpha$ . These effects occurred for several reasons. The first is that the distance the wave beam travels from the location of the wavemaker to the bottom boundary changes with  $\alpha$  because the wave beams travel at different angles relative to the bottom boundary in the *unrotated* domain. The longer path for the wave beam means more viscous dissipation and a weaker beam upon hitting the boundary.

Another reason for the differences in the simulations is that the nu-

Date of Simulation 5/18/2009 Group Plate Scan with N=1.63, w=.628 Lambda 2.125  
 Location Run TACC Notes  
 Run ID **Run445**

Copy Parameters  
 Table View

Brunt Vaisala Frequency 1.63  
 Plate Angle XZ 18  
 Plate Angle YZ 0  
 Wavemaker Count 1  
 Wavemakers Phase Difference 3.14  
 Wavemaker Center 1 -14  
 Wavemaker Center 2 0  
 Wavemaker 1 Frequency .628  
 Wavemaker Period 1 10.0050721  
 Wavemaker Amplitude 1 1.8088  
 Wavemaker Wavelength 1 2.125  
 Wavemaker Direction 1 1  
 Wavemaker Rotation Angle 1 22.66  
 Wavemaker MaxMin Count 1 1  
 Wavemaker MaxMin Locations 1 0  
 Wavemaker Standard Deviation 1 .5  
 Wavemaker 1 MaxMin Phase Difference 0.0

Physical  
 1.63065009  
 0.0  
 .5  
 1.40064443

Wavemaker Standard Deviation 2  
 Wavemaker 2 MaxMin Phase Difference 0.0

Desired Distance to Plate 59.8  
 Actual Distance to Plate 43  
 Difference -16.8

Domain Statistics		
Physical Domain X Direction	117.4068	Wavemaker Center X
Grid Points Per Centimeter X	4.36	-45.6582
Physical Domain Z Direction	67.2309	Wavemaker Center Z
Grid Points Per Centimeter Z	3.81	-5.6026
X/Z Aspect Ratio	1.75	
Beam Energy (A*omega^2)	.713361779	

Beam Energy Statistics Incoming Reflected Second Harmonic

Other Program Parameters:  
 Reflection On  Yes  No  
 Side Beam Filtering  Yes  No  
 Side Beam Filter Harmonic 1.0  
 Side Beam Filter Length  
 Side Beam Filter Width 2.4  
 Side Beam Filter Distance Tunnel 3.2

Number of Periods 17  
 Time Step .25  
 Time Steps per Period 1024.0  
 Data Sets to Write 128  
 Periods Data is Written 5  
 nperiod 12.0  
 sampling 8.0  
 Viscosity .010  
 Total Time Steps 69632

Figure 3.10: Snapshot of Filemaker Pro database used to both record the parameters for a given simulation (~900 in total) and to generate an ASCII file read in at runtime. The database also stores results from the analysis and allow for easy sorting and comparison between simulations. Records in the database are related to simulation data organized in directories labeled with the value in the Run ID field, which is highlighted.

numerical code scales the domain in units of the wave maker wavelength as  $\lambda/\sin(\theta + \alpha)$  in the  $x$ -direction and  $\lambda/\cos(\theta + \alpha)$  in the  $z$ -direction, where  $\theta$  is the wave beam angle. These units make specifying the location, rotation angle and other characteristics of the numerical wavemaker easier to implement in the code. The physical sizes of the computational domains for a given wave beam angle were therefore different, depending on  $\alpha$ .

To ensure that all incident wave beams used in a beam angle study were the same, these finite domain effects were controlled by adjusting the amplitude and/or wavelength of the wavemaker in the simulations. This required running a set of test simulations with the same forcing amplitude and wavelength for all the boundary angles. I then measured the intensity of the wave beam at 10 cm from the bottom boundary and adjusted the forcing amplitude and wavelength based on the relative difference between a given wave beam's characteristics and those desired. A Filemaker script was used to automatically generate the corrected parameter files and new simulations were run.

I saw similar finite domain effects in the experiments but could not change the domain or the wavemaker amplitude easily so I adjusted the rotation angle and distance from the reflection boundary until all incoming wave beams for a given study had similar characteristics.

The peak vorticity of the beam incident on the plate was kept at  $\approx 0.3$  rad/s just before hitting the boundary; this corresponds to a velocity amplitude  $|\vec{u}_{max}| \approx 0.3$  cm/s. As Fig. 3.11 illustrates, the beam profiles of the instantaneous vorticity and the velocity amplitude from experiment and sim-

ulation are nearly the same. With so much experimental and numerical data to analyze, I created a GUI program in Matlab integrated with the Filemaker database. The GUI shown in Fig. 3.12 consists of the GUI panel and various functions needed for analysis launched by clicking the associated buttons. The fields in the GUI panel are correlated with the parameters in the input ASCII file used at runtime, and the data are organized in directories by run name so that the GUI can access the data without the user having to manually switch directories. The user need only specify the parent directory as shown in the figure.

The functions include plotting the data at a time specified in the field “File #’s to Plot”. Typically, there were 128 time snapshots taken over four wave periods. There is a function for taking cross sections of the flow variables: velocity, vorticity, and density perturbation, along with cross sections of the velocity amplitude from the curve fitting process in (3.8). Cross sections are obtained for the incoming wave beam, the primary reflection or the second harmonic as specified by a pull down menu in the GUI. The location of the center of the cross section and it’s cross-beam extent is specified in one of three ways. It can be specified as a distance from the bottom boundary, a specific  $(x,z)$  location or interactively using three mouse clicks: left edge, center and right edge. If the center of the cross section is specified as a distance from the bottom boundary, the Cross Section function calculates the location for the cross section center using ray optics based on the location of the wavemaker, bottom boundary angle and size of the domain. Consistent location of the

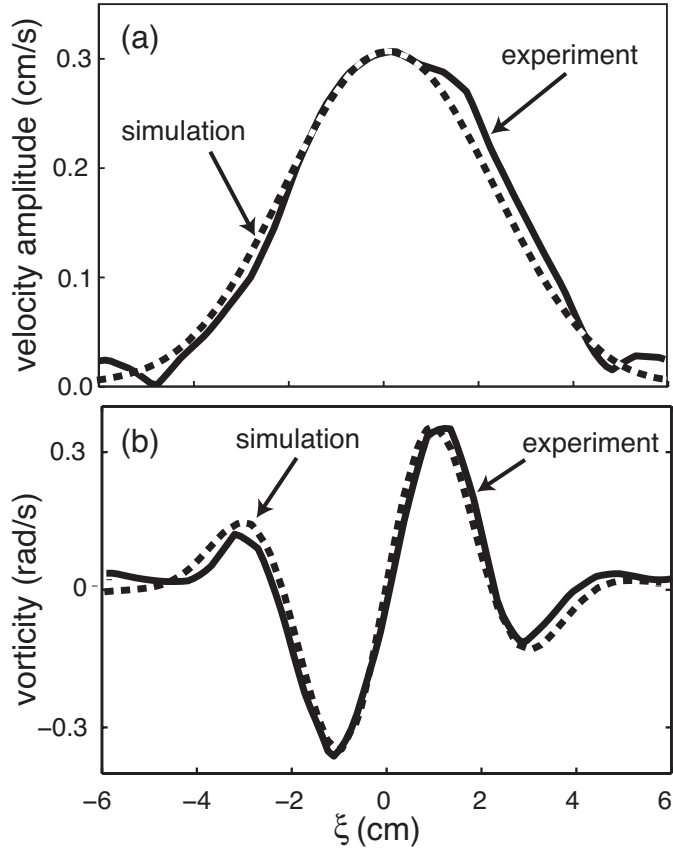


Figure 3.11: (a) The time-independent velocity amplitude cross sections for wave beams under the same conditions as in Fig. 5.1. The cross section from the numerical simulation (dashed line) is accurately Gaussian, whereas there is a small departure from a Gaussian for the laboratory beam (solid line). (b) Vorticity cross section snapshots at the same location.

cross sections is critical to ensure wave beams had similar characteristics upon reflection. Other functions that can be performed on any of the three beams include: fitting the velocity amplitude to a Gaussian, calculating the dominant wavenumber, and calculating the integrated kinetic energy in the beam, as described below.

### 3.2.3 Data analysis

In the experiments and simulations I found that the reflected beam evolved to a steady state in about eight oscillation periods. The analysis was done after waiting 12 wave periods, well after steady state had been achieved but before the reflection region became affected by multiple reflections from side and top boundaries.

To find the steady state velocity amplitude in the experiments and simulations, each component ( $u_x$  and  $u_z$ ) of the velocity field is first processed in Matlab using a four-parameter curve fit to

$$u = A_1 \sin(\omega + \phi_1) + A_2 \sin(2\omega + \phi_2), \quad (3.8)$$

where  $u$  refers to one of the two velocity components,  $A_1$  is the amplitude at the fundamental frequency  $\omega$ ,  $A_2$  is the amplitude at the harmonic frequency  $2\omega$ , and  $\phi_1$  and  $\phi_2$  are the corresponding phases.

The curve fitting process begins by creating a three-dimensional array where each slice in the array is a snapshot of the velocity at a given time, launched from the GUI by clicking the Create Time Series button. The user

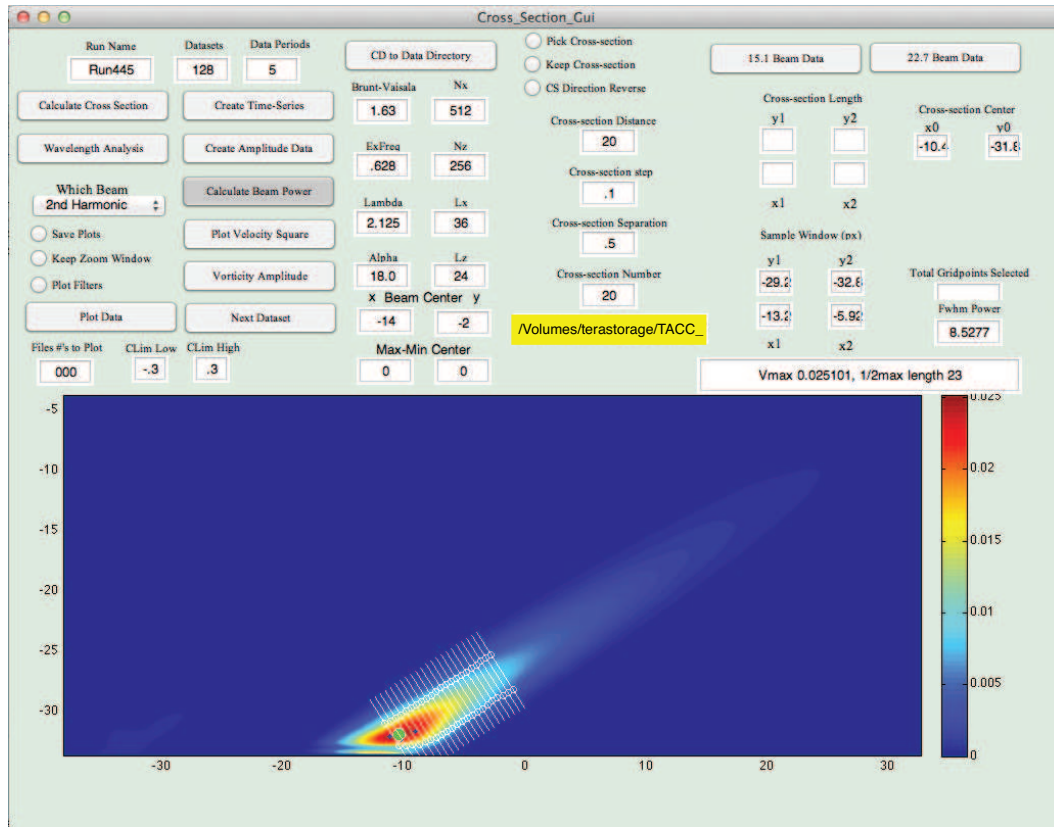


Figure 3.12: Snapshot of Matlab GUI used for data analysis showing the various parameter fields and buttons that launch analysis scripts. The parent directory is specified in the highlighted field and the directory with the data to be analyzed is specified in the Run ID field. The data are all stored in directories with the same name as the records in the Filemaker database. Values for the wave beam intensity and other results are returned in the field above and to the right of the figure. The values are also copied to the computer clipboard for easy transfer into the Filemaker database.

picks the region of the computational domain to curve fit by clicking the upper left and lower right corners of a square region in a snapshot of the vorticity field. As shown in Fig. 3.12, large areas of the domain have essentially zero velocity and curve fitting all of such regions increases the computational time considerably so I crop the domain to only the essential areas. The reduced domain size is recorded in the data files saved by the Create Time Series function, information necessary to analyze the data later.

Next, the user clicks the Create Amplitude Data, which performs the curve fit to (3.8) at each computational grid point. The function returns four two-dimensional arrays of: velocity amplitudes  $A_1$ , phase  $\phi_1$ , velocity amplitude  $A_2$  and phase  $\phi_2$ , which are saved into the same directory as the original data in a directory named “Amplitude\_Data”.

The amplitude data are used to characterize the intensity of the wave beams. As a measure of the intensity of the second harmonic wave beam generated by reflection for different plate angles  $\alpha$ , I integrate  $(A_2)^2$  in the approximately rectangular region shown in Fig. 3.13, where the beam amplitude is computed from  $A = \sqrt{A_x^2 + A_z^2}$ .

The resultant kinetic energy depends on the starting point of the integration, so for consistency I use the point of highest kinetic energy as the starting point (cf. Fig. 3.13). The location of maximum kinetic energy was found using  $(A_2)^2$  as the weights in an average over the highest energy region

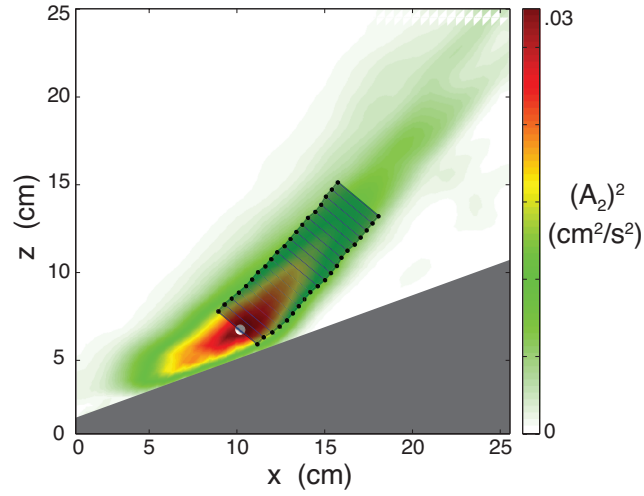


Figure 3.13: Contour plot of the measured second harmonic intensity,  $(A_2)^2$ . The kinetic energy of the beam was integrated over the area where it was above one-half the maximum. Integration starts at the point of maximum kinetic energy within the beam (white circle).

of the beam (dark red in Fig. 3.13),

$$\vec{r}_{maxKE} = \frac{\sum_i A_i^2 \vec{r}_i}{\sum_i A_i^2} \quad (3.9)$$

where  $A_i$  is the amplitude and  $r_i$  is the position coordinate for the  $i$ th grid point within the region.

The Matlab function I wrote for this purpose is launched by “Calculate Beam Power” button in the GUI. The user then clicks the upper left and lower right corners of a box over which the weighted sum of (3.9) is calculated. This eliminates areas of high amplitude outside of the second harmonic beam such as in the boundary layer, ensuring consistency in the location of the starting

point for the integration. Fields in the GUI specify the cross section step, the distance between successive cross sections and the total number of cross sections used in the integration. The cross section step refers to the number of points along the cross section where the data from the nonuniform computational grid is interpolated. Generally, I use interpolation points separated by 1.0 mm and I found no significant difference by increasing the resolution. Similarly, I generally used a cross section separation of 5.0 mm and found no significant difference in decreasing the separation.

The “Calculate Beam Power” function calculates the total integrated kinetic energy in the beam and copies the data onto the computer’s clipboard so that it may be pasted directly into the Filemaker database, eliminating human error in transferring the information. The results of the integration are also stored in the directory with the original simulation data in a directory given a unique ID by Matlab so that the data will not be overwritten if the function is run again.

## Chapter 4

### Bacterial swimming with a helical flagellum

In this Chapter, I investigate how the resistance matrix elements (2.18) depend on helical pitch ( $\lambda$ ) and flagellum length ( $L$ ) using my experiments and Dr. Zhang's numerical simulations. I compare these results to predictions of resistive force theory and analyze the reasons for the failure of resistive force theory. I then describe an asymptotic scaling for  $L \rightarrow \infty$  developed Dr. Bin Liu that explains the length dependence found in my data. Finally, I describe a modified version of resistive force theory developed Dr. Zhang that computes the local drag coefficients by fitting simulation data to resistive force theory equations, which illustrates the pitfalls in this often used technique.

#### 4.1 Comparison of experiments, simulations and resistive force theories

##### 4.1.1 Dependence on helical pitch

To show the dependence on helical pitch, I measured the propulsive force, torque and drag for a set of flagella with the same helical radius  $R = 6.5 \pm 0.2$  mm, filament diameter  $a = R/16$  and axial length  $L = 20R$ , but different helical pitch  $R < \lambda < 16R$ . Experimental and numerical results are shown in

Fig. 4.1 along with the predictions from resistive force theory. Experimental and numerical results are in excellent agreement, generally agreeing within 3%, which demonstrates the accuracy of both our experiments and the Regularized Stokeslet Method [26]. However, the results compare poorly with the widely used predictions of resistive force theory.

For long wavelengths,  $\lambda > 10R$ , theoretical predictions of resistive force theory agree qualitatively with experiments and simulations within a factor of two. However, for flagella with  $\lambda < 10R$ , theoretical predictions for propulsive force diverge even more significantly from experiments and numerics, as shown in Fig. 4.1(a). Resistive force theory (2.24) predicts that  $F_x$  increases without limit as the helical pitch decreases; however, experiments and numerics show that  $F_x$  has a maximum at approximately  $\lambda = 5.5R$ . Theory also predicts much larger drag  $D_x$ , by about a factor of two, for flagella with small wavelengths as shown in Fig. 4.1(c).

In the Stokesian fluid regime, velocity perturbations decay slowly, following power laws, so the interaction between segments is long-ranged. For a flagellum, the separation of filament segments is controlled by pitch. As  $\lambda$  decreases, adjacent turns of the flagellum become closer in space, which leads to stronger hydrodynamic interaction, cf. the red segments in Fig. 2.1. In the small  $\lambda$  limit, a flagellum hydrodynamically becomes a cylinder with zero propulsive force. This rapid decrease in propulsive force for small  $\lambda$  is observed in both experiments and simulations. However, in contrast resistive force theories predict that the propulsive force continues to increase with decreasing

$\lambda$ .

The failure of resistive force theories to describe flagella with shorter wavelengths is especially important with respect to biological flagella. As shown in Tab. 2.1, biological flagella generally have  $\lambda < 11R$ . The failure of resistive force theories is both quantitative and qualitative, indicative that the neglect of hydrodynamic interactions creates serious limitations in the applicability of these widely used theories.

#### 4.1.2 Dependence on flagellum length

I also study the dependence of propulsive force, torque and drag on flagellum length by making measurements on flagella with the same pitch but different axial lengths. In the experiments, I use five flagella with pitch  $\lambda = 2.42 \pm 0.05R$  and axial lengths:  $8R$ ,  $13R$ ,  $17R$ ,  $22R$  and  $27R$ . Numerically, the data has the same pitch and the axial length varied from  $2R$  to  $30R$  in one wavelength increments. Figure 4.2 shows that the experimental and numerical data also agree well in my length dependence study, and generally disagree with resistive force theory. The exception is for axial torque which Lighthill's theory predicts accurately, at least for this wavelength. However, the length dependence predicted by both resistive force theories for propulsive force and drag are significantly different from the experiments and simulations.

Since resistive force theory neglects interactions between flagellum segments, it predicts that propulsive force, torque, and drag are linearly proportional to the flagellum length. However, Fig. 4.2 shows that propulsion

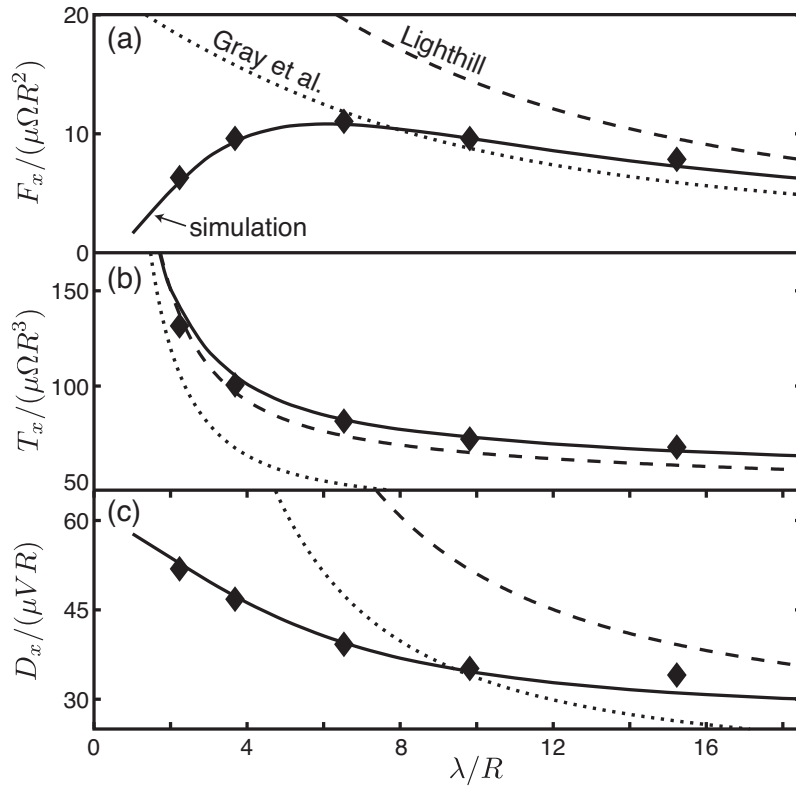


Figure 4.1: Propulsive force (a), torque (b) and drag (c) of flagella with the same helical radius  $a = 1/16R$ , axial length  $L = 20R$  but different helical pitch  $R < \lambda < 20R$ . Numerical results are the solid lines and experimental measurements are the black diamonds. Predictions from resistive force theory are shown as dotted lines for Gray et al.'s[49] drag coefficient expressions and dashed lines for Lighthill's expressions[81].

and drag deviate from a linear dependence, while torque appears linear with respect to flagellum length. Incorrect scalings in resistive force theory result from neglecting hydrodynamic interactions, which I show can be corrected so that resistive force theory is more accurate for long flagella.

## 4.2 Analysis of why resistive force theories fail

### 4.2.1 Asymptotic theory for long flagella

In this section, I describe a theoretical analysis that can correctly predict the length scaling observed in the data. Dr. Bin Liu derived these scalings using Lighthill's slender body theory.

Consider a flagellum parameterized by contour position  $s$  with a length  $L$  much greater than  $R$  and  $\lambda$ . According to Lighthill[81], the local velocity of a segment of the helix located at  $s = 0$  is correlated with the force distribution along the entire filament  $\mathbf{f}(s)$  as

$$\mathbf{u}(0) = \frac{\mathbf{f}(0) \cdot \hat{n}\hat{n}}{4\pi\mu} + \int_{|\mathbf{r}(s',0)| > \delta} \mathbb{J}(s', 0) \cdot \mathbf{f}(s') ds' \quad (4.1)$$

where  $s'$  is a point along the centerline of the flagellum,  $\hat{n}$  is the unit vector normal to the flagellum at  $s'$ ,  $\mu$  is the dynamic viscosity,  $\mathbf{r}$  is the displacement of the segment  $s'$  away from the segment at  $s = 0$ ,  $\delta = a\sqrt{e}/2$  is the natural cutoff,  $\mathbb{J}$  is the Oseen Tensor of (2.7), and  $\mathbf{f}$  is the force per unit length on the flagellum.

For a sufficiently long helix, end effects are minimal so each segment is essentially the same. Therefore, the force per unit length can be written:

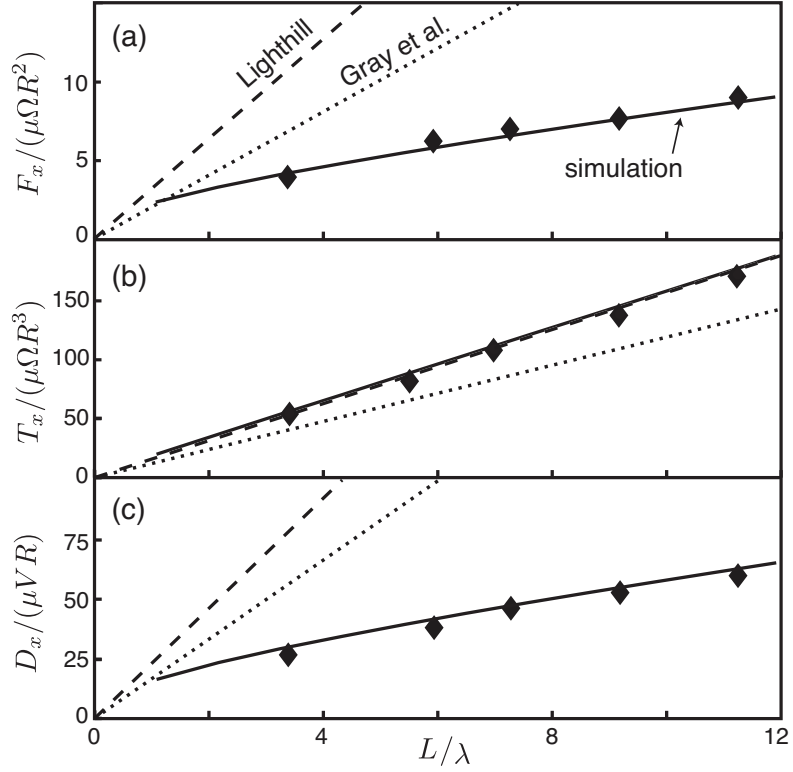


Figure 4.2: Propulsive force (a), torque (b) and drag (c) for flagella with the same helical radius  $a = 1/16R$  and pitch  $\lambda = (2.42) R$ , but different axial lengths  $L$ . Experimental data are shown as diamonds and numerical results are the solid curves. Simulation results are the solid lines and experimental measurements are the black diamonds. Predictions from resistive force theory are shown as dotted lines for Gray et al.'s[49] drag coefficient expressions and dashed lines for Lighthill's expressions[81].

$\mathbf{f}(s) \approx (f_x, f_\Omega \sin \varphi, f_\Omega \cos \varphi)$  where  $f_x$  is the force per unit length in the  $x$  direction and  $f_\Omega$  is the tangential force per unit length perpendicular to the  $x$  direction, which has components in the  $y$  and  $z$  directions, depending on the helical phase  $\varphi \equiv ks \cos \theta$  of the segment. The associated velocity of the helical filament is  $\mathbf{u} = (u_x, \Omega R \sin \varphi, \Omega R \cos \varphi)$  so the velocity formulation from Lighthill's slender body theory (4.1) gives, for the  $x$  direction and tangential velocities respectively:

$$\begin{aligned}
u_x &= (f_x \sin \theta - f_\Omega \cos \theta) \sin \theta + \\
&\int_{k\delta \cos \theta}^{kL} \csc \theta d\varphi \left( \frac{f_x}{\xi} + \frac{f_\Omega \varphi \sin \varphi \cot \theta + f_x \varphi^2 \cot^2 \theta}{\xi^3} \right) \\
\Omega R &= \frac{(f_x \sin \theta - f_\Omega \cos \theta) \cos \theta}{4\pi\mu} + \\
&\int_{k\delta \cos \theta}^{kL} \csc \theta d\varphi \left( \frac{f_\Omega \cos \varphi}{4\pi\mu\xi} + \frac{f_{\text{clockmege}} \sin^2 \varphi + f_x \varphi \sin \varphi \cot \theta}{4\pi\mu\xi^3} \right),
\end{aligned} \tag{4.2}$$

where  $\xi(\varphi, \theta) \equiv \sqrt{4 \sin^2(\varphi/2) + \varphi^2 \cot^2 \theta}$ , which means  $1/\xi$  approaches  $1/(\varphi \cot \theta)$  as  $\varphi$  increases. It can be shown that the pre-factor of  $f_x$  in the first equation of (4.2) includes an integrand of order  $1/\varphi$ , and thus has an asymptotic  $O(\log(L))$  dependency. All the pre-factors of  $f_x$  and  $f_\Omega$  elsewhere converge for large  $L$ . Therefore, the asymptotic form of (4.2) for large  $L$  is:

$$u_x = A_1 f_\Omega + A_2 \ln(L/L_0) f_x \tag{4.3}$$

$$\Omega R = B_1 f_\Omega + B_2 f_x \tag{4.4}$$

where  $A_1, A_2, B_1,$  and  $B_2$  are constants that will not affect the length scaling. The force per unit length is solved as:

$$f_x = \left( u_x - \frac{B_1}{A_1} \Omega R \right) / [B_2 - \frac{A_2 B_1}{A_1} \ln(L/L_0)] \tag{4.5}$$

$$f_\Omega = \left( \frac{u_z}{A_1} \right) - \frac{A_2}{A_1} \ln(L/L_0) f_x \tag{4.6}$$

This analytical result shows the anisotropic dependencies of the hydrodynamic force on the helix length. The axial force per unit length  $f_x$  decreases logarithmically because the  $\ln(L/L_0)$  term in (4.5) will dominate for very large  $L$ . However, the torque per unit length  $f_\Omega R$  saturates to a constant as  $L$  increases because the term proportional to  $f_x$  in (4.6) is multiplied by the same factor  $\ln(L/L_0)$ . Therefore:

$$F_x \propto L / \ln(L/R) \tag{4.7}$$

$$T_x \propto L \tag{4.8}$$

and

$$D_x \propto L / \ln(L/R) \tag{4.9}$$

The numerical data are re-plotted in Fig. 4.3 with thrust, torque and drag normalized using the scale factors of Eqs. 4.7 to 4.9. For flagella with axial lengths longer than  $2\lambda$ , the scaled values for  $F_x$ ,  $T_x$  and  $D_x$  become independent of axial length  $L$ , showing that these scalings are correct.

#### **4.2.2 Incorporating length scaling and wavelength dependence into resistive force theory**

Other researchers have found that equations 2.24 to 2.27 provide a good framework for describing the motion of sperm [36] and worms [119], but with a catch. In order to fit theory to experimental results, they must treat the drag coefficients  $C_n$  and  $C_t$  as free parameters rather than using Gray or Lighthill's expressions. In this section, I describe work by Dr. Zhang, who uses the same

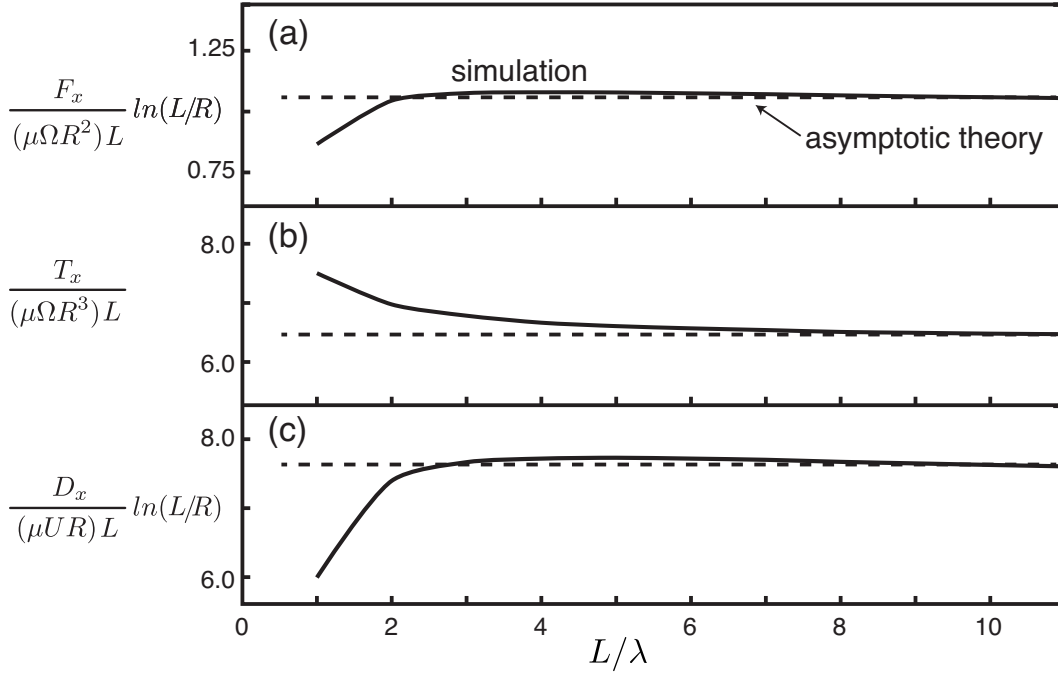


Figure 4.3: Axial length,  $L$ , dependence.  $F_x$ ,  $T_x$  and  $D_x$  are rescaled (see text for details) and plotted as functions of axial length  $L$  in (a), (b) and (c). The solid curves are simulations and the dashed lines are the asymptotic theory from (4.5) and (4.6). All data sets have the same filament radius  $a = 1/16R$ . The helical pitch is  $\lambda = 2.42R$ . For flagella longer than  $\sim 3\lambda$ , the normalized  $F_x$ ,  $T_x$  and  $D_x$  are approximately constant, showing that Dr. Liu's asymptotic theory is correct.

idea and extracts  $C_n$  and  $C_t$  from measurements of  $F_x$  and  $T_x$ . The process leads to an improved methodology for implementing resistive force theory for understanding the dynamics of swimming microorganisms and nanobots.

First, the predictions of resistive force theory (Eqs. 4.10, 4.11 and 2.27) should be modified by the asymptotic scalings (Eqs. 4.7, 4.8, and 4.9) which then gives the following expressions to which the data will be fit:

$$F_x = -(\Omega R) [(C_n - C_t) \sin \theta \cos \theta] \left[ \frac{L}{\cos \theta} \right] \left[ \frac{\ln 30}{\ln(L/R)} \right] \quad (4.10)$$

$$T_x = -(\Omega R^2) [C_n \cos^2 \theta + C_t \sin^2 \theta] \left[ \frac{L}{\cos \theta} \right] \quad (4.11)$$

$$D_x = -S_{drag} V [C_n \sin^2 \theta + C_t \cos^2 \theta] \left[ \frac{L}{\cos \theta} \right] \left[ \frac{\ln 30}{\ln(L/R)} \right]. \quad (4.12)$$

In Eq. 4.10 and Eq. 4.12, the factor of  $\ln 30$  is added to correspond to the magnitudes in the biologically relevant regime:  $20R < L < 40R$ . In this regime, the ratio of  $\frac{\ln 30}{\ln(L/R)}$  is around one, ranging from 0.92 to 1.13.

For a given flagellum, the drag coefficients  $C_n$  and  $C_t$  are computed using the measurements of  $F_x$  and  $T_x$  and Eqs. (4.10) and (4.11). The resultant drag coefficients from a set of flagella with various wavelengths are shown by symbols in Fig. 4.4 (a). However, if I plug the extracted  $C_n$  and  $C_t$  into Eq. 4.12 and compute the drag, it does not match the measured values.

The failure of the parameterized  $C_n$  and  $C_t$  to describe the drag on the flagellum is not a minor point. It means that the method fails to describe

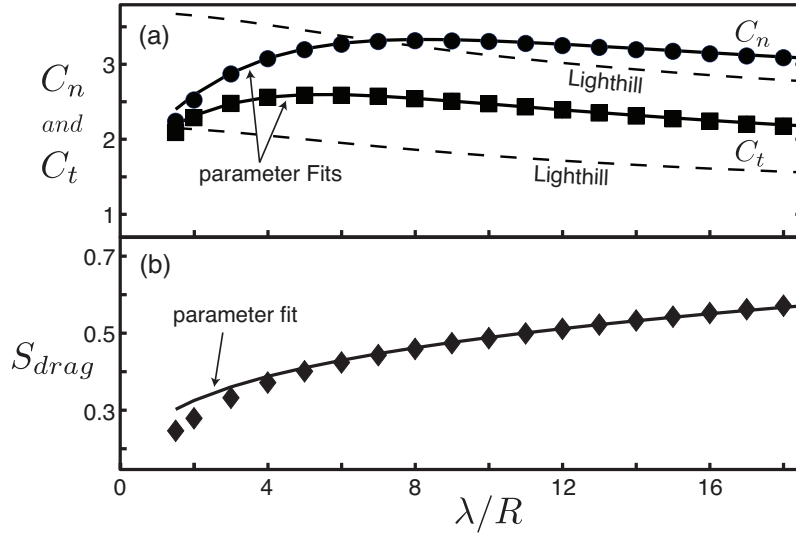


Figure 4.4: (a) Drag coefficients  $C_n$  (circles) and  $C_t$  (squares) from simulations with  $a = 1/16R$ ,  $L = 30R$ , and  $R < \lambda < 20R$ . The solid lines are the new parameterization of these coefficients provided in Eq. 4.13. Lighthill's expressions for  $C_n$  and  $C_t$  are shown as dashed lines. (b) The new drag scaling factor extracted from the same simulations (diamonds) with the parameterization from Eq. 4.15 plotted as the solid lines.

the resistance matrix of the flagellum and does not accurately describe the dynamics.

The problem with using  $C_n$  and  $C_t$  as free parameters to fit experimental data is that the resistance matrix is described by three independent equations, (2.24), (2.25) and (2.27), so three parameters are necessary to properly fit data to these equations. Thus, a new term is introduced,  $S_{drag}$  in Eq. 4.12, having values around 0.5. Extracted  $S_{drag}$  values are plotted as diamonds in Fig.4.4 (b), which shows that they decrease nonlinearly with decreasing helical pitch, as expected because increased hydrodynamic interactions will reduce

the measured drag in a nonlinear fashion.

### 4.2.3 Parameterization of $C_n$ , $C_t$ and $S_{drag}$

The parameterized values for  $C_n$ ,  $C_t$  and  $S_{drag}$  in Fig. 4.4 are for flagella with all the same geometric parameters except for pitch  $\lambda$ . To get general expressions for  $F_x$ ,  $T_x$ , and  $D_x$ , Dr. Zhang sought expressions for  $C_n$ ,  $C_t$  and  $S_{drag}$  as functions of the other geometric parameters. He systematically varied these parameters in his computations of  $F_x$ ,  $T_x$ , and  $D_x$  for flagella in a biologically relevant regime where  $1/10R < r < 1/25R$ ,  $2R < \lambda < 20R$ , and  $15R < L < 40R$ . From each simulation, he computed  $C_n$ ,  $C_t$  and  $S_{drag}$  using Eqs. 4.10 to 4.12. Results for all  $C_n$ ,  $C_t$  and  $S_{drag}$  values are shown in Fig. 4.5 as functions of scaled variables. He found that the following empirical expressions describe the data well:

$$C_t = \frac{2.45\pi\mu}{\ln \frac{0.105\lambda}{a(\cos\theta)^{1.77}}}, \quad (4.13)$$

$$C_n = \frac{4.45\pi\mu}{\ln \frac{0.271\lambda}{a(\cos\theta)^{-6.23a/R+3.1}}}, \quad (4.14)$$

and

$$S_{drag} = (-0.83a/R + 0.3236) (\lambda/R)^{0.25}. \quad (4.15)$$

which are shown by lines in Fig. 4.4.

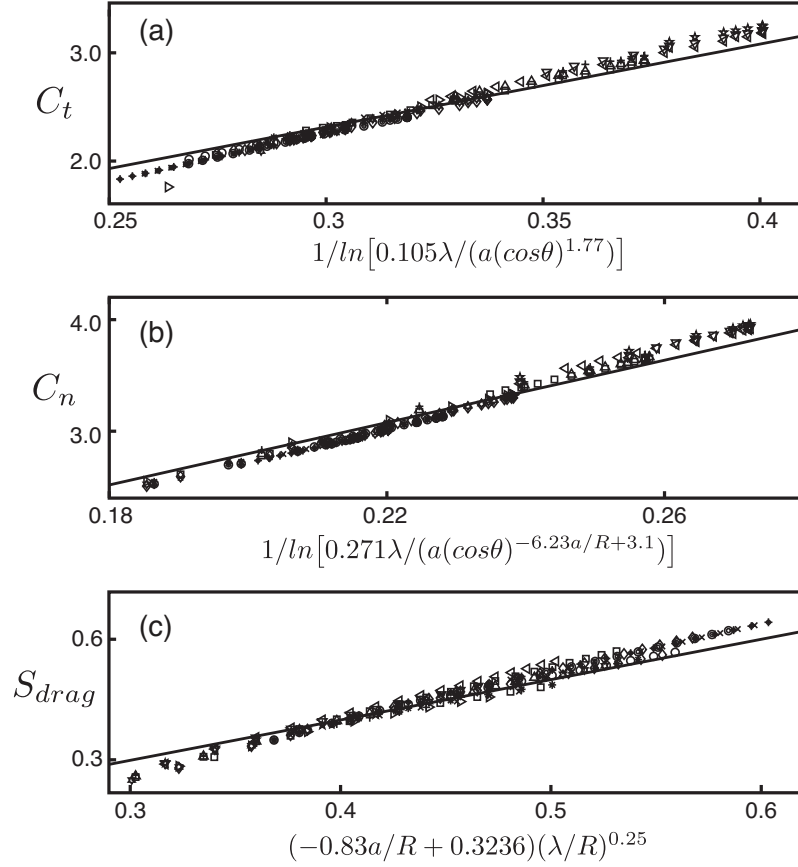


Figure 4.5: Collapse of  $C_n$ ,  $C_t$  and  $S_{drag}$  to functions given by Eqs. (4.13) to (4.15). Different symbols correspond to a specific combination of  $a$ ,  $R$ ,  $\lambda$  and  $L$ . Our study covers a biologically relevant parameter regime of  $1/10R < a < 1/25R$ ,  $R < \lambda < 20R$ , and  $15R < L < 40R$ .

#### 4.2.4 Hydrodynamic efficiency as test of the parametrization scheme

Equations 4.10 to 4.12 coupled with Eqs. 4.13 to 4.15 form a closed system that can predict propulsive force  $F_x$ , torque  $T_x$ , and drag  $D_x$  for any flagellum, i.e., fully determine the resistance matrix. A further test the accuracy of the scheme is to compute the hydrodynamic efficiency as defined by Purcell [106, 117]. Purcell showed that in a low Reynolds numbers flow, the ratio of the power necessary to drive an axisymmetric body to the power generated by an axisymmetric propeller of any shape (including a helix) is maximized when the  $A$ -elements from their respective resistance matrices (Eq. 2.18) are equal. Using this definition, the maximum efficiency possible for a flagellum is given by:

$$\varepsilon = \frac{F_x^2}{4T_x D_x}, \quad (4.16)$$

Dr. Zhang computes efficiency for nine forms of bacterial flagella observed in nature, which vary in radius and pitch angle. The geometric parameters of the flagella, hydrodynamic efficiency from numerical simulations  $\varepsilon_n$ , and efficiency given by his parametrization  $\varepsilon_p$  are shown in Table. 4.1. In all calculations, the filament radius is  $a = 0.01 \mu\text{m}$  and the contour length is  $\Lambda = 10 \mu\text{m}$ , where  $\Lambda = \sqrt{(2\pi R)^2 + L^2}$ . The difference between  $\varepsilon_p$  and  $\varepsilon_n$  is less than 5% except for “coiled” flagella, which have very large pitch angles. In all cases, the “normal” form has the highest efficiency, which is consistent with a recent study by Spagnolie and Lauga[117].

	Peritrichous (multi-flagellated)					Monotrichous (singly flagellated)			
	Normal	Semi-coiled	Curly	Curly-II	Coiled	Normal	Semi-coiled	Curly	Coiled
$R(\mu m)$	0.221	0.257	0.123	0.074	0.689	0.170	0.298	0.132	0.405
$\lambda(\mu m)$	2.284	1.167	1.029	0.961	0.784	1.402	1.177	0.961	1.059
$\varepsilon_n(10^{-3})$	8.840	7.232	7.166	4.431	0.744	8.364	6.507	7.179	3.715
$\varepsilon_p(10^{-3})$	8.895	7.597	7.066	4.575	1.404	8.341	6.980	7.092	4.34

Table 4.1: Geometric parameters and hydrodynamic efficiency of naturally observed bacterial flagella. Geometric parameters are from Spagnolie and Lauga [117] who averaged measurements found in the literature. In all computations, the filament radius is  $a = 0.01 \mu m$  and the contour length  $\Lambda = 10 \mu m$ .

To test the filament radius parametrization scheme, Zhang computes hydrodynamic efficiency of two flagella from Table 4.1 that have the same filament radius  $a = 0.01 \mu m$  and contour length  $\Lambda = 10 \mu m$ , but different helical radii - Peritrichous normal ( $R = 0.221 \mu m$ ) form and curly ( $R = 0.123 \mu m$ ) form. (This is equivalent to varying the filament radius since it is scaled by the helical radius.) The helical pitch is allowed to vary from 0 to 90 degrees, and in both cases, an optimal efficiency appears around  $\theta \approx 41^\circ$ . However, the normal form has a higher efficiency, which is probably the reason this is the form most frequently observed in live bacteria.

The parameterized resistive force theory developed by Dr. Zhang is more accurate than similar efforts of other researchers that failed to consider the full resistance matrix in their analyses. Though the final form of the parameterized coefficients is fairly complicated, they provide a simple method for biologists and designers of nanobots to calculate the resistance matrix of a flagellum without making measurements or conducting simulations.

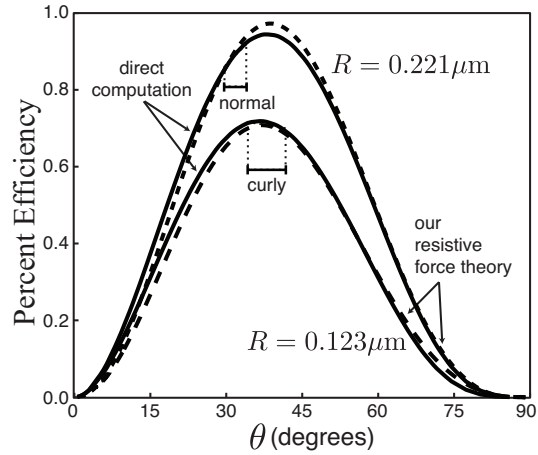


Figure 4.6: Hydrodynamic efficiency of two sets of flagella ( $R = 0.221 \mu\text{m}$ ) and ( $R = 0.123 \mu\text{m}$ ) from numerical simulations (Sec. 3.1.2). In both cases, the filament radius is  $a = 0.01 \mu\text{m}$  and the contour length  $\Lambda = 10 \mu\text{m}$ . Solid lines are directly computed from the numerical simulations and dashed lines are from the new resistive force parametrization scheme. The Peritrichous normal and curly form pitch angles with error bars (from experimental measurements in the literature) are indicated below the  $R = 0.221 \mu\text{m}$  and  $R = 0.123 \mu\text{m}$  curves respectively.

## Chapter 5

# Harmonic generation by internal gravity waves reflecting from a sloping boundary in a density stratified fluid

In this Chapter, I describe the results of my experiments and simulations, and compare them with theoretical predications of Thorpe [126] and Tabaei et al. [121]. Neither theory correctly predicts the boundary angle that maximizes harmonic generation, but I present a heuristic argument for predicting this maximizing boundary angle based on the geometry of the reflection process. I also explore the applicability of the theories to my simulation data in the limit of low viscosity and weak nonlinearity, assumptions made in the development of the theories. The prediction of Tabaei et al. is then predictive of the boundary angle of maximum harmonic generation, but only in the limit of very low intensity wave beams. Finally, I discuss the importance of my results with respect to the longstanding assumption of how nonlinear interactions develop, based on the resonant triad idea of Phillips [101].

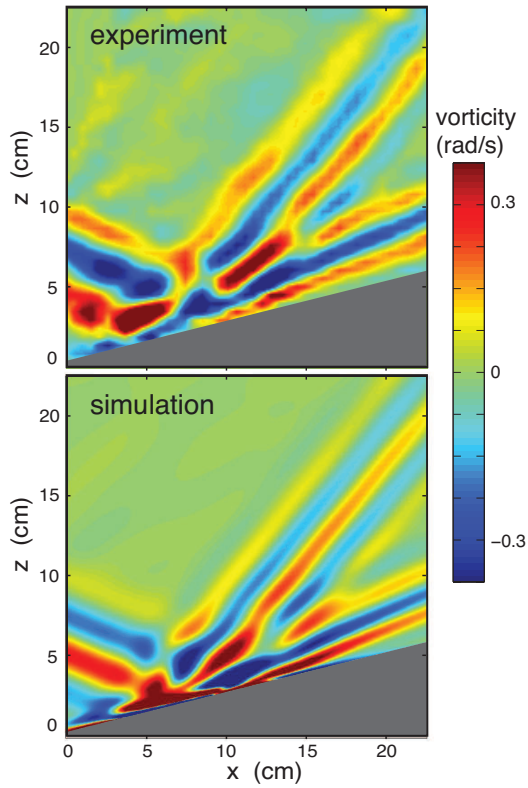


Figure 5.1: Instantaneous experimental and computed vorticity fields for forcing frequency,  $\omega = 0.628$  rad/s,  $N = 1.63$  rad/s,  $\theta_i = 22.7^\circ$ , plate angle  $\alpha = 14.1^\circ$ , and beam amplitude  $A \sim 0.25$  cm/s. In the experiment the spatial resolution was 0.5 cm.

## 5.1 Comparison of experiments and simulations to theories by Thorpe and Tabaei et al.

### 5.1.1 Intensity of second harmonic from experiment and simulation

My experimental and computational results for the vorticity fields of reflecting internal wave beams agree well, as the snapshots in Fig. 5.1 illustrate. The intensity of the second harmonic generated by the beam reflection as the

plate angle  $\alpha$  varied was found in all cases to exhibit a well-defined maximum (Fig. 5.2), which contrasts with an earlier observation [46] that did not detect any boundary angle dependence of the second harmonic intensity. In my and Daniel Kiefer’s experiments and my simulations, the angles determined for the maximum second harmonic intensity agreed within  $1^\circ$ , although the experiments and simulations yielded a somewhat different functional dependence of the intensity on plate angle (Fig. 5.2). This difference arose in part because of the experimental difficulty in maintaining the same incident beam waveform for varying distances between the wavemaker and the reflecting plate for different plate angles; the waveform also depended on the oscillation amplitude of the wavemaker and on finite domain effects, which changed with plate angle. Further, the simulations were two-dimensional whereas the experiments were only approximately so.

### 5.1.2 Quantifying nonlinearity

In all weakly nonlinear theories the amplitude of the second harmonic varies as the square of the amplitude of the incident beam. Figure 5.3(a) shows this expected quadratic dependence for low amplitude incident beams, but for high amplitude incident beams, the amplitude of the second harmonic saturates. To characterize the degree of nonlinearity I use the dimensionless amplitude parameter introduced by Dauxois and Young in a two-dimensional theoretical study of near-critical reflection[29],

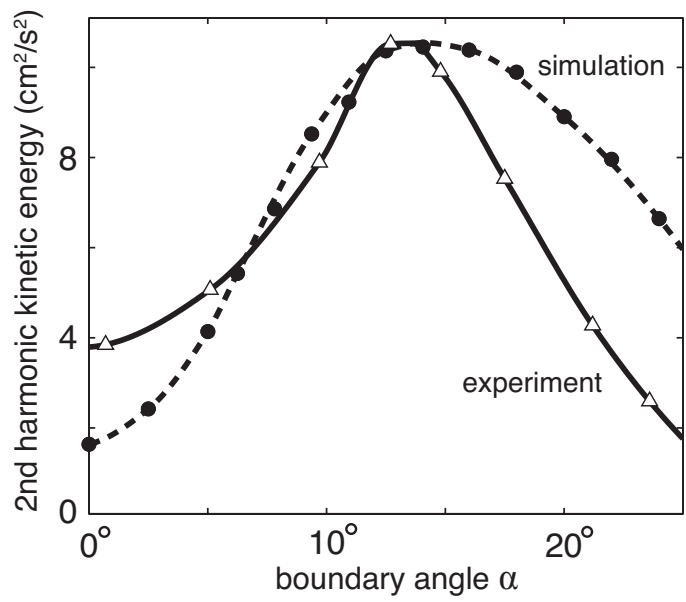


Figure 5.2: Intensity of the second harmonic generated in the reflection of an incident internal wave beam (at  $\theta = 22.7^\circ$ ) from a plate tilted at angle  $\alpha$ . The curves are cubic spline fits to the data. The boundary angles  $\alpha$  where the maxima occur are  $\alpha_{max} = 13.2^\circ$  (experiment) and  $14.1^\circ$  (simulation), far from either the  $22.7^\circ$  predicted by Tabaei et al. [121] or the  $8.25^\circ$  predicted by Thorpe [126].

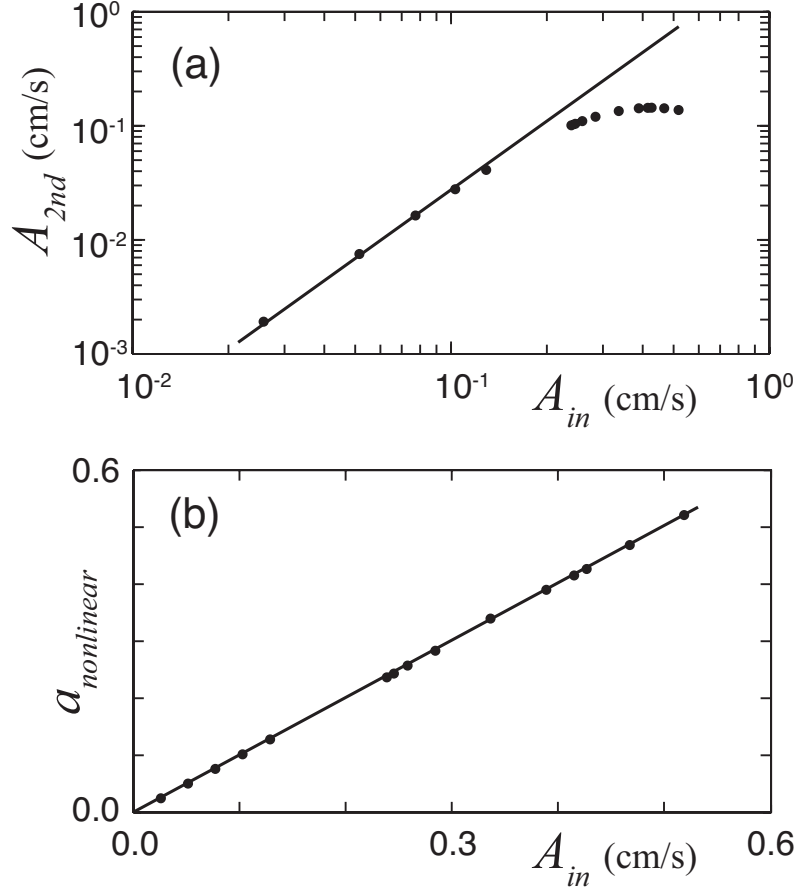


Figure 5.3: (a) The second harmonic amplitude depends quadratically (black line) on the incident wave beam amplitude, up to high amplitudes where the second harmonic determined in the simulations (solid dots) saturates (for a beam incident at  $\theta = 22.7^\circ$  on a boundary at angle  $\alpha = 12.5^\circ$ ). (b) Under the same conditions, the dimensionless amplitude parameter  $a_{nonlinear}$  (Eq. (5.1)) in the simulations varied from 0.01 (very weakly nonlinear) to 0.52 (highly nonlinear), and in the experiments was 0.25 (corresponding to  $A_{in} = 0.25$  cm/s).

$$a_{nonlinear} \equiv \frac{k_{in}^2 \sin[2(\theta + \alpha)]}{2N \sin\theta} \psi_{max} \quad (5.1)$$

where  $k_{in}$  is the magnitude of the wavevector of the incident beam,  $\psi_{max}$  is the maximum amplitude of the stream function, and  $\alpha$  and  $\theta$  are defined in Fig. 2.6. Weakly nonlinear theory should apply when  $a_{nonlinear} \ll 1$ , but in our experiments  $a_{nonlinear} \approx 0.25$ , and simulations were conducted for  $0.01 < a_{nonlinear} < 0.5$  (see Fig. 5.3(b)). I shall show in Section 5.2 that my simulations reveal a significant departure from weakly nonlinear theory even for  $a_{nonlinear} = 0.01$ .

### 5.1.3 An observation-based prediction in accord with experiment and simulation

I find that, for every internal wave beam that I could produce in experiment and for all but the lowest intensity beams in the simulations, the second harmonic generated in reflection has a maximum intensity when the width of this beam is the same as that of the incident beam. This result, found for a wide range of incident beam intensities, widths, and angles, leads to the conclusion from ray theory that the plate angle corresponding to the maximum intensity of the second harmonic beam is given by

$$\alpha_{geom} = \frac{\tan^{-1}(\sin\theta_i)}{\sqrt{1 - 4\sin^2\theta_i + \cos\theta_i}}, \quad (5.2)$$

which is in remarkable accord with my laboratory and computational results (Fig. 5.5(a)). For higher plate angles, those near critical, I observed very

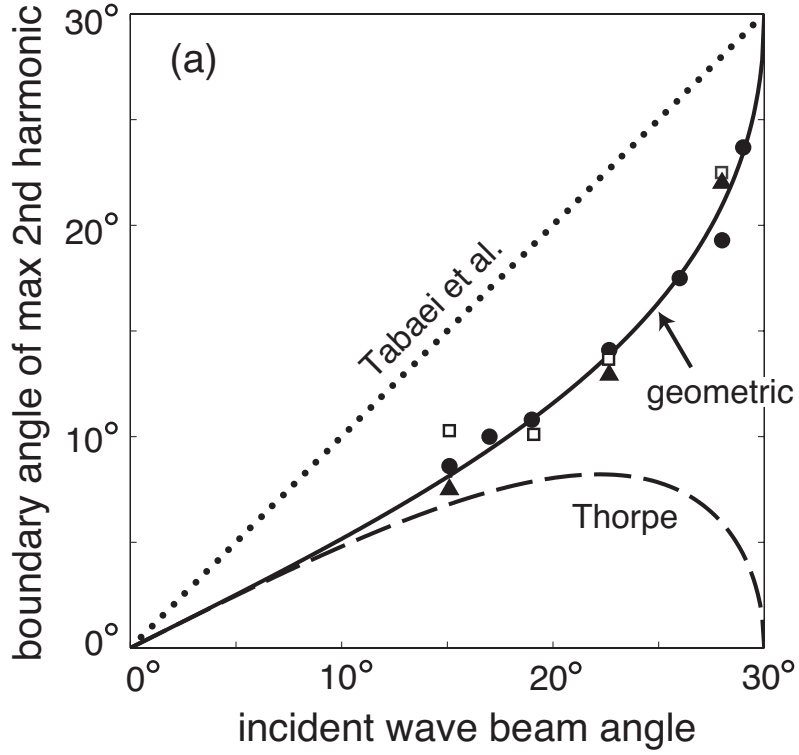


Figure 5.4: The boundary angle corresponding to the maximum intensity of the second harmonic of an internal wave beam reflected from a surface, for incident beam velocity amplitudes  $A = 0.25$  cm/s ( $a_{nonlinear} = 0.25$ ). My laboratory observations (triangles), numerical simulations (circles) with water viscosity ( $\nu = 0.01$  cm<sup>2</sup>/s) and numerical simulations with viscosity reduced by an order of magnitude (open squares) in (a) all agree well with the solid curve (Eq. (5.2)), which was obtained from ray theory, given the observation that the maximum intensity of second harmonic occurs when that beam's width is the same as that of the incident beam. Clearly, these results do not agree with either the Tabaei et al. [121] or the Thorpe [126] theory.

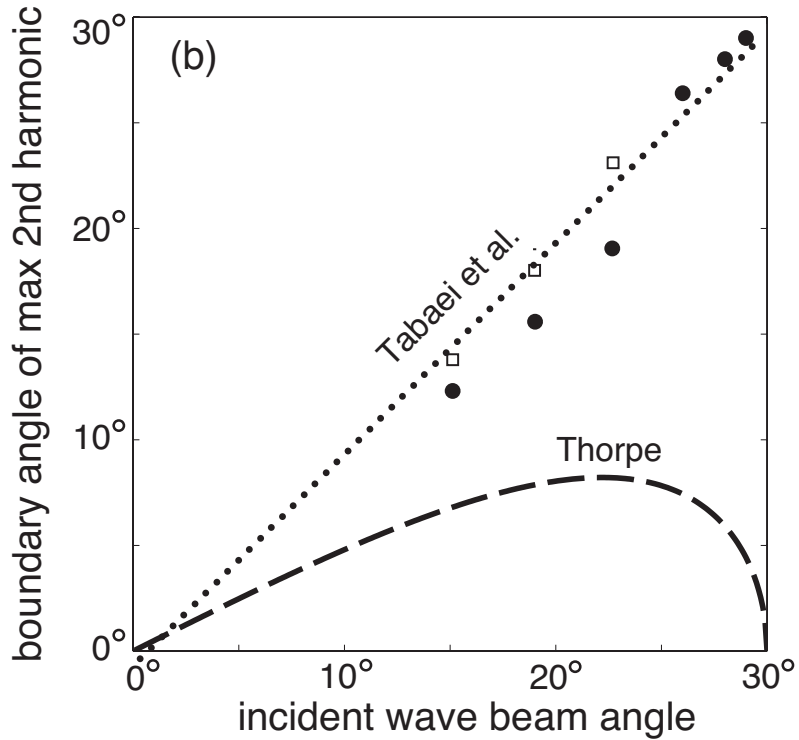


Figure 5.5: Results from numerical simulations for the boundary angle corresponding to the maximum intensity of the second harmonic of an internal wave beam reflected from a surface, for incident beam velocity amplitudes  $A = 0.01$  cm/s ( $a_{nonlinear} = 0.01$ ). These low-amplitude beams agree with the Tabaei et al. prediction for incident beam angles greater than  $\sim 25^\circ$  (solid circles). When the viscosity is reduced from that of water by an order of magnitude, the agreement of the simulation with the Tabaei et al. prediction extends to about  $15^\circ$  (open squares).

weak second harmonic waves and strong mean flows from the reflection region. However, I did not observe density inversions or turbulent events.

## 5.2 Analysis of the failure of weakly nonlinear and inviscid theories

### 5.2.1 Recovery of the Tabaei et al. prediction for low amplitude beams

The analyses of Thorpe and Tabaei et al. (cf. Section 2.3.4) assumed weak nonlinearity and no viscosity. To examine this limit I simulated wave beams of very low intensity ( $A_{in} \sim 0.01$  cm/s,  $a_{nonlinear} \sim 0.01$ ), below the level for which I was able to make accurate measurements in our experiments. The results then agreed with the Tabaei et al. prediction for beam angles down to about  $\theta \gtrsim 20^\circ$ , and reducing the fluid viscosity led to agreement with Tabaei et al. to yet lower beam angles (Fig. 5.5(b)). However, as the wave amplitude was increased,  $\alpha_{max}$  decreased rapidly, departing from the prediction of Tabaei et al. For lower frequency waves, I found that the amplitude of the incident beam had to be even lower for  $\alpha_{max}$  to approach the Tabaei et al. prediction. Tabaei et al. [121] comment that nonlinear effects are generally increased by longer time scales of interaction; this is supported by the dependence on wave period I found.

### 5.2.2 Wavenumber and amplitude of the reflected fundamental beam

The results from my experiments and simulations show that the weakly nonlinear analyses of Thorpe [126] and Tabaei et al. [121] have limited applicability. To understand this result, I measured the wavenumber of the incident beam and the reflected fundamental beam to test the assumption in the Thorpe and Tabaei et al. analyses that the incident and reflected beams have wavenumbers in the ratio given by:

$$\frac{k_i}{k_r} = \frac{\sin(\theta_i - \alpha)}{\sin(\theta_r + \alpha)} \quad (5.3)$$

I determined the wavenumbers of the beams by fitting the cross-sectional profiles of the vorticity to

$$q = q_{max}[exp(-(\eta - \eta_0)^2/2\sigma^2)]sin(k\eta + \phi), \quad (5.4)$$

where  $q_{max}$  is the amplitude of oscillation,  $\eta$  is a coordinate perpendicular to the wave beam propagation direction,  $\eta_0$  is the center of the wave beam,  $\sigma$  is the standard deviation of the wave packet envelope,  $k$  is the dominant wavenumber in the beam, and  $\phi$  is the phase at a given instant in time.

Equation (2.48) predicts that the wavenumber ratio  $k_i/k_r$  should approach zero as the critical angle is approached, whereas my simulations yield a quite different result: the ratio  $k_i/k_r$  remains far above zero as the boundary angle increases toward the incident beam angle, as shown in Fig. 5.6(a). The laboratory measurements of the wavenumber ratio are consistent with the simulations for the same incident beam amplitude. Simulations were then made

with the amplitude parameter  $a_{nonlinear}$  reduced from 0.25, as in Fig. 5.3, to a value of only 0.01, and the viscosity reduced to a value 10 times smaller than that of water, but the wavenumber ratio limit decreased only a small amount, from 0.40 to 0.35.

Another prediction of the Tabaei et al. theory (but not that of Thorpe [126]) is that the amplitude of the reflected wave beam should be given by  $A_r/A_i = \sin(\theta_r + \alpha)/\sin(\theta_i - \alpha)$ , thus diverging at the critical angle. Instead, my simulations yield very different behavior, as Fig. 5.6(b) illustrates. Thus I conclude that even when the theory of Tabaei et al. predicts the angle found for the maximum second harmonic intensity (at low intensities, cf. Section 5.2.1), the predictions about the wavenumber and the amplitude of reflected fundamental wave beam are not valid.

### 5.2.3 Wavenumber of the second harmonic

The analyses of Thorpe [126] and Tabaei et al. [121] predict that a harmonic generated in reflection should have a wavevector component parallel to the boundary that is simply related to the incident beam's wavevector component parallel to the boundary,  $k_{h\parallel} = nk_{i\parallel}$ , where  $n$  is the order of the harmonic. Gostiaux et al. [46] confirmed this prediction experimentally, and our experiments and simulations are also in accord with the predicted relation. It seems plausible that this result, coupled with the  $\alpha_{geom}$  condition (equal beam widths at peak harmonic generation) would lead to a triad relationship between the wavevectors of the incident, reflected fundamental, and reflected

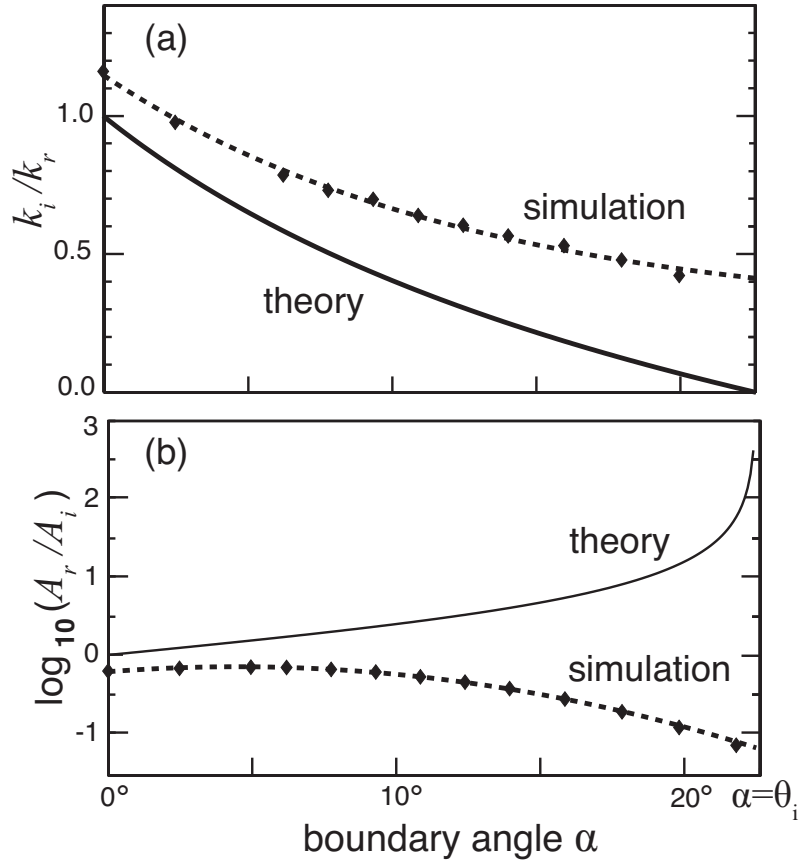


Figure 5.6: (a) The ratio of the dominant wavenumber in the incoming beam to the dominant wavenumber of the reflected beam (at the fundamental frequency) given by theory (Eq. (2.48), solid curve) and numerical simulation (data points and dashed line is an exponential fit to the data). (b) The prediction of the Tabaei et al. theory for the ratio of the reflected fundamental wave beam's peak amplitude to the incoming wave beam's peak amplitude,  $A_r/A_i = \sin(\theta_r + \alpha)/\sin(\theta_i - \alpha)$ , compared with the results from my numerical simulation. Theory predicts that the amplitude of the reflected wave should diverge at the critical angle, whereas the simulations yield quite different behavior with a broad peak in the reflected wave amplitude at about  $\alpha = 4.5^\circ$  and a monotonic decrease in amplitude for larger angles. (In both (a) and (b),  $\theta_i = 22.7^\circ$ ,  $A_{in} = 0.25$  cm, and  $a_{nonlinear} = 0.25$ .)

harmonic, as expected from the resonant triad theory of Thorpe [126]; however, the results for the wavevectors in my experiments and simulations do not support the triad theory.

#### 5.2.4 Reflection compared to interaction of unbounded beams

Although equation (2.48) does not correctly predict the characteristics of the reflected wave beams, harmonic generation might still result from the nonlinear interaction of the incoming and reflected wave beams. The process is analogous to the incoming wave beam interacting with a virtual wave beam emanating from the bottom boundary with the same characteristics as the reflected wave. Such beam-beam interactions will create harmonic waves except for certain beam orientations as shown by Jiang and Marcus [61]. I simulated such colliding wave beams (in the absence of a reflecting boundary) with the amplitude and wavenumber profile of the interacting beams matched to those of the incoming and reflected wave beams from the simulations.

My numerical simulations reveal that the intensity of the second harmonic is proportional to the sum of the integrated intensities (see Section 3.2.3) of the incident beam and the reflected fundamental wave beam. Hence harmonic generation is strongest when the virtual reflected wave beam is the strongest since the incoming wave beam is held fixed. As shown in Fig. 5.6, the reflected wave beam has the highest amplitude (and highest integrated kinetic energy because it is also relatively wide) at a small angle of  $\alpha$ , *not* at the critical angle. Thus my data cannot be explained as a nonlinear self-

interaction between the incoming and reflected wave beams, as suggested by Phillips [101, 100].

## Chapter 6

### Discussion

#### 6.1 Low Reynolds Number Flagellar Swimming

My laboratory experiments and Dr. Zhang's numerical simulations are in good agreement (Fig. 4.1) and demonstrate that the Regularized Stokeslet method of Cortez et al. is accurate within experimental error. The results differ from predictions of resistive force theories whether using drag coefficients by Gray et al.[49] or Lighthill[81] for biologically relevant helical flagella with parameters:

$$\begin{aligned} 1/25R < a < 1/10R \\ 0 < \lambda/R < 20 \\ 0 < L/\lambda < 10 \end{aligned} \tag{6.1}$$

where  $a$  is the filament diameter,  $R$  is the helical radius,  $\lambda$  is the pitch and  $L$  is the axial length of the flagellum, see Fig. 2.1.

In the Stokesian regime, velocity perturbations decay slowly, following power laws; therefore, interaction between segments is long-ranged. Resistive force theory neglects these hydrodynamic interactions between different parts of a flagellum, which leads to three quantitative discrepancies.

First, the theory significantly overestimates propulsive forces for flagella with small pitch ( $\lambda < 8R$ ), as shown in Fig. 4.1. The separation of filament

segments in a flagellum is controlled by pitch. As  $\lambda$  decreases, segments of a flagellum become closer in space, cf. the red segments in Fig. 2.1, which leads to stronger hydrodynamic interactions. In the small  $\lambda$  limit ( $\lambda \rightarrow 0$ ), a flagellum hydrodynamically becomes a cylinder that produces zero propulsive force, as observed in both experiments and simulations. However, theory predicts that the propulsive force continues to increase with decreasing  $\lambda$ . (In contrast, our parameterized resistive force theory expression for  $F_x$  decreases with decreasing  $\lambda$  because the drag coefficients for  $C_n$  and  $C_t$ , Eqs. 4.14 and 4.13, also decrease with decreasing  $\lambda$ , Fig. 4.4.)

Second, theory overestimates the drag force for all flagella by a factor of about two, and therefore, does not accurately describe the entire resistance matrix. This factor of two is due to the spatial anisotropy of hydrodynamic interactions. To qualitatively illustrate this point, I follow the idea of slender body theory and model the flow induced by a flagellum using a line of singularity solutions of Stokes flow of appropriate strength (Sec. 2.2.2). To simplify the discussion, only the point force singularities, i.e. Stokeslets, are considered.

A Stokeslet,  $f\hat{f}$ , generates a flow field at a location  $\vec{r}$  away from itself as:  $\vec{u}(\vec{r}) = \frac{f}{8\pi\mu} \left( \frac{\vec{r}}{r} + \frac{\vec{r}\vec{r}}{r^3} \right) \cdot \hat{f}$ . If  $\vec{r}$  is in the direction of  $\hat{f}$ , the generated flow is  $\vec{u}_{\parallel} = \frac{f}{4\pi\mu r} \hat{f}$ . If  $\vec{r}$  is perpendicular to  $\hat{f}$ , the generated flow is  $\vec{u}_{\perp} = \frac{1}{2} \vec{u}_{\parallel}$ . This means flow around a Stokeslet is spatially anisotropic: flow at a location in the Stokeslet direction is twice as strong as flow at an equally-distant location in the perpendicular direction.

Now consider the two red segments in Fig. 2.1. When the flagellum is translated in the  $\hat{x}$  direction, local velocities of these segments, and therefore the associated Stokeslets, are also in  $\hat{x}$  direction. When the flagellum rotates in the axial direction, local velocities and the associated Stokeslets, are perpendicular to the  $\hat{x}$  direction so the red segments in Fig. 2.1 interact more weakly. Consequently, hydrodynamic interaction between these segments is stronger if the flagellum translates, which leads to smaller axial drag  $D_x$  by a factor of about 2 as compared to theory. (We also encountered this factor of two when Dr. Zhang extracted  $C_n$  and  $C_t$  from his simulations and calculated a value for drag. It was about one half of what we measured, even though the drag coefficients properly described the propulsive force and torque.) A more detailed analysis would take into account interactions between all of the Stokeslets, but the same effects would be present.

Third, theory predicts that propulsive force, torque and drag all scale linearly with axial length  $L$ . My results demonstrate that only torque scales linearly, and propulsive force  $F_x$  and drag  $D_x$  scale as  $L/\ln(L/r)$  as  $L \rightarrow \infty$ . In Sec. 4.2.1, I show an analytic derivation of these scalings within the context of slender body theory derived by my collaborator Dr. Liu. This modified resistive force theory more accurately accounts for length dependent hydrodynamic interactions.

Nonlinear length scaling of propulsive force and axial drag should be expected on physical grounds as well. Imagine assembling a flagellum one turn  $\left(\frac{\lambda}{\cos\theta}\right)$  at a time. When the longer flagellum is rotated in the fluid, all

of the Stokeslets are perpendicular to the  $\hat{x}$  direction so the additional length creates little new hydrodynamic interaction because of the anisotropy of the Stokeslets. However, when the lengthened flagellum is translated in the  $\hat{x}$  direction, the Stokeslets are all aligned in the same direction, so each new turn is interacting not only with the turn immediately next to it, but also all of the other turns on the flagellum. Thus, I do not expect the propulsive force and drag to scale linearly with length, whereas the torque should, which is what I found in my analysis and the experimental and numerical data.

These length scalings have important consequences on how hydrodynamic efficiency depends on the axial length. Inserting the new resistive force expressions (4.10), (4.11) and (4.12) into (4.16) demonstrates that hydrodynamic efficiency depends on the axial length as

$$\varepsilon \propto \frac{1}{\ln(L/R)} \quad (6.2)$$

For bacteria, the contour length of a flagellum is fixed so the larger helical radius of the normal form has a shorter axial length, which explains the normal form's higher hydrodynamic efficiency.

In summary, I conclude that resistive force theories of Gray et al. and Lighthill, which are often used in interpreting bacterial swimming data and in design of nanobots are seriously deficient both qualitatively and quantitatively, failing badly especially for biologically relevant flagellar geometries with shorter wavelengths.

The traditional description can be greatly improved using the new pa-

parameterization scheme developed by Dr. Zhang so that its application to low Reynolds number swimming is more accurate. His parameterization scheme also demonstrates the importance of ensuring that any such parameterization is internally consistent and fully describes the resistance matrix.

### **6.1.1 Future bacterial swimming work**

My bacterial swimming work began with the simplest problem related to flagellar swimming, a rigid rotating helix at low Reynolds number. I have shown that even this problem is not well understood theoretically. There remain several open questions: the long range nature of hydrodynamic interactions means that boundaries have important consequences in flagellar swimming. Such effects are important because most bacteria are found swimming either near boundaries or swimming in swarms with other bacteria.

I have already begun a study of boundary effects with my collaborators. We are studying the effect of a nearby boundary on propulsive force, torque and drag of a flagellum. Researchers have observed that bacteria near surface swim in circles because they experience boundary forces perpendicular to their direction of motion, which generates a net torque on the bacterium. An approximate theory has been developed to describe these effects[74]. We intend to quantify the effect of the boundary distance on the flagellum's resistance matrix elements using experiments and simulations similar to those presented in this dissertation, and compare them to this theory.

Another simple extension to our bacterial swimming work is to look

at the effect of another nearby flagellum that may be rotating in the same or opposite sense. Researchers have seen that bacteria swim at much higher velocities when swimming in a group and this effect is not well understood[142]. This biological phenomenon likely has a fluid mechanical basis and it would be interesting to test how hydrodynamic efficiency is affected by proximity to another flagellum.

Finally, we are using a Newtonian fluid to make these measurements, while bacteria and other microorganisms often swim in non-Newtonian fluids such as mucus or other biological fluids. The range of validity of my results and could be explored using colloidal fluids with silicone oil being the continuous phase of the colloid. Otherwise, the measurement techniques would be identical.

## **6.2 Harmonic Generation by Reflection Internal Waves**

My laboratory experiments and numerical simulations for an internal wave reflecting from a sloping boundary are in excellent agreement (Fig. 5.5), and they reveal a distinct peak in the second harmonic intensity as the boundary angle varies. My results differ from the predictions by Tabaei et al., [121] except for very weak forcings – weaker than those measurable in experiments – in which case I recover the results of Tabaei et al. for wave beam angles greater than  $\sim 25^\circ$ ; i.e., the boundary angle of maximum harmonic generation approaches the critical angle. (This agreement extended to somewhat lower wave beam angles when the fluid viscosity was decreased by an order

of magnitude.) However, we found that even for low intensity incident beams ( $a_{nonlinear} \sim 0.01$ ), the result from my simulation differs from the weakly nonlinear theory prediction for the wavenumber ratios  $k_i/k_r$  (cf. Fig. 5.6(a)).

I did not find agreement with the resonant triad prediction of Thorpe [126] for any conditions, likely because as pointed out in Section 2.3.3, Thorpe derived his result for a plane wave reflecting from a boundary, not for a packet of plane waves (finite extent wave beam), where there are interactions that depend on the wavenumber profile of the wave beam.

Neither the Tabaei et al. nor the Thorpe theory correctly predicts the boundary angle that maximizes the generation of second harmonic waves in my laboratory experiments or numerical simulations. However, I obtained a prediction (Eq. 5.2) for the angle of maximum second harmonic intensity in good agreement with my results from experiment and simulations; my prediction was based on the observation that when the second harmonic has maximum intensity, the widths of the incoming and second harmonic beams are equal (cf. Section 5.1.3). Importantly, equation (5.2) holds with the viscosity reduced by an order of magnitude, and this result is correlated with long wave period. Thus, it may be relevant in the ocean since wave beams near the generation region are intense and have long wave periods that are of the order of the tidal forcing period [55, 38]. Further, wave beams generated by tidal flow over topography in a stratified fluid have a profile similar to those generated in my experiments and simulations [68].

My results indicate that critically reflecting internal waves (where the

internal wave beam propagation angle matches that of the sloping boundary ( $\theta = \alpha$ ), rather than being a source of intense second harmonic waves, dissipate energy in the boundary region. Although my experiments and simulations are for nonlinear waves (i.e., they are not described by weakly nonlinear theory), I did not observe strongly nonlinear phenomena such as density inversions, turbulent events, or other direct evidence of mixing. However, I did observe strong mean flows propagating from the reflection region. The observed mean flows are similar to the strong boundary currents found by Eriksen [31] and observed for tidal flow on topography where the slope is near the critical angle [21, 143]. Recent observations by van Haren and Gostiaux [138] provide direct evidence of breaking tidal-frequency internal waves along a seamount. They show that the process involves the coupling of low-frequency tidal waves with high-frequency internal waves near the buoyancy frequency. This result suggests that the internal wave reflection problem studied in this dissertation is an important part of the ocean mixing process.

### **6.2.1 Future work on internal wave reflection**

There are numerous questions raised by my work that warrant further investigation theoretically and experimentally. The foremost need is for a first principles derivation of the empirical, geometric prediction in Sec. 5.1.3 which accurately describes the boundary angle that maximizes second harmonic generation.

An interrelated issue that has generated interest both from the review-

ers of the paper when it was published and subsequently after its publication is the relationship between the incoming wave beam wavenumbers and the reflected and second harmonic wavenumbers, which is in contrast to the long-held assumption of how harmonic waves are generated through resonant triad interactions. Not only did my data differ from resonant triad predictions in the limit of intense internal wave beams, but also even for weaker beams that would presumably be well-described by the weakly nonlinear theories.

A logical extension of my experimental and numerical work would be to pursue a three-dimensional wave reflection study where the boundary angle is tilted in two dimensions with respect to the incoming wave beam. Such reflection processes are more realistic with respect internal wave reflection in the ocean, though more complicated experimentally and numerically. The simulation code I used can be adapted for three dimensional work, and in fact, the core solver was written for a three-dimensional domain.

Another extension of my work is currently being pursued by another researcher in our group who is looking at reflection of internal wave beams in a fluid where the buoyancy frequency  $N$  is not constant, as in the ocean. In such a stratified fluid, a wave beam can encounter a region where it cannot propagate because the buoyancy frequency is lower than the wave frequency, and the dispersion relation (2.47) cannot be satisfied [67]. The wave beam reflects because it is evanescent in this region, analogous to total internal reflection of light. This may be a common occurrence in the ocean, based on work described in Benjamin King's thesis that shows such "turning depths"

are ubiquitous in the ocean.

Finally, obtaining a better understanding of the boundary layer dynamics and quantifying mixing from internal wave reflection would be very useful in determining the mechanisms by which input tidal energy is converted into vertical mixing in the ocean. Such work would benefit from a technique for generating more intense internal waves than those we were able to produce with our wave maker. We found large amplitude plate oscillations create local mixing near the wavemaker rather than a propagating wave beam.

## Appendix

The code was obtained from Marcus and Jiang [61] to whom I am indebted for providing the code and for assistance in using it. I made minor modifications to the code to make the numerical work easier.

The primary modification I made to the code was to implement a function to read the parameters from an ASCII file titled *parameters.ascii*, rather than have the parameters hard-coded into the source code. These modifications were to several of the files listed below in Sec. 0.1, but primarily to *main.f90*. A subroutine called *readParametersfile* reads parameter values for variables I varied frequently during the study. The code for this subroutine is in the file *parameterFileReader.f90*.

As shown in Fig. 6.2.1, new variables can be added to the subroutine by adding new lines of the form in the figure. The user must specify whether it is an integer (*getParamInteger*) or a real number (*getParamreal*) and then in parentheses the name of the variable in the ASCII file in single quotes, e.g. 'ny', and the destination variable in the code, e.g. *grid%ny*. The subroutine parses the ASCII file looking for instances of the text identified in quotes and reads the text on the right hand side of an equals sign as the value of the parameter, e.g. *ny=256*, will result in the variable *grid%ny* being assigned the value 256 in the simulation.

This addition greatly simplifies the process of not only changing parameter values, but also of keeping the simulations organized because the Filemaker database described in Sec. 3.2.2 is tightly integrated with it.

```

! =====
! Parameter Read Subroutine
contains
  subroutine readParametersFile(fileName, grid, params, time, whichInit, &
    wavemaker)
    character(len=*), intent(in) :: fileName
    type(grid3d), intent(inout) :: grid
    type(param_type), intent(inout) :: params
    type(time_type), intent(inout) :: time
    integer, intent(inout) :: whichInit ! Not used here (selects which
      intialization process
    type(wavemakerType), intent(out) :: wavemaker

    call newParamReader(fileName, paramReader)
    success = getParamInteger(paramReader, 'nx', grid%nx)
    if(.not.(success)) print *, 'could not read parameter nx...'
    print *, grid%nx
    success = getParamInteger(paramReader, 'ny', grid%ny)
    if(.not.(success)) print *, 'could not read parameter ny...'
    print *, grid%ny
    success = getParamInteger(paramReader, 'nz', grid%nz)
    if(.not.(success)) print *, 'could not read parameter nz...'
    print *, grid%nz
    success = getParamReal(paramReader, 'Lx', wavemaker%Lx)
    if(.not.(success)) print *, 'could not read parameter Lx...'
    print *, wavemaker%Lx
  end subroutine
end contains

```

Figure 1: Code from the *main.f90* source file showing the implementation of the parameter reader subroutine. New variables may be created here and read from the parameters.ascii file at runtime.

## 0.1 Compiling source files

The source code is stored in the following files, all of which include comments within the code that explains their purpose:

1. base\_density\_profile\_init.f90
2. chebyshev.f90
3. comp\_grid.f90
4. diagnostics.f90
5. fft.f90
6. fftw3.f90
7. flow\_init.f90
8. flow\_variables.f90
9. greens\_functions\_init.f90
10. helmholtz.f90
11. ibmf95lapack.f90
12. main.f90
13. more\_diagnostics.f90
14. more\_more\_diagnostics.f90

15. parameterFileReader.f90
16. parameters.f90
17. phdf5Wrappers.f90
18. time\_integ.f90
19. vec\_ops.f90
20. wave\_generator\_init.f90

These files and a Makefile need to be in the same directory to compile the executable that runs the code. Fig. 2 shows a Makefile written for use on the Ranger system at the Texas Advanced Computing Center (TACC). A user will need to know the basics of how to create a Makefile, but starting with this example, the process is generally straightforward.

In the Makefile, there are several variables, identifiable because they are in all capital letters, that are defined to allow the compilation command to be more easily modified. `OBJS` refers to `.o` files created by the Fortran compiler from each of the source Fortran code files listed above at compilation time. `FC` refers to the Fortran compiler that will be used. In this case, I am using the `mpif90` compiler at TACC because I want to run the code in parallel. `FFLAGS` are compiler options that I want to use for this system. They will be different depending on the computer architecture being used. `MPIINC` is the directory path to where the Fortran compiler is installed on the Ranger system, another

architecture specific setting. The same is true for the FFTWLIB, FFTWINC, PHDF5LIB and PHDF5LIB variables that identify the location of the these libraries on Ranger (see Sec. 0.2)

The variable DEST is the name of the destination for the compilation, i.e. the name of the executable to be created at the end of compilation. The name choice is arbitrary. The following lines in the Makefiles are the compilation commands that create the executable named vortex. The line that begins .f90.o: instructs the Fortran compiler to create the .o files that then become part of the OBJS. The next line beginning with .f90.mod instructs the compiler to create .mod files. The final compilation line begins with vortex which instructs the compiler to create the destination executable from the OBJS .o files that are linked to the specified libraries.

The next two commands: clean and archive, are used to remove or archive previously compiled versions of the source code and the destination executable.

Thus, this is a simple (as compared to many Makefiles) process to compile the code that requires only a basic working knowledge of linux environments.

## 0.2 Libraries needed

There are only two libraries needed to run the code. The first is an FFTW library, which can be obtained from [www.fftw.org/](http://www.fftw.org/). However, TACC

```

.SUFFIXES :
.SUFFIXES : .f90 .o .mod

OBJS =comp_grid.o \
      fft.o \
      vec_ops.o \
      helmholtz.o \
      chebyshev.o \
      diagnostics.o \
      phdf5Wrappers.o \
      flow_variables.o \
      parameters.o \
      parameterFileReader.o \
      flow_init.o \
      greens_functions_init.o \
      wave_generator_init.o \
      base_density_profile_init.o \
      time_integ.o \
      more_diagnostics.o \
      more_more_diagnostics.o \
      main.o

FC      =mpif90
FFLAGS  = -O3 -xT

MPIINC  = -I/opt/MPI/intel10.1/mvapich-gen2/0.9.8/include

FFTWLIB = -L$(TACC_FFTW3_LIB) -lfftw3
FFTWINC = -I$(TACC_FFTW3_INC)

PHDF5LIB = -L/home/00921/brucerod/lib/hdf5/lib -lhdf5_fortran -lhdf5
PHDF5INC = -I/home/00921/brucerod/lib/hdf5/lib

DEST     =vortex

.f90.o:
$(FC) -c $(FFLAGS) $(FFTWINC) $(PHDF5INC) $<

.f90.mod:
$(FC) -c $(FFLAGS) $(FFTWINC) $(PHDF5INC) $<

vortex: $(OBJS)
$(FC) $(FFLAGS) $(OBJS) $(FFTWLIB) $(PHDF5LIB) -o $(DEST)

clean:
rm -f *.o *.mod $(DEST)

archive:
DATE=`date '+%b%d%Y'`; \
tar cf - Makefile *.f90 | bzip2 > rotating_anelastic_flow_$
$DATE.tar.bz2

```

Figure 2: Makefile created for use on the Ranger system at the Texas Advanced Computing Center.

always installs this library on its machines and compiling it is only necessary if a local machine is used.

However, the code also uses PHDF5 library to write the data output in HDF5 format files. TACC installs this on their systems, but they leave out parts of the library that are necessary to run the code. Therefore, a user must compile a complete HDF5 library, available from [www.hdfgroup.org/](http://www.hdfgroup.org/). In the example Makefile, the PHDF5 library is in my home directory as specified in the path variable.

## Bibliography

- [1] J. J. Abbott, K. E. Peyer, M. C. Lagomarsino, L. Zhang, L. X. Dong, I. K. Kaliakatsos, and B. J. Nelson. How should microrobots swim? *International Journal of Robotics Research*, 28(11-12):1434–1447, 2009.
- [2] S. Asakura. Polymerization of flagellin and polymorphism of flagella. *Adv Biophys*, 1:99–155, 1970.
- [3] S. Asakura and T. Iino. Polymorphism of salmonella flagella as investigated by means of in vitro copolymerization of flagellins derived from various strains. *Journal of Molecular Biology*, 64(1):251–268, 1972.
- [4] J. E. Avron, O. Gat, and O. Kenneth. Optimal swimming at low Reynolds numbers. *Phys. Rev. Lett.*, 93(18):186001, 2004.
- [5] J. E. Avron, O. Kenneth, and D.H. Oaknin. Pushmepullyou: an efficient micro-swimmer. *New Journal of Physics*, 7(1):234, 2005.
- [6] P. G. Baines. On internal tide generation models. *Deep-Sea Res.*, 29(3):307–338, 1982.
- [7] P. G. Baines and F. Xin-Hua. Internal tide generation at a continental-shelf slope junction - a comparison between theory and a laboratory experiment. *Dyn.*, 9(3):297–314, 1985.

- [8] N. J. Balmforth, G. R. Ierley, and W. R. Young. Tidal conversion by subcritical topography. *J. Phys. Oceanogr.*, 32(10):2900–2914, 2002.
- [9] J. A. Barranco and P. S Marcus. A 3D spectral anelastic hydrodynamic code for shearing, stratified flows., pp. 21–46. *J. Comput. Phys.*, 219:21–46, 2006.
- [10] G. K. Batchelor. Slender-body theory for particles of arbitrary cross-section in stokes flow. *Journal of Fluid Mechanics*, 44(03):419–440, 1970.
- [11] B. Behkam and M. Sitti. Design methodology for biomimetic propulsion of miniature swimming robots. *Journal of Dynamic Systems Measurement And Control-Transactions of The Asme*, 128(1):36–43, 2006.
- [12] T. H. Bell. Lee waves in stratified flows with simple harmonic time-dependence. *J. Fluid Mech.*, 67(FEB25):705–722, 1975.
- [13] T. H. Bell. Topographically generated internal waves in open ocean. *J. Geophys. Res.*, 80(3):320–327, 1975.
- [14] H. C. Berg. [http://www.rowland.harvard.edu/labs/bacteria/movies\\_rsphe.html](http://www.rowland.harvard.edu/labs/bacteria/movies_rsphe.html): Runs and stops 1.
- [15] H. C. Berg. Motile behavior of bacteria. *AIP*, 53(1):24–29, 2000.
- [16] H. C. Berg. The rotary motor of bacterial flagella. *Annual Review of Biochemistry*, 72(1):19–54, 2003.

- [17] H. C. Berg. Bacterial flagellar motor. *Current Biology*, 18(16):R689 – R691, 2008.
- [18] H. C. Berg and R. A. Anderson. Bacteria swim by rotating their flagellar filaments. *Nature*, 245(5425):380–382, 1973.
- [19] D. A. Cacchione and Wunsch C. I. Experimental study of internal waves over a slope. *J. Fluid Mech.*, 66:223–239, 1974.
- [20] D. A. Cacchione and L. F. Pratson. Internal tides and the continental slope. *Amer. Sci.*, 92(2):130–137, 2004.
- [21] D. A. Cacchione, L. F. Pratson, and A. S. Ogston. The shaping of continental slopes by internal tides. *Science*, 296(5568):724–727, 2002.
- [22] C. R. Callidine. Change of waveform in bacterial flagella: The role of mechanics at the molecular level. *Journal of Molecular Biology*, 118(4):457–479, 1978.
- [23] NASA Goddard Space Flight Center. <http://svs.gsfc.nasa.gov/search/sensor/modis.html>.
- [24] S. Chattopadhyay, R. Moldovan, C. Yeung, and X. L. Wu. Swimming efficiency of bacterium escherichia coli. *Proc. Natl. Acad. Sci. U. S. A.*, 103(37):13712–13717, 2006.
- [25] S. Chattopadhyay and X. L. Wu. The effect of long-range hydrodynamic interaction on the swimming of a single bacterium. *Biophys. J.*, 96(5):2023–2028, 2009.

- [26] R. Cortez, L. Fauci, and A. Medovikov. The method of regularized Stokeslets in three dimensions: Analysis, validation, and application to helical swimming. *Physics of Fluids*, 17(3):031504, 2005.
- [27] N. C. Darnton and H. C. Berg. Force-extension measurements on bacterial flagella: Triggering polymorphic transformations. *Biophysical Journal*, 92(6):2230 – 2236, 2007.
- [28] N. C. Darnton, L. Turner, S. Rojevsky, and H. C. Berg. On torque and tumbling in swimming escherichia coli. *J. Bacteriol.*, 189(5):1756–1764, 2007.
- [29] T. Dauxois and W. R. Young. Near-critical reflection of internal waves. *J. Fluid Mech.*, 390:271–295, 1999.
- [30] I. P. D. DeSilva, J. Imberger, and G. N. Ivey. Localized mixing due to a breaking internal wave ray at a sloping bed. *J. Fluid Mech.*, 350:1–27, 1997.
- [31] C. C. Eriksen. Observations of internal wave reflection off sloping bottoms. *J. Geophys. Res-Oc. Atm.*, 87(NC1):525–538, 1982.
- [32] C. C. Eriksen. Implications of ocean bottom reflection for internal wave spectra and mixing. *J. Phys. Oceanogr.*, 15(9):1145–1156, 1985.
- [33] C. C. Eriksen. Internal wave reflection and mixing at Fieberlin Guyot. *J. Geophys. Res.*, 103,C2:2977–2994, 1998.

- [34] R. Ferrari and C. Wunsch. Ocean circulation kinetic energy: Reservoirs, sources, and sinks. *Annu. Rev. Fluid Mech.*, 41:2513–282, 2009.
- [35] A. Fincham and G. Delerce. Advanced optimization of correlation imaging velocimetry algorithms. *Exp. Fluids*, 29:S13, 2000.
- [36] B. M. Friedrich, I. H. Riedel-Kruse, J. Howard, and F. Julicher. High-precision tracking of sperm swimming fine structure provides strong test of resistive force theory. *Journal of Experimental Biology*, 213(8):1226–1234, 2010.
- [37] C. Garrett. Internal tides and ocean mixing. *Science*, 301(5641):1858–1859, 2003.
- [38] C. Garrett and E. Kunze. Internal tide generation in the deep ocean. *Annu. Rev. Fluid Mech.*, 39:57–87, 2007.
- [39] C. Garrett, P. MacCready, and P. Rhines. Boundary mixing and arrested Ekman layers - rotating stratified flow near a sloping boundary. *Annu. Rev. Fluid Mech.*, 25:291–323, 1993.
- [40] C. Garrett and W. Munk. Internal waves in the ocean. *Annu. Rev. Fluid Mech.*, 11:339–369, 1979.
- [41] T. Gerkema. Internal-wave reflection from uniform slopes: higher harmonics and Coriolis effects. *Nonlinear Processes in Geophysics*, 13(3):265–273, 2006.

- [42] T. Gerkema, C. Staquet, and P. Bouruet-Aubertot. Decay of semi-diurnal internal-tide beams due to subharmonic resonance. *Geophys. Res. Lett.*, 33(8):L08604, 2006.
- [43] T. Gerkema, C. Staquet, and P. Bouruet-Aubertot. Nonlinear effects in internal-tide beams, and mixing. *Ocean Modelling*, 12(3-4):302–318, 2006.
- [44] T. Gerkema and J. T. F. Zimmerman. *An introduction to internal waves*. Lecture notes, Royal NIOZ, Texel, 2008.
- [45] L. Gostiaux and T. Dauxois. Laboratory experiments on the generation of internal tidal beams over steep slopes. *Phys. Fluids*, 19(2):028102, 2007.
- [46] L. Gostiaux, T. Dauxois, H. Didelle, J. Sommeria, and S. Viboud. Quantitative laboratory observations of internal wave reflection on ascending slopes. *Phys. Fluids*, 18(5):056602, 2006.
- [47] L. Gostiaux, H. Didelle, S. Mercier, and T. Dauxois. A novel internal waves generator. *Exp. Fluids*, 42(1):123–130, 2007.
- [48] J. Gray. The movement of sea-urchin spermatozoa. *J. Exp. Biol.*, 32(4):775–801, 1955.
- [49] J. Gray and G. J. Hancock, G. J. The propulsion of sea-urchin spermatozoa. *J. Exp. Biol.*, 32(4):802–814, 1955.

- [50] N. Ha, B. Goo, and H. Yoon. Development of a propulsion system for a biomimetic thruster. *Chinese Science Bulletin*, 56(4):432–438, 2011.
- [51] G. J. Hancock. The self-propulsion of microscopic organisms through liquids. *Proceedings of the Royal Society of London. Series A, Mathematical and Physical Sciences*, 217(1128):pp. 96–121, 1953.
- [52] R. M. Harshey. Bacterial motility on a surface: Many ways to a common goal. *Annual Review of Microbiology*, 57(1):249–273, 2003.
- [53] K. Hasegawa, I. Yamashita, and K. Namba. Quasi- and nonequivalence in the structure of bacterial flagellar filament. *Biophysical Journal*, 74(1):569–575, 1998.
- [54] P. E. Holloway and B. Barnes. A numerical investigation into the bottom boundary layer flow and vertical structure of internal waves on a continental slope. *Cont. Shelf Res.*, 18(1):31–65, 1998.
- [55] P. E. Holloway and M. A. Merrifield. Internal tide generation by seamounts, ridges, and islands. *J. Geophys. Res.*, 104:25,937–25,951, 1999.
- [56] T. Ikeda, S. Asakura, and R. Kamiya. “Cap” on the tip of salmonella flagella. *Journal of Molecular Biology*, 184(4):735–737, 1985.
- [57] T. Ikeda, S. Asakura, and R. Kamiya. Total reconstitution of salmonella flagellar filaments from hook and purified flagellin and hook-associated proteins in vitro. *Journal of Molecular Biology*, 209(1):109–114, 1989.

- [58] G. N. Ivey and R. I. Nokes. Vertical mixing due to the breaking of critical internal waves on sloping boundaries. *J. Fluid Mech.*, 204:479–500, 1989.
- [59] G. N. Ivey, K. B. Winters, and I. P. D. De Silva. Turbulent mixing in a sloping benthic boundary layer energized by internal waves. *J. Fluid Mech.*, 418:59–76, 2000.
- [60] A. Javam, J. Imberger, and S. W. Armfield. Numerical study of internal wave reflection from sloping boundaries. *J. Fluid Mech.*, 396:183–201, 1999.
- [61] C. H. Jiang and P. S. Marcus. Selection rules for the nonlinear interaction of internal gravity waves. *Phys. Rev. Lett.*, 102(12):124502, 2009.
- [62] R. E. Johnson and C. J. Brokaw. Flagellar hydrodynamics - comparison between resistive-force theory and slender-body theory. *Biophysical Journal*, 25(1):113–127, 1979.
- [63] R. Kamiya and S. Asakura. Flagellar transformations at alkaline pH. *Journal of Molecular Biology*, 108(2):513 – 518, 1976.
- [64] R. Kamiya and S. Asakura. Helical transformations of salmonella flagella in vitro. *Journal of Molecular Biology*, 106(1):167 – 186, 1976.

- [65] R. Kamiya, S. Asakura, and S. Yamaguchi. Formation of helical filaments by copolymerization of two types of straight flagellins. *Nature*, 286(5773):628–630, 1980.
- [66] S. Kim and J. S. Karrila. *Microhydrodynamics: Principles and Selected Applications*. Boston,MA: Butterworth-Heinemann, 1991.
- [67] B. King, M. Stone, H. P. Zhang, T. Gerkema, M. Marder, R. B. Scott, and H. L. Swinney. Buoyancy frequency profiles and internal semidiurnal tide turning depths in the oceans. *Journal of Geophysical Research-Oceans*, *submitted*, 2011.
- [68] B. King., H. P. Zhang, and H. L. Swinney. Tidal flow over three-dimensional topography generates out-of-forcing-plane harmonics. *Geophys. Res. Lett.*, 37:L14606, 2010.
- [69] S. Koyasu and Y. Shirakihara. Caulobacter crescentus flagellar filament has a right-handed helical form. *Journal of Molecular Biology*, 173(1):125 – 130, 1984.
- [70] T. Kuhlbrodt, A. Griesel, M. Montoya, A. Levermann, M. Hofmann, and S. Rahmstorf. On the driving processes of the Atlantic meridional overturning circulation. *Rev. Geophys.*, 45(1):RG2001, 2007.
- [71] H.K. Kuiken. H.a. lorentz: Sketches of his work on slow viscous flow and some other areas in fluid mechanics and the background against which it arose. *Journal of Engineering Mathematics*, 30(1):II+1–18, 1996.

- [72] P. K. Kundu and I. M. Cohen. *Fluid Mechanics*. Elsevier, New York, pp. 246–261, 2004.
- [73] K. G. Lamb. Nonlinear interaction among internal wave beams generated by tidal flow over supercritical topography. *Geophys. Res. Lett.*, 31(9):L09313, 2004.
- [74] E. Lauga, W. R. DiLuzio, G. M. Whitesides, and H. A. Stone. Swimming in circles: Motion of bacteria near solid boundaries. *Biophys. J.*, 90(2):400–412, 2006.
- [75] E. Lauga and T. R. Powers. The hydrodynamics of swimming microorganisms. *Reports on Progress in Physics*, 72(9):096601, 2009.
- [76] J. R. Ledwell, E. T. Montgomery, K. L. Polzin, L. C. St Laurent, R. W. Schmitt, and J. M. Toole. Evidence for enhanced mixing over rough topography in the abyssal ocean. *Nature*, 403(6766):179–182, 2000.
- [77] S. Legg. Internal tides generated on a corrugated continental slope. part I: Cross-slope barotropic forcing. *J. Phys. Oceanogr.*, 34(1):156–173, 2004.
- [78] S. Legg and A. Adcroft. Internal wave breaking at concave and convex continental slopes. *J. Phys. Oceanogr.*, 33(11):2224–2246, 2003.
- [79] H. Li, J. Tan, and M. Zhang. Dynamics modeling and analysis of a swimming microrobot for controlled drug delivery. *Automation Science and Engineering, IEEE Transactions on*, 6(2):220–227, 2009.

- [80] R. C. Lien and M. C. Gregg. Observations of turbulence in a tidal beam and across a coastal ridge. *Journal of Geophysical Research-Oceans*, 106(C3):4575–4591, 2001.
- [81] J. Lighthill. Flagellar hydrodynamics - John Von Neumann lecture, 1975. *Siam Review*, 18(2):161–230, 1976.
- [82] J. Lighthill. Reinterpreting the basic theorem of flagellar hydrodynamics. *Journal of Engineering Mathematics*, 30(1):25–34, 1996.
- [83] J. Lighthill. *Waves in Fluids*. Cambridge University Press, 2002.
- [84] G. Lowe, M. Meister, and H. C. Berg. Rapid rotation of flagellar bundles in swimming bacteria. *Nature*, 325(6105):637–640, 1987.
- [85] R. Macnab and D. E. Koshland Jr. Bacterial motility and chemotaxis: Light-induced tumbling response and visualization of individual flagella. *Journal of Molecular Biology*, 84(3):399–406, 1974.
- [86] R. M. Macnab. How bacteria assemble flagella. *Annual Review of Microbiology*, 57(1):77–100, 2003.
- [87] R. M. Macnab and M. K. Ornston. Normal-to-curly flagellar transitions and their role in bacterial tumbling. stabilization of an alternative quaternary structure by mechanical force. *Journal of Molecular Biology*, 112(1):1 – 30, 1977.

- [88] R. D. Maladen, Y. Ding, P. B. Umbanhowar, A. Kamor, and D. I. Goldman. Mechanical models of sandfish locomotion reveal principles of high performance subsurface sand-swimming. *Journal of The Royal Society Interface*, 8(62):1332–1345, 2011.
- [89] T. Minamino and K. Namba. Self-assembly and type III protein export of the bacterial flagellum. *Journal of Molecular Microbiology and Biotechnology*, 7(1/2):5 – 17, 2004.
- [90] J. N. Moum, D. R. Caldwell, J. D. Nash, and G. D. Gundersen. Observations of boundary mixing over the continental slope. *J. Phys. Oceanogr.*, 32(7):2113–2130, 2002.
- [91] W. Munk and C. Wunsch. Abyssal recipes II: energetics of tidal and wind mixing. *Deep Sea Research Part I: Oceanographic Research Papers*, 45(12):1977–2010, 1998.
- [92] J. D. Nash, M. H. Alford, E. Kunze, K. Martini, and S. Kelly. Hotspots of deep ocean mixing on the Oregon continental slope. *Geophys. Res. Lett.*, 34(1):L01605, 2007.
- [93] J. D. Nash, E. Kunze, J. M. Toole, and R. W. Schmitt. Internal tide reflection and turbulent mixing on the continental slope. *J. Phys. Oceanogr.*, 34(5):1117–1134, 2004.
- [94] P. Olla. Effective swimming strategies in low Reynolds number flows.

*The European Physical Journal B - Condensed Matter and Complex Systems*, 80:263–273, 2011. 10.1140/epjb/e2011-10944-1, 2011.

- [95] A. R. Osborne and T. L. Burch. Internal solitons in the Andaman sea. *Science*, 208(4443):451–460, 1980.
- [96] A. R. Osborne, T. L. Burch, and R. I. Scarlet. Influence of internal waves on deep-water drilling. *Journal of Petroleum Technology*, 30(OCT):1497–1504, 1978.
- [97] G. Oster. Density gradients. *Sci. Amer.*, 213:70, 1965.
- [98] T. Peacock, P. Echeverri, and N.J. Balmforth. An experimental investigation of internal wave beam generation by two-dimensional topography. *J. Phys. Ocean.*, 2007.
- [99] T. Peacock and A. Tabaei. Visualization of nonlinear effects in reflecting internal wave beams. *Phys. Fluids*, 17(6):061702, 2005.
- [100] O. M. Phillips. Energy transfer in rotating fluids by reflection of inertial waves. *Phys. Fluids*, 6:513–520, 1963.
- [101] O. M. Phillips. *The Dynamics of the Upper Ocean*. Cambridge University Press, 1977.
- [102] O. M. Phillips, J. H. Shyu, and H. Salmun. An experiment on boundary mixing - mean circulation and transport rates. *J. Fluid Mech.*, 173:473–499, 1986.

- [103] K. L. Polzin, K. G. Speer, J. M. Toole, and R. W. Schmitt. Intense mixing of Antarctic bottom water in the equatorial Atlantic ocean. *Nature*, 380(6569):54–57, 1996.
- [104] K. L. Polzin, J. M. Toole, J. R. Ledwell, and R. W. Schmitt. Spatial variability of turbulent mixing in the abyssal ocean. *Science*, 276(5309):93–96, 1997.
- [105] P. Puig, A. Palanques, J. Guillen, and M. El Khatab. Role of internal waves in the generation of nepheloid layers on the northwestern Alboran slope: Implications for continental margin shaping. *Journal of Geophysical Research-Oceans*, 109(C9):C09011, 2004.
- [106] E. M. Purcell. Life at low Reynolds-number. *American Journal of Physics*, 45(1):3–11, 1977.
- [107] E. M. Purcell. The efficiency of propulsion by a rotating flagellum. *Proceedings of the National Academy of Sciences*, 94(21):11307–11311, 1997.
- [108] R. D. Ray and G. T. Mitchum. Surface manifestation of internal tides generated near Hawaii. *Geophys. Res. Lett.*, 23(16):2101–2104, 1996.
- [109] O. Raz and J. E. Avron. Swimming, pumping and gliding at low Reynolds numbers. *New Journal of Physics*, 9(12):437, 2007.
- [110] O. Reynolds. An experimental investigation of the circumstances which determine whether the motion of water shall be direct or sinuous, and

- of the law of resistance in parallel channels. *Philosophical Transactions of the Royal Society of London*, 174:935–982, 1883.
- [111] B. E. Rodenborn, D. Kiefer, H. P. Zhang, and H. L. Swinney. Harmonic generation by reflecting internal waves. *Physics of Fluids*, 23(2), 2011.
- [112] B. Scharf. Real-time imaging of fluorescent flagellar filaments of *Rhizobium lupini* h13-3: Flagellar rotation and pH-induced polymorphic transitions. *J. Bacteriol.*, 184(21):5979–5986, 2002.
- [113] M. Silverman and M. I. Simon. Bacterial flagella. *Annual Review of Microbiology*, 31(1):397–419, 1977.
- [114] D. N. Slinn and J. J. Riley. Turbulent mixing in the oceanic boundary layer caused by internal wave reflection from sloping terrain. *Dyn.*, 24(1-4):51–62, 1996.
- [115] D. N. Slinn and J. J. Riley. A model for the simulation of turbulent boundary layers in an incompressible stratified flow. *J. Comput. Phys.*, 144(2):550–602, 1998.
- [116] D. N. Slinn and J. J. Riley. Turbulent dynamics of a critically reflecting internal gravity wave. *Theoretical and Computational Fluid Dynamics*, 11(3-4):281–303, 1998.
- [117] S. E. Spagnolie and E. Lauga. Comparative hydrodynamics of bacterial polymorphism. *Phys. Rev. Lett.*, 106(5):058103, 2011.

- [118] C. Staquet and J. Sommeria. Internal gravity waves: From instabilities to turbulence. *Annu. Rev. Fluid Mech.*, 34:559–593, 2002.
- [119] J. Sznitman, X. Shen, R. Sznitman, and P. E. Arratia. Propulsive force measurements and flow behavior of undulatory swimmers at low Reynolds number. *Physics of Fluids*, 22(12):121901, 2010.
- [120] A. Tabaei and T. R. Akylas. Nonlinear internal gravity wave beams. *J. Fluid Mech.*, 482:141–161, 2003.
- [121] A. Tabaei, T. R. Akylas, and K. G. Lamb. Nonlinear effects in reflecting and colliding internal wave beams. *J. Fluid Mech.*, 526:217–243, 2005.
- [122] G. I. Taylor. Analysis of the swimming of microscopic organisms. *Proceedings of the Royal Society of London. Series A, Mathematical and Physical Sciences*, 209(1099):pp. 447–461, 1951.
- [123] G. I. Taylor. The action of waving cylindrical tails in propelling microscopic organisms. *Proc. Roy. Soc. A*, 2II:225–39., 1952.
- [124] S. G. Teoh, G. N. Ivey, and J. Imberger. Laboratory study of the interaction between two internal wave rays. *J. Fluid Mech.*, 336:91–122, 1997.
- [125] S. A. Thorpe. Current and temperature variability on the continental slope. *Philosophical Transactions of The Royal Society of London Series A-Mathematical Physical and Engineering Sciences*, 323(1574):471–517, 1987.

- [126] S. A. Thorpe. On the reflection of a train of finite amplitude waves from a uniform slope. *J. Fluid Mech.*, 178, 1987.
- [127] S. A. Thorpe. Thermal fronts caused by internal gravity-waves reflecting from a slope. *J. Phys. Oceanogr.*, 22(1):105–108, 1992.
- [128] S. A. Thorpe. On the interactions of internal waves reflecting from slopes. *J. Phys. Oceanogr.*, 27(9):2072–2078, 1997.
- [129] S. A. Thorpe. Fronts formed by obliquely reflecting internal waves at a sloping boundary. *J. Phys. Oceanogr.*, 29(9):2462–2467, 1999.
- [130] S. A. Thorpe. The generation of alongslope currents by breaking internal waves. *J. Phys. Oceanogr.*, 29(1):29–38, 1999.
- [131] S. A. Thorpe. Internal wave reflection and scatter from sloping rough topography. *J. Phys. Oceanogr.*, 31(2):537–553, 2001.
- [132] S. A. Thorpe. On the reflection of internal wave groups from sloping topography. *J. Phys. Oceanogr.*, 31(10):3121–3126, 2001.
- [133] S. A. Thorpe. *The Turbulent Ocean*. Cambridge University Press, 2005.
- [134] J.R. Toggweiler and B. Samuels. On the ocean’s large-scale circulation near the limit of no vertical mixing. *J. Phys. Oceanogr.*, 28:1832, 1998.
- [135] J. M. Toole, K. L. Polzin, and R. W. Schmitt. Estimates of diapycnal mixing in the abyssal ocean. *Science*, 264(5162):1120–1123, 1994.

- [136] L. Turner, W. S. Ryu, and H. C. Berg. Real-time imaging of fluorescent flagellar filaments. *Journal of Bacteriology*, 182(10):2793–2801, 2000.
- [137] H. van Haren. Nonlinear motions at the internal tide source. *Geophys. Res. Lett.*, 33(11):L11605, 2006.
- [138] H. van Haren and L. Gostiaux. A deep ocean Kelvin-Helmholtz billow train. *Geophys. Res. Lett.*, 37:L03605, 2010.
- [139] C. L. Wolfe, P. Cessi, J. L. McClean, and M. E. Maltrud. Vertical heat transport in eddying ocean models. *Geophys. Res. Lett.*, 35:L23605, 2008.
- [140] C. Wunsch and R. Ferrari. Vertical mixing, energy and the general circulation of the oceans. *Annu. Rev. Fluid Mech.*, 36:281–314, 2004.
- [141] C.I. Wunsch. Progressive internal waves on slopes. *J. Fluid Mech.*, 35:131–144., 1969.
- [142] H. P. Zhang, Avraham Be’er, E. L. Florin, and Harry L. Swinney. Collective motion and density fluctuations in bacterial colonies. *Proceedings of the National Academy of Sciences*, 107(31):13626–13630, 2010.
- [143] H. P. Zhang, B. King, and H. L. Swinney. Experimental study of internal gravity waves generated by supercritical topography. *Phys. Fluids*, 19:096602, 2007.

- [144] H. P. Zhang, B. King, and Harry L. Swinney. Resonant generation of internal waves on a model continental slope. *Phys. Rev. Lett.*, 100(24):244504, 2008.